

UNIVERSITY OF SOUTHAMPTON

Phase-field Model of Rapid Solidification of a
Binary Alloy

by

Noor Atinah Ahmad

Thesis submitted for the degree of Doctor of Philosophy

Faculty of Mathematical Studies

This thesis was submitted for examination in March 1997

UNIVERSITY OF SOUTHAMPTON

ABSTRACT

FACULTY OF MATHEMATICAL STUDIES

MATHEMATICS

Doctor of Philosophy

PHASE-FIELD MODEL OF RAPID SOLIDIFICATION OF A BINARY ALLOY

by Noor Atinah Ahmad

This thesis extends earlier works by Wheeler, Boettinger and McFadden [1, 2], and Aziz [9], on a non-equilibrium phenomenon commonly observed in rapid solidification, called ‘solute trapping’. The phase-field model by Wheeler, Boettinger and McFadden (denoted as WBM2), and a sharp interface model, known as the Continuous Growth Model (CGM), due to Aziz, are found to show similar solute trapping behaviours.

Numerical and asymptotic analyses are carried out on the WBM2 model. The numerical results establish the possible cause of solute trapping, which is, the relative size of the diffusive length scale of the solute field, and the characteristic thickness of the interface. As the solidification velocity increases, the diffusive length scale of the solute field decreases. When its value becomes comparable or smaller than the characteristic thickness of the interface, solute trapping occurs. This relationship cannot be realised by the Continuous Growth Model because it is a sharp interface model, in which, the interface is assumed to have negligible thickness. This result emphasises the capability of a phase-field model in studying the solute trapping phenomenon.

The asymptotic analysis successfully produces an explicit form for the ‘diffusive speed’, which is an important parameter in solute trapping, as it scales the solidification velocity. Solute trapping becomes important when the solidification velocity exceeds this diffusive speed. The explicit expression obtained for the diffusive speed, relates it directly to the material parameters of the alloy; this is the first theory to provide such a relationship. A comparison with values calculated from experimental data on solute trapping shows that this expression supports the experimental results.

Another non-equilibrium effect found in rapid solidification processes, is the ‘kinetic undercooling’ effect. This effect is also successfully captured by the WBM2 model, where the numerical values of the interface temperature is found to decrease with the interface velocity.

Contents

1	Introduction	6
1.1	Background	7
1.2	Overview	7
1.2.1	Chapter 3	7
1.2.2	Chapter 4	8
1.2.3	Chapter 5	9
1.2.4	Chapter 6	10
1.2.5	Chapter 7	10
1.2.6	Chapter 8	11
1.3	Main results	12
2	The solidification process	14
2.1	Mathematical analysis of solidification	16
2.1.1	Sharp interface model of the solidification of a binary alloy	16
2.2	Rapid solidification	19
3	Phase-field Models	21
3.1	Thermodynamics	24
3.2	The relation between phase-field models and sharp interface models	24
3.3	Anisotropy	26
3.4	Numerical Calculations.	27
3.5	Phase-field models of binary alloys	28
3.5.1	WBM2 model	29
3.5.2	Asymptotic analysis for $\epsilon/\delta \ll 1$ of WBM2	31
3.5.3	Developments in phase-field models of binary alloys	32

4	Sharp Interface Models of Solute Trapping	34
4.1	Introduction	34
4.2	The solute trapping models.	35
4.2.1	Stepwise Growth Model.	35
4.2.2	Continuous Growth Model (CGM).	37
4.2.3	Aperiodic Stepwise Growth Model.	39
4.3	Experimental Results.	40
5	The sharp interface limit of WBM2 when the solid-liquid interface is curved	43
5.1	The governing equations	44
5.2	Asymptotic analysis in the limit $\epsilon/\delta \rightarrow 0$	47
5.2.1	The outer region	47
5.2.2	The inner region	48
5.2.3	Matched asymptotic analysis	51
5.3	Interface temperature	53
6	Phase diagram for a regular solution model	54
6.1	The free energy	54
6.2	Common tangent constructions	57
6.2.1	Classical thermodynamics	57
6.2.2	Phase-field model	60
6.3	Numerical results	61
7	Numerical Computations of the Phase-field Model	64
7.1	Dimensionless equations	65
7.2	Numerical procedures	66
7.2.1	Initial guesses	68
7.2.2	Grid resolution	70
7.3	Numerical results	75
7.3.1	Solutions when $D_S/D_L = 1$	75
7.3.2	Solutions when $D_S/D_L \neq 1$	79
7.4	The determining factor of solute trapping	80
7.5	Partition coefficient and diffusive speed	81
7.5.1	The diffusive speed	82
7.5.2	Dependence of V_D on k_e , D_S/D_L and ϵ	83

7.6	Interfacial temperature	86
8	The high solidification velocity limit with δ/ϵ constant	88
8.1	Asymptotic analysis for $\tilde{V}_\epsilon \rightarrow \infty$	88
8.1.1	Partition coefficient and solute trapping	91
8.1.2	Diffusive speed	95
8.1.3	Extension to cases $k_e > 1$ and $\tilde{V}_\epsilon < 0$	97
8.2	Varying diffusivity	101
8.2.1	Partition coefficient	101
8.2.2	Diffusive speed	105
8.3	Comparing the asymptotic solutions with numerical solutions	107
8.4	The relationship between Continuous Growth Model and the WBM model . . .	112
9	Summary and future work	115
9.1	Summary and discussion of the results on solute trapping	115
9.1.1	The independence of solute trapping on δ	115
9.1.2	The partition coefficient	116
9.1.3	Correlation between the diffusive speed and the material parameters . .	117
9.1.4	The cases $k_e > 1$ and $\tilde{V}_\epsilon < 0$	118
9.1.5	The relationship between phase-field models and the CGM	119
9.2	Kinetic undercooling effect	119
9.3	Future work	120
9.3.1	The stability of the planar interface during rapid solidification	120
9.3.2	Solute trapping treatments using curved interface and regular solution formulations of the WBM2 model	120
9.3.3	The interface diffusivity	121
9.3.4	Solute trapping treatments using other phase-field models	122
9.4	Conclusion	122
A	Transforming the cartesian coordinates into the curvilinear coordinates	124
B	The Nickel-Copper alloy data	127
C	Finite difference discretization	128
D	Fortran program PDE1.F	131

Acknowledgement

In the name of Allah, the Most Beneficient, the Most Merciful.

All the praises and thanks be to Allah, the Lord of the worlds.

‘Read! In the Name of your Lord Who has created (all that exists),
Has created man from a clot (of blood),
Read! And your Lord is the Most Generous,
Who has taught (the writing) by the pen,
Has taught man that which he knew not.’
(Al-Qur’an, Sura Al-‘Alaq, verses 1-5).

Chapter 1

Introduction

Solidification is an important industrial process which finds application in the production of materials used in the fabrication of modern electronic devices, as well as the casting of metals. In the case of electronic materials, controlled solidification is necessary to provide a very high quality product. The optimisation of control techniques for this process requires a rigorous method to tackle the issue effectively. Thereby, mathematical models are established to introduce a practical way of assessing the techniques, by relating the fundamental concepts involved in the solidification process, to practice.

The essential aim of this thesis is to provide a step forward in the development of mathematical models of solidification processes. It builds on the original work of Wheeler, Boettinger and McFadden [1, 2] which focuses on a particular type of model known as the ‘Phase-field Model’. Their proposed version of the model has been successful in predicting typical phenomena observed in solidification, one of which, is in the prediction of ‘solute trapping’ during the rapid solidification of a binary alloy [2]. This development motivates most of the work carried out in this thesis whose main emphasis is on the rapid solidification of a binary alloy.

Solute trapping is a ‘non-equilibrium’ phenomenon that is commonly observed in rapid solidification of alloys. It has been identified as one of the factors involved in the formation of supersaturated solid solutions in rapid solidification during pulsed laser melting [3]. The uniform distribution of solute in alloys produced in this way, is a great advantage in subsequent processing of the material [4]. The limited understanding of the mechanisms of solute trapping, and rapid solidification in general, emphasise the importance of the analyses carried out in this thesis. Current solidification theories mainly focus on the concept of ‘equilibrium solidification’, which is commonly associated with much slower rates of solidification. Improvements in rapid solidification techniques in recent years, have enabled in-depth experimental

studies of the process. This is a great advantage towards providing a more comprehensive understanding of the non-equilibrium nature of rapid solidification processes.

1.1 Background

Knowledge of solidification processes is needed in order to understand how solidification models are derived. We set out, in chapter 2, by considering solidification on a microscopic level, where we focus our attention on the processes occurring in the region separating the two bulk phases, the liquid phase and the solid phase. This region is called ‘the solid-liquid interface’. During solidification, the growth of solid causes the interface to move forward into the liquid, thus it is often referred as the ‘moving boundary’ or the ‘free boundary’. There are two different types of mathematical formulations of the process, known as the **Sharp Interface Model** and the **Phase-field Model**.

A detailed description of the sharp interface model is given in chapter 2, which involves deriving an appropriate set of governing equations for temperature and concentration in the bulk phases, as well as boundary conditions at the ‘outer boundary’, i.e., the boundary around the melted region, and a set of conditions at the moving boundary, i.e., the interface. The concept of ‘equilibrium solidification’ is also introduced here; this is used to derive the conditions for temperature and concentration at a slowly moving interface, where the conditions are very closely approximated by the equilibrium conditions [5]. An extension of this model to the rapid solidification process, takes into account the deviation, from equilibrium to non-equilibrium, of the interfacial conditions (often referred as the ‘response function’). This leads to the derivation of the corresponding non-equilibrium versions of the response functions given by Boettinger et. al. [6, 7]; their results are outlined.

1.2 Overview

This section provides an overview of each chapter of the thesis. Chapters 3 and 4 contain literature reviews on phase-field models and solute trapping models respectively. In the remaining chapters, we discuss the analyses we carried out on the WBM2 model.

1.2.1 Chapter 3

The phase-field model is described in this chapter, where the state of art of the model is reviewed. The differences between the phase-field model and the sharp interface model are

outlined and the simplest form of the model, which corresponds to the solidification of a pure material is described. Several analyses of the phase-field model that have been carried out over the years are summarised here, for example the derivation of the thermodynamically consistent phase-field model, the sharp interface limits of the model as well as the numerical calculations. The description of several extensions to the model to include anisotropy, and the extension to binary alloys are also included.

The phase-field model which will be used in this thesis is referred to as the ‘WBM2 model’, proposed by Wheeler, Boettinger and McFadden [2], and it is described in detail in the last section of chapter 3. The model is for **isothermal** solidification of a binary alloy, where the solid and liquid solutions are assumed to be ideal. It is a generalisation of an earlier model WBM1 [1]. In WBM2, a **solute gradient energy** is added in the corresponding free energy functional. The generalisation was made because the WBM1 model failed to capture the correct variation in the jump of concentration across the interface, with interface velocity. Although WBM2 qualitatively predicts the correct variation (i.e., solute trapping) in the sharp interface limit, it is still not clear whether the improvement is due to the solute gradient energy term, or, the particular distinguished limit they chose for their asymptotic analysis. This is one of the important issues that is resolved in this thesis.

The free energy functional used in the model is given in this section, together with the corresponding governing equations for the phase-field and the solute field, along with the appropriate boundary conditions. The asymptotic analysis of the model in the sharp interface limit (where the interface is assumed to be planar) is summarised and the resulting boundary conditions across the interface are presented. The solute trapping phenomena observed in the leading order solution of the solute field is discussed briefly. Several other calculations for binary alloys are also discussed, they include the computation of dendrites in binary alloy solidification and a phase-field description of growth of a *eutectic alloy*.

1.2.2 Chapter 4

This chapter contains discussions of solute trapping models. We describe three different solute trapping models, **the Stepwise Growth Model (SGM)**, **the Continuous Growth Model (CGM)** and **the Aperiodic Stepwise Growth Model (ASGM)**. All of these models are due to Aziz [9], and they are based on the sharp interface formulation of solidification processes. The three models differ in their description of the growth mechanism of the solid, although it can be shown that there are special cases in which they are equivalent. In all the models, the same measure of solute trapping is used, i.e. the partition coefficient k . This is defined as the

ratio of the solute concentration in the far-field to the maximum concentration. Experimental observations suggest that its value should rise from an equilibrium value, k_e , say (whenever $k_e < 1$), where k_e is a constant for each alloy, at a constant temperature, to a saturation value of unity, as the interface velocity increases, i.e. as the system departs from equilibrium. (Whenever $k_e > 1$, the value of k should decrease from k_e to unity, as the interface velocity increases). All the models are successful in predicting the ‘qualitative’ variation of k , but the CGM is noted to be the most successful in predicting its ‘quantitative’ value [4, 8].

Each solute trapping model contains a fitting parameter which is defined as the ‘diffusive speed’ (solute trapping is observed when the interface speed exceeds this speed). Its value is defined to be the ratio of the interface diffusion coefficient, D_i , to the inter-atomic distance λ . Because of the difficulty in obtaining direct measurements for D_i and λ , the diffusive speed is commonly assumed to be approximately equal to the ratio of the diffusivity in the liquid bulk phase to the interface width, but experimental measurements on solute trapping have proved the inaccuracy of this assumption [4].

At the end of chapter 4, we describe the experimental procedures involved in measuring the value of the partition coefficient for a particular interface speed. We also review the experimental results on solute trapping, observed in several alloys like the Silicon based alloys. One of the important results we highlight here is the inverse correlation found between the diffusive speed and the **equilibrium** partition coefficient, an observation made by Smith et. al. [4].

1.2.3 Chapter 5

The analysis of the WBM2 model carried out in [2] assumes the solid-liquid interface to be planar, and that the melted alloy transforms from an **ideal liquid solution** to an **ideal solid solution** during solidification. These assumptions provide a very simplified description of the process, hence, in order to afford a comparison with the ‘real’ system, further extensions need to be done. To this end, we used the model to propose a formulation in chapter 5, that assumes a curved solid-liquid interface.

In the curved interface formulation, the WBM2 model is expressed in a suitable curvilinear coordinate system. The sharp interface limit of this new configuration produces a set of boundary conditions across the interface. The resulting equation for the interface temperature is shown to capture the physical effect, known as the ‘thermal undercooling’ (or the ‘Gibbs-Thomson effect’), due to the curvature of the interface and the interface velocity. The undercooling effect due to the moving interface is also captured.

1.2.4 Chapter 6

Another extension of the WBM2 model is considered here which deals with transformation of a **regular liquid solution** to a **regular solid solution**. This is referred as the ‘regular solution’ model. It involves adding an extra term in the free energy density function of the WBM2 model. This term corresponds to the ‘entropy of mixing’ associated with the regular solution mixture. It contains a parameter G , which is the energy of pairwise interaction of the atoms, and represents a measure of the regularity of the solutions. The equilibrium phase diagram associated with this new model, is constructed for different values of G using the *common tangent construction* derived from both classical thermodynamics and the phase-field model.

1.2.5 Chapter 7

In this chapter, the solute trapping behaviour in the WBM2 phase-field model is analysed numerically, where the partition coefficient, k , is derived from the solutions for the solute field, obtained for a particular interface velocity. The definition for k is adopted from [2], and given by

$$k = \frac{\text{far - field concentration}}{\text{maximum concentration of solute}}, \quad (1.1)$$

The governing equations are non-dimensionalised in such a way that the solute gradient energy coefficient, δ , may be set to zero. We also allow the diffusivity to vary monotonically across the interface, from a value D_L on the liquid side, to a value of D_S on the solid side, where D_L and D_S are the diffusivities in the liquid and solid bulk phases respectively. The numerical procedures involved in the computation of the solutions are explained, with a demonstration of how a well-resolved solution is obtained.

The solutions are computed for the Nickel-Copper alloy (whose material parameters are given in appendix B), where they are described, for $D_S/D_L = 1$ and for $D_S/D_L \neq 1$. In the case of $D_S/D_L = 1$, the solutions are first computed for $\delta \neq 0$, an equivalent case to the one considered by Wheeler et. al. in [2]. The numerical solution for the solute field in this case, exhibits solute trapping as the interface velocity increases, confirming their results. The computations are then performed with $\delta = 0$ which has the effect of removing the solute gradient energy term from the model. Comparison of the results in the two cases, $\delta \neq 0$ and $\delta = 0$, leads to the conclusion that the solute gradient energy term is **not a prerequisite** for solute trapping. Therefore, for simplicity, the remainder of the calculations are carried out with $\delta = 0$.

The effect of varying diffusivity is captured by setting $D_S/D_L \neq 1$. This helps to predict the nature of the solutions as we approach the more realistic limit of $D_S/D_L \ll 0$, i.e., the liquid diffusivity is far greater than the solid diffusivity. The interface temperature also forms part of the solution, where we are able to obtain a set of values for the temperature corresponding to a range of interface speeds. The temperature variation with velocity is compared with the results predicted from sharp interface models.

A procedure is formulated so that for each interface speed V , a corresponding value for the partition coefficient k is calculated from the profile of the solute field obtained at that particular value of V , using equation (1.1). We performed *least squares fitting* on the numerical data, where we fit the following function to the k data,

$$k = \frac{k_e + V/V_D}{1 + V/V_D}, \quad (1.2)$$

which is the form for the partition coefficient given by CGM. The quantity V_D denotes the diffusive speed, and in this case, it acts as a fitting parameter. Repeating the procedure for a number of sets of $k - V$ data, we are able to study the correlation between V_D and (i) the equilibrium partition coefficient k_e (assumed less than 1), (ii) the diffusivity ratio D_S/D_L , and (iii) the interface width.

1.2.6 Chapter 8

In this chapter, an asymptotic analysis is carried out in the high interface velocity limit. In this limit, regular expansions for the phase-field and the solute field are obtained. The partition coefficient is defined in the same way as in the numerical analysis, i.e., (1.1). Therefore, a corresponding expansion for k is obtained, which shows the value increases to unity as V increases (k_e is assumed to be less than 1). The first two terms of the expansion are observed to be independent of δ , which supports the claim we made earlier based on the numerical results, that solute trapping is independent of the solute gradient energy term.

We proceed by expanding the form for k given by the CGM in the same limit. A functional form for V_D is found by equating this expansion with the expansion for k obtained earlier from the WBM2 model. This is done under the assumption that the trapping behaviour captured in both models is **quantitatively** the same ¹. Encouragingly, the functional form shows that V_D decreases with increasing values of k_e , which is in agreement with experimental results.

¹The validity of this assumption is later confirmed, where in the ‘dilute limit’, the ‘interdiffusion fluxes’ from the two models are found to be almost exactly identical. The interdiffusion flux is the flux of solute atoms that are diffusing away from the interface. It is derived in CGM using *the chemical rate theory*, whereas in the WBM2 model, it is given by the multiple of the gradient of the ‘interdiffusion potential’

The analyses are extended to cases where $k_e > 1$ and $V < 0$ (melting), where similar results are produced.

A more general form for V_D is obtained in the case $D_S/D_L \neq 1$. For the more realistic case where $D_S/D_L \approx 0$, the asymptotic approximation for V_D is compared with a set of data from experiment on solute trapping of several Silicon alloys.

1.3 Main results

In this thesis we set out to address several important issues regarding the solute trapping phenomena, observed in an earlier work by Wheeler et. al. [2]. These issues are outlined below;

- (i) the dependence of the solute gradient energy term on solute trapping;
- (ii) the dependence of various length scale in the problem, and their relative sizes, on solute trapping;
- (iii) to find a better means of estimating the value of the diffusive speed for a specific alloy;
- (iv) to establish a connection between the WBM2 model and the CGM.

After performing numerical and asymptotic analyses on the WBM2 model, we have successfully obtained results that enable us to resolve the issues above.

The successful prediction of solute trapping in the analysis of Wheeler et. al. in [2] has suggested that the inclusion of the solute gradient energy term in the free energy functional, may be the important factor that leads to this result. On the other hand, our numerical results clearly show that the solute trapping is **not due to the solute gradient energy term**. This result however, does not explain why solute trapping is not observed in the earlier model, WBM1 [1]. After analysing the length scales used in both formulations, [1] and [2], we discover that solute trapping is intimately related to the **relative sizes of the diffusive length scale of the solute field, and the characteristic thickness of the interface**. The diffusive length scale, denoted as D/V , decreases in size as the solidification velocity, V , is increased. When its size becomes **comparable** or **smaller** than the interface thickness, solute trapping results. It is not possible to draw this conclusion from Aziz's solute trapping models because they are based on the sharp interface models, where the interface is assumed to have negligible thickness, and hence prevent a direct connection between the interface thickness and the effect of solidification velocity on the length scale of the solute field.

The diffusive speed V_D is an important parameter which appears in all the solute trapping models described in chapter 4. However, none of the solute trapping theories to date is able to provide an explicit form for it. The common assumption that

$$V_D \approx \frac{\text{the diffusion coefficient in the liquid}}{\text{the interface thickness}}, \quad (1.3)$$

has been experimentally proven to be inaccurate by Smith et. al. [4], thereby, a better estimate is clearly needed. This issue is tackled in our asymptotic analysis, where we have succeeded in producing a functional form for V_D which **relates it to measurable parameters of the alloy**, such as the equilibrium segregation coefficient, k_e , the diffusivity ratio, D_S/D_L , and the interface thickness, l_i . It is even more encouraging to see that the form for V_D is **inversely correlated with k_e** , confirming the experimental prediction of Smith et. al. [4]. The agreement is shown to be both **qualitative and quantitative**, since we are able to show that the values of V_D calculated using this functional form **correspond to a reasonable value of the interface thickness**.

One interesting factor that arises from the analysis of the WBM2 model is that the predicted solute trapping behaviour resembles the behaviour observed in the CGM. Although both models are derived using two completely different formulations (phase-field formulation (WBM2) and sharp interface formulation (CGM)), the partition coefficient from both models are shown to have a very similar dependence on the interface velocity. Furthermore, the explicit functional form we obtain for V_D shows both quantitative and qualitative agreements with the values of V_D , derived using the CGM, from experimental results. A more detailed analysis of the governing equations for the solute field from both models has shown that, in the dilute alloy limit, the interdiffusion flux of both models are very similar. Because the interdiffusion flux plays an important role in the solute trapping process, the results offer an explanation as to why the solute trapping behaviour predicted in both models show a lot of resemblance.

In summary, this thesis provides several contributions to existing solute trapping theories. It also highlights the capabilities of the WBM2 model in predicting characteristic behaviours of solute trapping, and other non-equilibrium aspects of rapid solidification, for example, the kinetic undercooling. These findings should encourage further developments in the study of non-equilibrium solidification.

Chapter 2

The solidification process

A system undergoing solidification can be described macroscopically as one that consists of two distinct phases, solid and liquid, lying adjacent to each other with a thin interfacial region separating them. The temperature gradient across the interface promotes various processes that transform the liquid into solid at the interface, thereby changing the position of the interface. These processes are governed by a set of concepts describing the transport processes, thermodynamics and material science. In order to gain a thorough understanding of the interface dynamics, it is necessary to study the interface processes on the microscopic scale.

The interface is envisioned to be of two different types, an atomically flat interface, and a diffuse interface (see Fig. 2.1). On an atomically flat interface, the solid atoms are very closely packed resulting in a well-defined boundary between the solid and liquid. Transition from liquid to solid is assumed to take place across a single atomic layer. On the other hand, the diffuse interface is more ‘atomically rough’. The ordering of the atoms changes over a number of atomic layers, getting more and more ordered towards the fully crystalline side, where all the atoms are in their appropriate lattice sites and all heat of fusion is released [5].

During solidification, an atom from the liquid phase will find a site on the solid-liquid interface and ‘attach’ itself to it. The atom will naturally choose a site where it will lose a maximum amount of its heat of fusion if it moves there. Such a site would have to be where the atom gains a large number of nearest neighbours. The ease with which the solid can grow depends very much on the proportion of interface sites that are favorable for the atoms. A diffuse interface has a higher proportion of favorable sites for growth on it, compared to a flat interface; therefore it grows more easily. The growth mechanism of the two interfaces is also expected to be different. Because growth of solid occurs more easily, the diffuse interface

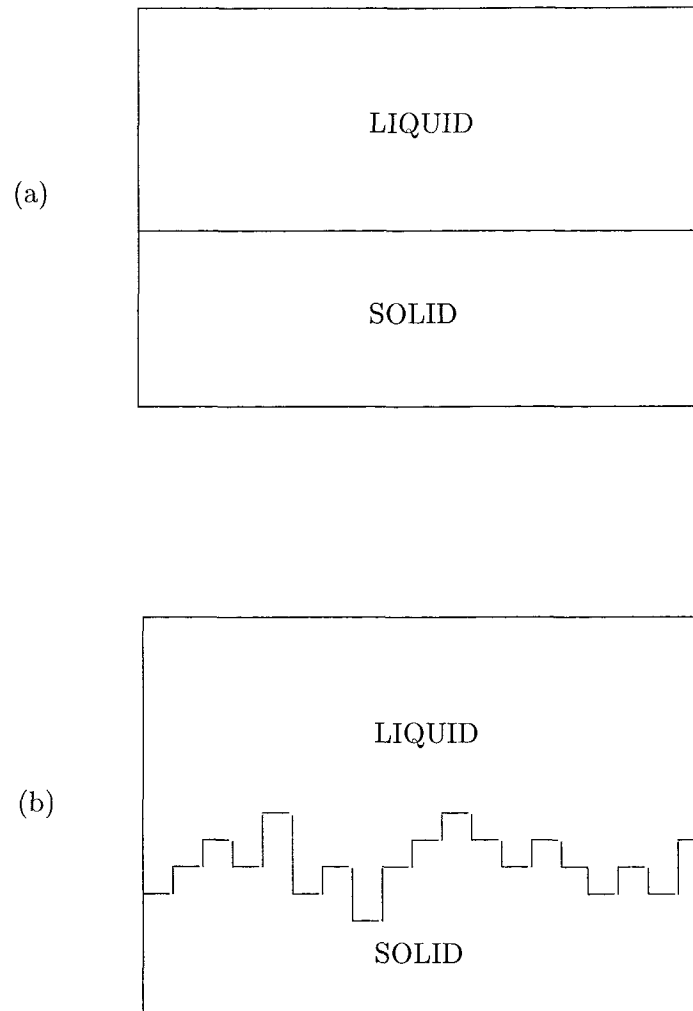


Figure 2.1: The two types of solid-liquid interface, (a) atomically flat interface, (b) a diffuse interface.

moves uniformly into the liquid and it is said to be a ‘continuous growth’. Forward growth of a flat interface occurs preferentially at steps which sweep laterally across the interface, this is called ‘lateral growth’.

In the next section we will discuss how the solidification process (applied to a binary alloy case) is analysed mathematically. Two different mathematical formulations are introduced, the **sharp interface model** and the **phase-field model**.

2.1 Mathematical analysis of solidification

Over the years, a number of mathematical models [1, 9, 10, 11, 12, 13, 14, 15] have been developed to describe phase transitions in solidification. The classical modelling approach [9, 10] represents the solid-liquid interface as a microscopically thin evolving surface. The governing equations are typically, diffusion equations for heat and concentration, formulated independently in the bulk phases. Boundary conditions are posed at the interface, which express the conservation of heat and mass across the interface and the assumption of local interface equilibrium. This gives rise to a free boundary problem. Numerical solutions require the tracking of the free boundary, involving intricate numerical schemes for problems with complex geometries. Models of this type are commonly known as *Sharp Interface Models*, and the corresponding model for a binary alloy is described in detail below.

The *Phase-field Models* are a more recent development compared to the sharp interface models. We will mostly focus our attention on the phase-field model in this thesis where a detailed description of the model is given in chapter 3.

2.1.1 Sharp interface model of the solidification of a binary alloy

The simplest sharp interface model of alloy solidification is one that describes the solidification of a dilute binary alloy (i.e. the mole fraction of a component of the alloy is very small compared to that of its complement), contained in a fixed region Ω . In such a case, we consider the system as a solvent-solute system, where, if the alloy is made up of components A and B , the A component is treated as the solvent and B as the solute. Let us define c to be the mole fraction of solute in the system, and T to be the system temperature. Therefore the diffusion of solute and heat in the solid bulk phase is described by,

$$D_S \nabla^2 c - \frac{\partial c}{\partial t} = 0, \tag{2.1}$$

and

$$\kappa_S \nabla^2 T - \frac{\partial T}{\partial t} = 0, \quad (2.2)$$

respectively, where D_S and κ_S are the solute and thermal diffusivity for the solid respectively, which are assumed constant. There is a similar pair of equations for the solute and heat diffusion in the liquid phase. We use the customary subscripts S and L to denote the respective quantities in the solid and liquid. These four equations are the governing equations for the solidification process.

Typically, conditions are imposed at the boundary of Ω to ensure no solute or heat enters or leaves the system. Thereby, we require

$$\frac{\partial c}{\partial \bar{n}} = 0 \quad \text{and}; \quad \frac{\partial T}{\partial \bar{n}} = 0, \quad (2.3)$$

where $\bar{\mathbf{n}}$ is the outward unit vector, normal to the fixed boundary. The governing equations (2.1) and (2.2), together with boundary conditions in (2.3) guarantees the conservation of solute and heat within the system.

Solute and heat are also conserved across the moving solid-liquid interface, a notion which is expressed in terms of their fluxes, and provide interfacial boundary conditions for the problem. The conservation of solute satisfies the following boundary condition,

$$D_S(\nabla c \cdot \hat{\mathbf{n}})_S - D_L(\nabla c \cdot \hat{\mathbf{n}})_L = (c_L - c_S)V_n, \quad (2.4)$$

applied on the solid on the interface, S , and the conservation of heat (also applied on S) is given by,

$$\kappa_S(\nabla T \cdot \hat{\mathbf{n}})_S - \kappa_L(\nabla T \cdot \hat{\mathbf{n}})_L = LV_n, \quad (2.5)$$

which allows for the latent heat production, denoted by the term proportional to L , where L is the latent heat of fusion. Here, $\hat{\mathbf{n}}$ represents the unit vector normal to the interface, directed into the liquid, which has a velocity component V_n in that direction. The quantities c_S and c_L are the interfacial concentrations on the solid and liquid side respectively.

Further, boundary conditions are imposed based on the assumption of local equilibrium at the interface. The equilibrium conditions for heat and solute are summarised by the so-called ‘phase diagram’. (See chapter 5 for a detailed discussion). An example of an idealised phase diagram is shown in Fig. 2.2(i). It gives the values of the interfacial concentrations of the solid and liquid phases, c_S and c_L , at a particular interfacial temperature. In the case of a dilute alloy, the phase diagram may be approximated by straight lines as the temperature of interest lies in the domain close to the melting point of the major component, T_M , say (see

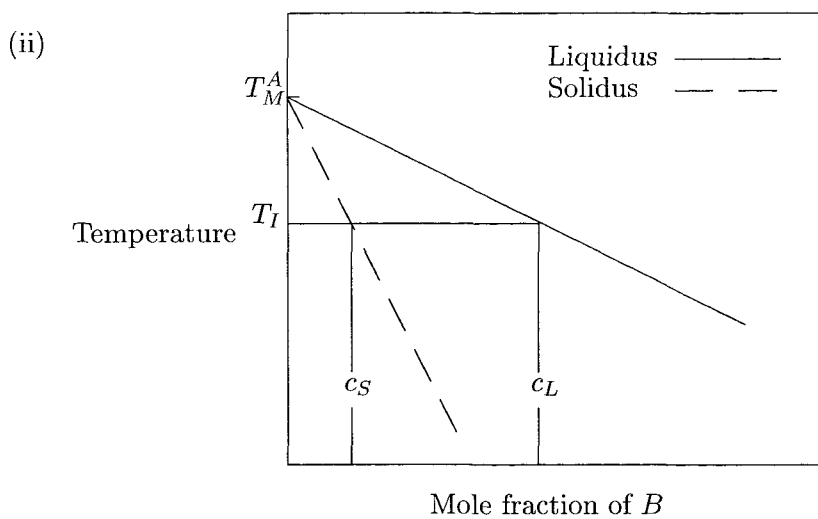
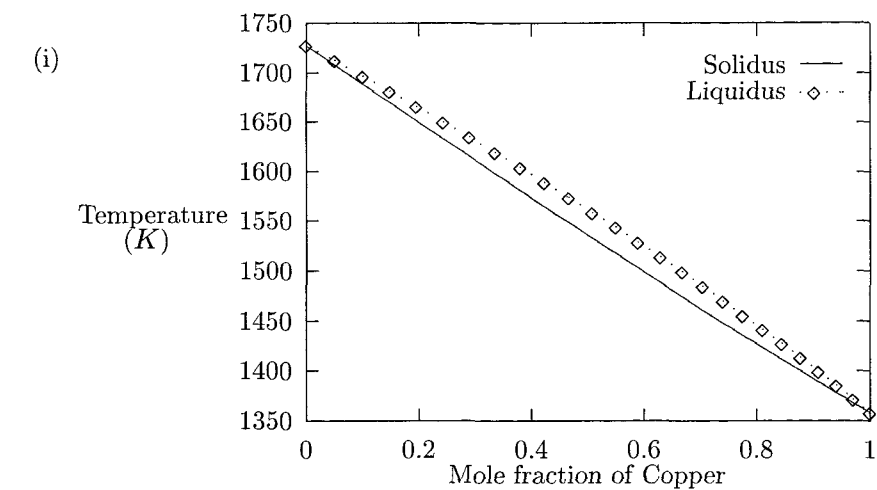


Figure 2.2: (i) The phase diagram of the Nickel-Copper alloy which is an example of an idealised phase diagram. (ii) The idealised phase diagram for a dilute alloy.

Fig. 2.2(ii)). The two interfacial concentrations are related through the following equation,

$$c_S = kc_L. \quad (2.6)$$

This equation describes the solute partitioning at the interface, where k indicates the degree of partitioning. Under the assumption of local equilibrium, k takes the value k_e , the so-called *equilibrium partition coefficient*.

The temperature is assumed continuous across the interface and its interfacial value, in the dilute limit, is given by,

$$T = T_M + m_L c_L + T_M \Gamma \mathcal{K}, \quad (2.7)$$

where m_L is the slope of the liquidus curve (the loci of c_L on the phase diagram). The term $T_M \Gamma \mathcal{K}$ is the effective change in the melting point due to the Gibbs-Thomson effect (i.e., the effect due to the interface being curved) with Γ being the capillary constant (defined as the ratio of the interfacial surface free energy to the latent heat of fusion per unit volume) and \mathcal{K} is the average curvature of the interface. Equations (2.1) to (2.7) provide a free boundary problem for the solidification of a dilute alloy.

2.2 Rapid solidification

The assumption of local interface equilibrium only holds when the solid-liquid interface is either stationary or it is moving at a very slow rate (typically 10^{-3}cms^{-1}). In solidification techniques such as the pulsed laser melting, the growth velocities are found to achieve up to several metres per second. Under such circumstances, the recrystallization of the melted region takes place under conditions that are far from equilibrium. Recent developments in the rapid solidification techniques have provided fundamental information on high-speed, non-equilibrium solidification. For example, it is observed that the value of the (non-equilibrium) partition coefficient k , is greater than the corresponding equilibrium value k_e (whenever $k_e < 1$). It is also found that k has a velocity dependence, and as the interface velocity increases, k rises to a saturation value of unity.

The observed increase in the value of k is termed as ‘solute trapping’. It is a phenomenon in which the solute atoms are trapped in the solid by the rapid incorporation of new layers of atoms at the interface. During solidification, a solute atom exchanges places many times across the interface before they are permanently embedded into the solid [3]. When the growth of solid occurs rapidly, the solute atom has a much reduced opportunity to escape into the liquid.

The mathematical study of non-equilibrium solidification processes to date have mostly been performed on sharp interface model. An extension of the simple version of the sharp interface model we presented in the previous section, to rapid solidification was provided by Baker and Cahn [16, 17]. They proposed a model with a thermodynamically consistent formulation for the interfacial boundary conditions in non-equilibrium solidification. This model employs the same governing equations (2.1) and (2.2) in the bulk phases and interfacial conservation equations (2.4) and (2.5). The conditions due to the assumption of local equilibrium, (2.6) and (2.7), were replaced by the following equations (in the dilute limit),

$$c_S = k(V_n)c_L, \quad (2.8)$$

and

$$T = T(V_n, c_L) + T_M \Gamma K, \quad (2.9)$$

where

$$k(V_n) = \frac{k_e + \beta_0 V_n}{1 + \beta_0 V_n}, \quad (2.10)$$

and

$$T(V_n, c_L) = T_M + m(V_n)c_L - \frac{m_L}{(k_e - 1)} \frac{V_n}{V_0}. \quad (2.11)$$

The quantity β_0 has dimensions of the reciprocal of the normal interface velocity V_n , and $m(V_n)$ is given by,

$$m(V_n) = m_L \left\{ 1 - \frac{1}{(k_e - 1)} [k_e - k(1 - \ln(k/k_e))] \right\},$$

where the liquidus slope m_L , is obtained from the phase diagram at the dilute limit. The velocity V_0 is defined in [18] to be the upper bound for V_n . The local interface temperature (2.9) (derived by Boettinger et. al. [6, 7]) is obtained from thermodynamic arguments for the free energy of the non-equilibrium system, and it corresponds to a process where ‘solute drag’ is limited. The more detailed treatment of solute trapping carried out by Aziz [9, 19, 20] will be discussed in chapter 4.

The study of rapid solidification using a diffuse interface model of solidification has been minimal. Advances in the development of the phase-field model, has made it possible for the numerical calculations of complicated geometries of the interface [21, 22]. These methods can be used to produce numerical computations of the solute trapping phenomenon and gain more insights into nonequilibrium solidification. The study in this direction has been proposed by Wheeler et. al. [1, 2], and their work is extended in this thesis.

Chapter 3

Phase-field Models

The phase-field method is an alternative approach to the sharp interface model in modelling solidification processes. It captures both the microscopic and the continuum aspects of the solid-liquid interface. An important difference between these two approaches is that, while the classical method involves prescribing boundary conditions at the evolving interface, the phase-field method avoids any explicit reference to it. Instead, an order parameter, i.e., the phase-field, $\phi(\mathbf{x}, t)$ is introduced to label the liquid and solid phases explicitly. It is a continuous function of space, \mathbf{x} , and time, t and characterises the phase of the system at each point (\mathbf{x}, t) . This function assumes constant values in the solid and liquid bulk phases, and varies monotonically between these two values, over thin transition layers which represent the interface. Therefore, unlike the classical models, which assume the interface to have negligible thickness, the phase-field model attributes a finite thickness to the interface and allows it to have an internal structure.

The concept of an order parameter has its roots in statistical physics and finds applications in the study of critical phenomena in dynamical systems. It goes back as early as 1893, when van der Waals [23] employed the method in his study of a fluid near its critical point. The approach was later used in the study of high temperature superconductivity by Landau and Ginzburg [24]. A model of spinodal decomposition for metallic alloys was proposed by Cahn and Hilliard [14] who derived the so-called ‘Cahn-Hilliard equation’ from the ‘Landau-Ginzburg’ energy functional (which is given in equation (3.1) below), in which, solute concentration was treated as the conserved order parameter. A similar theory was applied in the development of the ‘Allen-Cahn equation’ for the motion of a curved antiphase boundary [15] (with non-conserved solute).

The phase-field model for a pure material was first suggested by Langer [11] following an

adaptation of a similar model called ‘Model C’ by Halperin et. al. [25]. At around the same time, similar models of the solidification of a pure material were developed by Caginalp [12], Collins and Levine [13] and Umantsev and Roitburd [26]. Since then, phase-field models have received more attention as their potential was realised.

The model is generally based on a Landau-Ginzburg free energy functional, \mathcal{F} , assumed to be a function of ϕ and is given by,

$$\mathcal{F}[\phi, ..] = \int_{\Omega} \left[\frac{\epsilon^2}{2} |\nabla \phi|^2 + f(\phi, ..) + \dots \right] d\Omega, \quad (3.1)$$

where Ω is the region occupied by the system. The free energy density $f(\phi, ..)$ is usually chosen to have the double-well form with respect to ϕ , with minimas in the solid and liquid. The gradient energy coefficient ϵ determines the thickness of the interface [11] and the gradient energy term $|\nabla \phi|^2$ is associated with the surface free energy of the interface [14].

Many different forms of the free energy density function $f(\phi, ..)$ have been suggested. The phase-field model of a solidification process of a pure material developed by Kobayashi [21] employs the following form for $f(\phi, T)$,

$$f(\phi, T) = W \int_0^{\phi} p(p-1)[p-1/2 - \beta(T)] dp, \quad (3.2)$$

or,

$$f(\phi, T) = \frac{W}{4} \phi^2 (\phi - 1)^2 + \frac{W\beta(T)}{6} \phi^2 (3 - 2\phi), \quad (3.3)$$

where W is a constant with dimensions of energy per unit volume, $\beta(T)$ is a monotonic decreasing function of T such that $\beta(T_M) = 0$, T_M is the melting point of the material and $|\beta(T)| < 1/2$ (to ensure the minima of f are at $\phi = 0$ and $\phi = 1$). Here $\phi = 0$ represents the liquid phase and $\phi = 1$, the solid phase. Figure 3.1 shows the double-well form of f with respect to ϕ . Notice that when $T = T_M$, f has a ‘symmetric double-well’ form, where at the melting temperature, the second term in (3.3) (which is an ‘asymmetric’ function of ϕ) is identically equal to zero. Other choices of $f(\phi, ..)$ have been proposed by Penrose and Fife [27], Langer [11], Caginalp [12] and Wang et. al. [28].

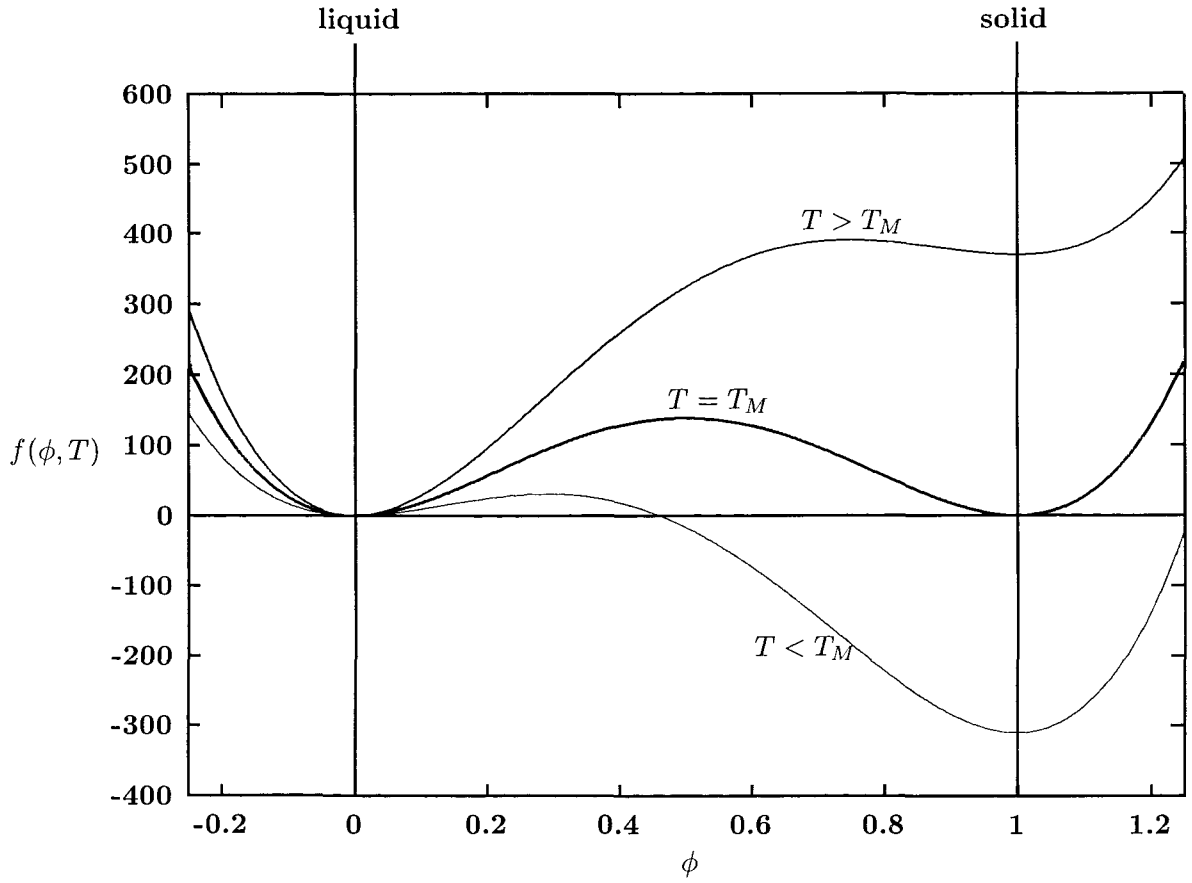


Figure 3.1: The variation of free energy density $f(\phi, T)$ given by (3.2), with ϕ . The function is drawn for three different characteristic values of T ; $T = T_M$, $T > T_M$ and $T < T_M$ [1].

The governing equation for the phase-field is derived from the free energy functional by requiring the functional to decrease monotonically in time, consistent with the second law of thermodynamics. The equation is postulated to be of the form,

$$\frac{\partial \phi}{\partial t} = -M_1 \frac{\delta \mathcal{F}}{\delta \phi}, \quad (3.4)$$

where M_1 is positive and may depend on the phase-field, the composition and the temperature of the system, and

$$\frac{\delta \mathcal{F}}{\delta \phi} = \frac{\partial f}{\partial \phi} - \epsilon^2 \nabla^2 \phi.$$

Other equations, describing the transport processes (i.e., equations for composition and temperature) are modified by adding terms that depend on the phase-field to allow, for example, for latent heat production in the interfacial region.

3.1 Thermodynamics

Penrose and Fife [27] claimed that the phase-field model is thermodynamically sound when applied to an isothermal process but a difficulty arises when it is extended to a non-isothermal case. The usual derivation for a non-isothermal model starts by deriving a governing equation for the phase-field from a Helmholtz free-energy functional that is applicable to an isothermal situation. The equation for the temperature field is obtained by altering the corresponding classical equation so that the latent heat production is accounted for by a source term proportional to the time derivative of the phase-field. For example, a modified equation due to Langer [11] and Caginalp [12] is given (in our notation) as,

$$\gamma \nabla^2 T = \rho c_p \frac{\partial T}{\partial t} + L \frac{\partial \phi}{\partial t}, \quad (3.5)$$

where γ is the thermal conductivity, c_p is the heat capacity per unit mass, ρ is the density and L is the latent heat per unit volume.

This procedure, apparently, does not guarantee the free energy functional to always decrease on solution paths [27]. An alternative method was proposed by Penrose and Fife [27] in which the phase-field and temperature field are derived in a thermodynamically consistent manner from a single entropy functional, \mathcal{S} given by,

$$\mathcal{S} = \int_{\Omega} \left[-\frac{1}{2} \epsilon_s^2 |\nabla \phi|^2 + s(\phi, e) \right] d\Omega, \quad (3.6)$$

where ϵ_s is a constant, $s(\phi, e)$ represents the entropy density function and e is the internal energy density. This method was used by Wang et. al. [28] to develop a class of phase-field models that are guaranteed to be thermodynamically consistent.

3.2 The relation between phase-field models and sharp interface models

In sharp interface models, boundary conditions are prescribed at the interface and interfacial physical mechanisms, such as the Gibbs-Thomson effect, are represented by these conditions explicitly. In phase-field models however, the association of the internal layers of the interface with realistic physical features is rather more implicit. It has been shown that common free boundary problems (sharp interface models) with their corresponding interfacial boundary conditions, are recovered in asymptotic limits in which the thickness of the interface goes to zero. This relationship can provide a means to relate the parameters in a phase-field model with material parameters. For the purpose of demonstrating this relationship, we summarise

the results of Wheeler et. al. [1], where they calculated the solution of the phase-field equation (3.4) with the free energy density $f(\phi, T)$, given by the form in (3.2). They consider the case of isothermal solidification of a pure material, where the solid-liquid interface is planar. The one-dimensional phase-field equation is given as,

$$\epsilon^2 \frac{d^2 \phi}{dz^2} + \frac{V}{M_1} \frac{d\phi}{dz} - f_\phi = 0, \quad (3.7)$$

where V is the velocity of the interface and $f_\phi(\phi, T)$ is given as,

$$f_\phi(\phi, T) = \frac{W}{2} \phi(\phi - 1)(2\phi - 1) + W\beta(T)\phi(1 - \phi).$$

A solution to (3.7) with the property $\phi \rightarrow 1$ as $z \rightarrow -\infty$ and $\phi \rightarrow 0$ as $z \rightarrow +\infty$ is,

$$\phi(z) = \left[1 + \exp \left(\frac{z}{\epsilon} \sqrt{\frac{W}{2}} \right) \right]^{-1}, \quad (3.8)$$

which represents ϕ through the interfacial layer. It exists only when

$$V = -M_1 \epsilon \beta(T) \sqrt{2W}. \quad (3.9)$$

Since the free energy difference between the solid and liquid phases, i.e., $W\beta(T)/6$ (evaluated from the integration of (3.2)), is often approximated as $L(T - T_M)/T_M$, then we have,

$$\beta(T) = \frac{6L(T - T_M)}{WT_M}, \quad (3.10)$$

where W is a constant, T is the interfacial temperature and T_M is the melting temperature. Equation (3.9) indicates that the interface velocity V , is related to the temperature deviation from the melting temperature, which may be interpreted as a non-equilibrium effect in which the interface moves in response to a difference in free energy density between the two phases.

From the form of the solution (3.8), it can be inferred that the characteristic interface thickness, l_i , is given by,

$$l_i = \epsilon \sqrt{\frac{2}{W}}. \quad (3.11)$$

The surface energy, σ , or the interfacial free energy is defined in [14] as **the difference, per unit area of an equilibrium interface, between the actual free energy of the system and the free energy it would have in the bulk phases** (where ϕ is uniform). Now, the total energy of the system (in 3-D) is given as follows,

$$\mathcal{F} = \int_{\Omega} \frac{\epsilon^2}{2} (\nabla \phi)^2 + f(\phi, T) d\Omega, \quad (3.12)$$

which, in 1-D reduces to,

$$\mathcal{F} = \int_{-\infty}^{+\infty} \frac{\epsilon^2}{2} \phi_z^2 + f(\phi, T) dz. \quad (3.13)$$

Using the definition for the surface energy above, we have

$$\sigma = \int_{-\infty}^{+\infty} \frac{\epsilon^2}{2} \phi_z^2 + f(\phi, T_M) dz - \int_{-\infty}^0 f(1, T_M) dz - \int_0^{+\infty} f(0, T_M) dz. \quad (3.14)$$

From definition of f in (3.3), we see that

$$f(1, T_M) = f(0, T_M) = 0,$$

which gives,

$$\sigma = \int_{-\infty}^{+\infty} \left[\frac{\epsilon^2}{2} \phi_z^2 + f(\phi, T_M) \right] dz. \quad (3.15)$$

After substituting for $\phi(z)$ given by (3.8), (3.15) evaluates to give,

$$\sigma = \frac{\epsilon \sqrt{W}}{6\sqrt{2}}. \quad (3.16)$$

It is evident from expressions (3.11) and (3.16) that the characteristic length scale of the interface and its surface energy, both depend on ϵ . It is therefore natural to expect that in the limit $\epsilon \rightarrow 0$, we will recover the corresponding free boundary problem.

The relationship between the two types of models has been investigated by Caginalp [29]. He showed that in various distinguished limits of the phase-field model, in which $\epsilon \rightarrow 0$, different free boundary problems are recovered. These free boundary problems include a variety of the classical Stefan problems and the Hele-Shaw type problems. They emerge from an asymptotic analysis of the same phase-field model, in different distinguished limits in which $\epsilon \rightarrow 0$, giving rise to different type of problems. In particular, if $W = \mathcal{O}(\epsilon^{-2})$ and $M_1 = \mathcal{O}(\epsilon^{-2})$, he obtained the following jump conditions for the temperature, at the interface, of the corresponding free boundary problem,

$$\kappa \left[\frac{\partial T}{\partial n} \right]_S^L = -LV_n, \quad (3.17)$$

and,

$$T_S = T_L = T_M - \frac{T_M \sigma}{L} \mathcal{K} - \frac{V_n}{\mu}, \quad (3.18)$$

where μ is the attachment kinetic parameter of the interface which is related to M_1 , \mathcal{K} is the curvature of the interface, κ is the dimensionless thermal diffusivity and V_n is the normal velocity of the interface into the liquid. Hence, we see from (3.18) that the Gibbs-Thomson effect (the term proportional to \mathcal{K}) and interface kinetics are featured by the phase-field model.

3.3 Anisotropy

Anisotropy plays a very important role in the macroscopic description of solidification and hence its inclusion in phase-field models is significantly vital. An interface is said to be

anisotropic when properties like the surface free energy and interface kinetics depend on the orientation of the interface. In particular, during dendritic solidification, it has been proposed in microscopic solvability theory [30, 31] that, surface energy anisotropy is important in governing the operating state of a dendrite tip.

Several methods have been proposed to include crystalline anisotropy in phase-field models. An early attempt in this direction was made by Caginalp and Fife [32] who modified the ‘square gradient term’ in the free energy functional by replacing it with a more general quadratic form with different coefficients in each coordinate direction. Another possible modification to the gradient term to include terms of higher derivatives of ϕ , was first suggested by Langer [11]. A different approach was employed by Cahn and Kikuchi [33] who included the effect of anisotropy through the inclusion of nearest-neighbour-interactions. Recently, Kobayashi [21] introduced another method on a 2-D model, which is to allow the gradient energy coefficient, namely ϵ , to depend on the local orientation of the gradient of the phase-field (i.e. $\epsilon = \xi\eta(\theta)$ where θ is the angle between the interface normal and a fixed direction, the z -axis say, $\eta(\theta)$ is a function that determines the anisotropy of the surface energy, and ξ is a parameter).

Kobayashi’s method was adopted by McFadden et. al. [34]. They introduced a similar phase-field model, in which, an asymptotic analysis in the limit $\epsilon \rightarrow 0$ was conducted. In this limit, they obtained a modified boundary condition for temperature (i.e. an anisotropic form of the Gibbs-Thomson effect given in (3.18) was recovered in 2-D), namely,

$$T = T_M + \frac{T_M}{L}(\sigma + \sigma_{\theta\theta})K - \frac{V_n}{\mu\eta(\theta)}, \quad (3.19)$$

where the term $\sigma_{\theta\theta}$ represents the second derivative with respect to θ of the surface energy. This result is equivalent to the form obtained from conventional thermodynamic arguments (Herring [35]). The corresponding result in 3-D, obtained using ξ -vector formulation, is discussed by Wheeler and McFadden [36]. Due to the dependence of the interface kinetics on ϵ (as can be seen from (3.9), this approach results in the inclusion of anisotropy not only in the surface energy, but also in the interface kinetic term.

3.4 Numerical Calculations.

In the context of numerical computation of solidification processes, phase-field models have many advantages over the free boundary formulations. The introduction of the phase-field variable into the problem allows the whole domain of solidification to be treated in the same way numerically. Phase-field models are able to show the transition between liquid and solid through the smooth (but extremely localised) changes in the phase-field variable. Moreover,

the explicit tracking of the interface (common in numerical treatments of the free boundary formulations) which usually leads to difficulties when the interface develops complicated geometries, can be avoided.

Computations on phase-field models have been conducted for dendritic solidification. Such a case requires the inclusion of anisotropy effects. In addition to the methods discussed in the last section, anisotropy may also be provided implicitly by the underlying grid used in the computation. This method was employed by Smith [37] and Umantsev et. al. [38] in early computations on the phase-field models. Recent works by Kobayashi [21] and Wheeler et. al. [22] provided successful computations of dendrites from phase-field models with anisotropy included. Kobayashi conducted calculations in 2-D on an anisotropic model of a pure material, in which, the effect of thermal noise was included at the interface. The results were remarkable in that the computer simulations exhibited realistic dendritic features such as side arm formations, coarsening effects and liquid pockets. These calculations were repeated by Wheeler et. al. using finer mesh in order to investigate the accuracy of Kobayashi's results and how they correspond with realistic growth conditions of an actual material. The results were compared with current theories of dendrite tip selection like the Ivantsov solution [39], marginal stability theory [40, 41, 42, 43] and microscopic solvability theory [31], and gave very good agreement.

3.5 Phase-field models of binary alloys

Until recently, phase-field models have been confined to solidification in pure materials. Pioneering studies of solidification in alloys using phase-field models were established by Wheeler, Boettinger and McFadden [1] and Lowen, Bechoefer and Tuckerman [44]. The former developed a phase-field model of an isothermal solidification of a binary alloy and used an analogous asymptotic analysis to the one employed by Caginalp [29] for the pure material, to show that their model recovers classical sharp interface models. However, their model predicts, in this asymptotic limit, a jump in the concentration across the interface, which increases in magnitude as the solidification velocity is increased. This contradicts the experimental results on rapid solidification. To remedy this shortcoming, they generalised their model by including a gradient energy term for the solute field, in the free energy functional (3.1). This new model [2] (which will henceforth be referred to as **Wheeler, Boettinger and McFadden 2 (WBM2)**) predicts a decrease of the interfacial concentration jump with increasing growth rate, (i.e., solute trapping), as observed in experiments.

3.5.1 WBM2 model

Wheeler et. al. [2] considered a binary alloy with components A and B , in which A is the solvent and B , the solute. The Helmholtz free-energy functional used in the model was given by,

$$\mathcal{F} = \int_{\Omega} \left[\frac{\epsilon^2}{2} |\nabla \phi|^2 + \frac{\delta^2}{2} |\nabla c|^2 + f(\phi, c, T) \right] d\Omega, \quad (3.20)$$

where c is the composition of solute. The term proportional to δ^2 in (3.20) is the so-called *solute gradient energy term*, which is absent from their earlier model [1]. Both models assumed the solid and liquid solutions of the alloy to be ideal solutions, leading to the following choice of Helmholtz free energy density function

$$f(\phi, c) = cf_B(\phi) + (1 - c)f_A(\phi) + \frac{RT}{v_m} [c \ln c + (1 - c) \ln(1 - c)], \quad (3.21)$$

where the quantities R , T and v_m are respectively the universal gas constant, the temperature of the system and the molar volume (assumed constant). The term proportional to RT/v_m is the contribution of the entropy of mixing of an ideal solution, and the functions $f_A(\phi)$ and $f_B(\phi)$ are the free energies of the pure components which take the same form as (3.2).

Governing equations postulated in both models are similar, where the phase-field, ϕ is governed by equation (3.4). An additional equation for the solute field is given by,

$$\frac{\partial c}{\partial t} = \nabla \cdot M_2 \left(c(1 - c) \nabla \frac{\delta \mathcal{F}}{\delta c} \right), \quad (3.22)$$

where \mathcal{F} is given by (3.20) and

$$\frac{\delta \mathcal{F}}{\delta c} = \frac{\partial f}{\partial c} - \delta^2 \nabla^2 c.$$

The quantity M_2 is a mobility constant and is related to the diffusion coefficient by,

$$D = M_2 \frac{RT}{v_m}. \quad (3.23)$$

It can be seen from this relation that the diffusion coefficient is the same in both liquid and solid. The diffusivities in the two phases may be distinguished by letting D be a monotonic function in ϕ that takes a value, D_L , in the liquid bulk phase, and, D_S , in the solid bulk phase [1]. We tackle this issue later in chapter 7.

The governing equations, together with the following boundary conditions (for a finite volume Ω),

$$\frac{\partial \phi}{\partial \bar{n}} = \frac{\partial c}{\partial \bar{n}} = \frac{\partial (\nabla^2 c)}{\partial \bar{n}} = 0, \quad (3.24)$$

where $\bar{\mathbf{n}}$ is the outward unit normal to the boundary of Ω , ensure consistency with the second law of thermodynamics in that they guarantee \mathcal{F} decreases monotonically in time. They also express the conservation of solute within the system.

In the 1-D formulation of the model, the solid-liquid interface is assumed to be planar and move with constant speed V in the z direction. Therefore, the solidifying alloy is assumed to occupy an infinite region $-\infty < z < +\infty$ where the origin $z = 0$ is chosen to correspond to $\phi = 1/2$; the liquid is considered to be situated in the region $z > 0$ and the solid, in the region $z < 0$. The appropriate far-field boundary conditions are therefore given by

$$(\phi, c) \rightarrow \begin{cases} (1, c_{-\infty}), & \text{as } z \rightarrow -\infty, \\ (0, c_{+\infty}), & \text{as } z \rightarrow +\infty, \end{cases} \quad (3.25)$$

where $c_{-\infty}$ and $c_{+\infty}$ are the far-field concentrations.

The non-dimensionalised versions of (3.4) and (3.22), formulated in the frame of reference attached to the moving interface are,

$$\tilde{\epsilon}^2 \frac{d^2 \phi}{d\tilde{z}^2} + \tilde{\epsilon}^2 \frac{\tilde{V}}{\tilde{m}} \frac{d\phi}{d\tilde{z}} - [\tilde{f}_\phi^{(-2)} \tilde{\epsilon}^{-2} + \tilde{f}_\phi^{(0)}] = 0, \quad (3.26)$$

$$\frac{d}{d\tilde{z}} \left\{ c(1-c) \frac{d}{d\tilde{z}} \left[-\frac{d^2 c}{d\tilde{z}^2} + (\tilde{f}_c^{(-2)} \tilde{\epsilon}^{-2} + \tilde{f}_c^{(0)}) \right] \right\} + \frac{d^2 c}{d\tilde{z}^2} + \tilde{V} \frac{dc}{d\tilde{z}} = 0, \quad (3.27)$$

where

$$\tilde{V} = \frac{V l_\delta}{D}, \quad (3.28)$$

and

$$\tilde{m} = \frac{l_\epsilon^2}{l_{M_1} l_{M_2}} = \frac{\epsilon^2 M_1}{D}, \quad (3.29)$$

are non-dimensional representations of the interface velocity and mobility of the interface, respectively. The length scale $l_\delta = \delta \sqrt{v_m / RT}$ has been chosen as the reference length scale so that $\tilde{z} = z / l_\delta$, here $\tilde{\epsilon} = \epsilon / \delta$ and the non-dimensional free energy density $\tilde{f} = f / [RT / v_m]$ takes the form

$$\tilde{f}(\phi, c) = c\tilde{f}_B + (1-c)\tilde{f}_A + c \ln c + (1-c) \ln(1-c), \quad (3.30)$$

where

$$\tilde{f}_A(\phi) = \tilde{\epsilon}^{-2} \tilde{f}_A^{(-2)}(\phi) + \tilde{f}_A^{(0)}(\phi), \quad (3.31)$$

with

$$\tilde{f}_A^{(-2)}(\phi) = 18\tilde{\sigma}_A^2\phi^2(1-\phi)^2 \ ; \ \tilde{f}_A^{(0)}(\phi) = \widetilde{\Delta F}_A\phi^2(3-2\phi), \quad (3.32)$$

$$\widetilde{\Delta F}_A = \frac{W_A\beta_A}{6[RT/v_m]} = \frac{L_A}{[RT/v_m]} \frac{(T - T_M^{(A)})}{T_M^{(A)}},$$

and

$$\frac{W_A}{[RT/v_m]} = 72\tilde{\sigma}_A^2.$$

The quantity $\tilde{\sigma}_A$ is the non-dimensional surface energy of pure A given by $\sigma_A/(\epsilon\sqrt{RT/v_m})$ where σ_A is its dimensional value and W_A has been eliminated in favour of σ_A using the relation

$$\sigma_A = \frac{\epsilon\sqrt{W_A}}{6\sqrt{2}}. \quad (3.33)$$

Similar definitions hold for the B component. We have employed the notation $\tilde{f}^{(n)} = c\tilde{f}_B^{(n)} + (1-c)\tilde{f}_A^{(n)}$ to simplify the non-dimensional expression for the free energy density.

3.5.2 Asymptotic analysis for $\epsilon/\delta \ll 1$ of WBM2

An asymptotic analysis of governing equations (3.26) and (3.27) was carried in the limit $\tilde{\epsilon} \rightarrow 0$. Two separately distinguishable regions emerged from this analysis, which were referred to as the inner region and the outer region. In the inner region, where \tilde{z} is of $O(\tilde{\epsilon}^2)$, c is constant and ϕ varies between zero and unity. The inner region is therefore associated with the solid-liquid phase transition. In the outer region, c varies but ϕ is effectively zero or unity. When the two regions were matched, the following free boundary problem was recovered, at leading order:

$$-c(1-c)\frac{d^3c}{d\tilde{z}^3} + \frac{dc}{d\tilde{z}} + \tilde{V}c = \tilde{V}c_\infty, \quad (3.34)$$

where c_∞ is the common value of the far-field concentrations $c_{-\infty}$ and $c_{+\infty}$, as required by conservation of solute for this steady-state solution. The appropriate boundary conditions at $\tilde{z} = 0$ are

$$c(0^+) = c(0^-) = \chi(\tilde{V}, T), \quad (3.35)$$

$$\left[\frac{dc}{d\tilde{z}}\right]_{\tilde{z}=0^-}^{\tilde{z}=0^+} = \Upsilon, \quad (3.36)$$

$$\left[\frac{d^2c}{d\tilde{z}^2}\right]_{\tilde{z}=0^-}^{\tilde{z}=0^+} = \widetilde{\Delta F}_A - \widetilde{\Delta F}_B, \quad (3.37)$$

where χ is the interfacial concentration which satisfies the equation,

$$\frac{\Upsilon}{2} \left(\left[\frac{dc}{d\tilde{z}} \right]_{\tilde{z}=0^-} + \left[\frac{dc}{d\tilde{z}} \right]_{\tilde{z}=0^+} \right) + \frac{\tilde{V}}{\tilde{m}} \sqrt{\chi \tilde{\sigma}_B^2 + (1 - \chi) \tilde{\sigma}_A^2} = \tilde{f}^{(0)}(0, \chi) - \tilde{f}^{(0)}(1, \chi). \quad (3.38)$$

(The interfacial concentration when the interface is stationary was found to be $c^*(T)$, and for $\Upsilon = 0$ it corresponds to the concentration for which the free energy curves of the solid and liquid intersect). The quantity Υ is given by,

$$\Upsilon = \frac{\tilde{\sigma}_B^2 - \tilde{\sigma}_A^2}{2\sigma^*}, \quad (3.39)$$

where

$$\sigma^* = \sqrt{\chi \tilde{\sigma}_B^2 + (1 - \chi) \tilde{\sigma}_A^2}, \quad (3.40)$$

is a weighted average of the surface energies of the two components. The boundary conditions express continuity of the solute field, the chemical potentials and conservation of solute.

The numerical solution of this leading order problem displayed solute trapping as \tilde{V} was increased. To investigate the dependence of the solute profile on \tilde{V} , they rescaled the non-dimensional equation (3.34) and expressed it in the \tilde{z} coordinate, where

$$\tilde{z} = \tilde{z}/[c_\infty(1 - c_\infty)/\tilde{V}]^{1/3} = z/l_\delta[c_\infty(1 - c_\infty)/\tilde{V}]^{1/3},$$

and found an explicit expression for c in the high \tilde{V} limit, showing, the maximum concentration of solute decreases like $\tilde{V}^{-2/3}$. Defining the partition coefficient, k as

$$k = \frac{\text{far - field concentration}}{\text{maximum value of the concentration}}, \quad (3.41)$$

they managed to compare their dependence of k on V with the result by Aziz [9] and found a good qualitative agreement between the two results.

3.5.3 Developments in phase-field models of binary alloys

Computation of dendrites using phase-field models of binary alloy was first presented by Warren and Boettinger [45], in which, the solid and liquid phases were allowed to have different diffusivities. Realistic growth patterns were obtained, which include the development, coarsening and coalescence of secondary and tertiary dendrite arms. Caginalp and Xie [46] analysed the sharp interface limit of a non-isothermal model and recovered the classical free boundary problems. Several models describing the eutectic growth (when two different solid phases grow from a single liquid phase) in binary alloy solidification have also been produced. These include the works by Karma [47], Elder et. al. [48] and Wheeler et. al. [49]. The latter proposed two models of a eutectic alloy. Their first model is based on a regular solution model with a

chemical miscibility gap. It suffered from the deficiency that the solid-solid surface energy is zero in the sharp interface limit. Their second model contains two parameters to distinguish the liquid phase and the two solid phases. This model is derived in a thermodynamically consistent manner which is analogous to the treatment of Wang et. al. [28].

Chapter 4

Sharp Interface Models of Solute Trapping

4.1 Introduction

A number of sharp interface solidification models have been developed in an attempt to describe the trapping phenomena that is observed during rapid solidification. The understanding of the mechanism of solute trapping is still in its infancy, but it is generally agreed that the value of the partition coefficient k , which is the measure of solute trapping, increases from its equilibrium value k_e (for $k_e < 1$) to unity as the solidification velocity is increased. Experiments on rapid solidification have also confirmed this behaviour [9, 50, 51, 52, 53]. Although different solute trapping models seem to suggest different mechanisms by which the solute trapping occurs, all of them have been successful in predicting this particular velocity dependence of k .

We will describe the principle sharp interface solute trapping models in this chapter, these are the **Stepwise Growth Model**, the **Continuous Growth Model** and the **Aperiodic Stepwise Growth Model**, all of which are due to Aziz [9]. The Continuous Growth Model is considered to be the most successful of the three (and the simplest), as it has shown very good agreement with experimental data [8, 54]. On the other hand, the Stepwise Growth model offers a more detailed atomistic description of the solute trapping process, but it fails to fit the experimental data as well. We will see later that the Continuous Growth Model is actually equivalent to a special case of the Stepwise Growth Model. The Aperiodic Stepwise Growth Model is an extension of the Continuous Growth Model in which the partition coefficient k is allowed to depend on the orientation of the interface.

All the solute trapping models mentioned above contain a fitting parameter which has the dimension of velocity, and is identified as the diffusive speed. It is defined as the ratio of the interface diffusion, D_i , to the interatomic spacing, λ , a relationship which has been confirmed by Clancy and co-workers [55, 56] in their non-equilibrium molecular dynamics computer simulations. The diffusive speed is the lower bound of the values of the solidification velocities where solute trapping becomes important. At such high velocities, the solute atoms are trapped by the advancing crystal, which gives them insufficient time to escape back into the liquid, hence the term solute trapping.

4.2 The solute trapping models.

All three models we discuss here concern a binary alloy with components A and B say, where A is treated as the solvent and B the solute. The A and B atoms compose a two-phase system, liquid and solid (crystal), where the two distinct phases are separated by a planar interface moving with a constant velocity V ($V > 0$ corresponds to solidification) with respect to the crystal lattice. The temperature of the interface is T ; we denote c_S as the mole fraction of B in the solid adjacent to the interface, and c_L as the mole fraction of B in the liquid adjacent to the interface.

4.2.1 Stepwise Growth Model.

This model assumes a planar solid-liquid interface executing instantaneous periodic jumps of length λ , the period of which is $\tau = \lambda/V$, where V is the velocity of the interface. During each jump, a monolayer of liquid, which contains all the solute atoms, is incorporated into the crystal lattice. Before the next layer is added, the solute atoms have time to diffuse back into the liquid during the time interval τ . Let c_L^i be the concentration of solute in the liquid at the interface, and c_S^i be the concentration of solute in the newly created solid monolayer. Then at time $t = 0$, $c_S^i = c_L^i$. As t increases to $t = \tau$, the value of $c_S^i(t)$ decreases as the solute atoms start to escape from the solid. When the next layer is added at time $t = \tau$, the solute atoms that have not diffused back are assumed to be embedded permanently in the solid. Therefore,

$$c_S^i(t = \tau) = c_S \quad (4.1)$$

The transport of atoms from one phase to another, has been described by Turnbull [57] using *chemical rate theory*. In this theory, a solute atom is envisioned to reach an activated transition state before it can jump across the interface (see Fig. 4.1). The energy acquired

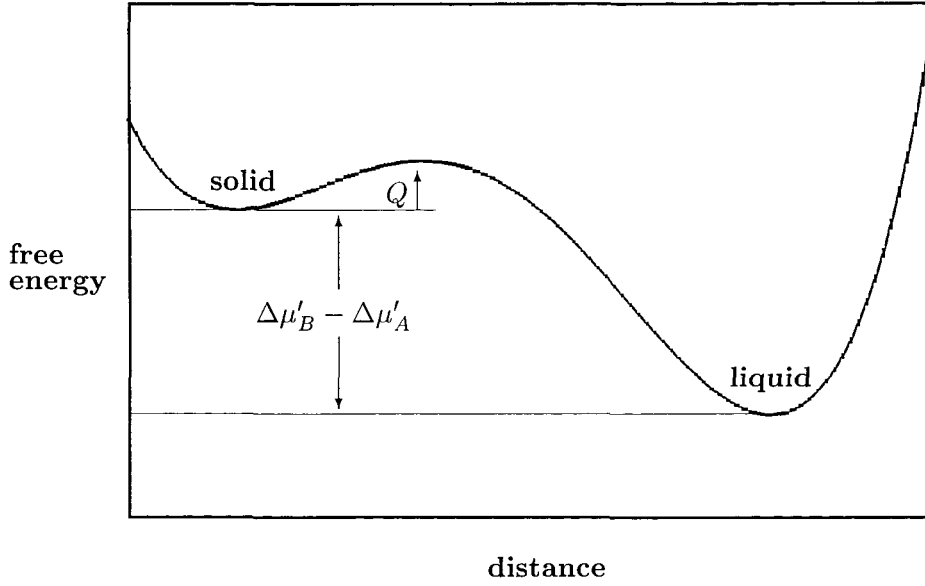


Figure 4.1: A schematic free energy diagram for a solid-liquid interface [5].

by the solute atom at this stage enables it to exchange places with a solvent atom in the opposite phase. The flux of solute atoms that escapes the solid monolayer into the liquid (for $0 < t < \tau$) is given by the rate theory as,

$$J_{S \rightarrow L} = f\nu\lambda(c_S^i(t))(1 - c_L^i)\exp(-Q/RT), \quad (4.2)$$

where f is the fraction of the interface sites where a diffusive jump can occur, ν is the attempt frequency (which is on the order of an atomic vibrational frequency), Q is the activation energy barrier for interdiffusion, T is the temperature of the undercooled interface and R is the gas constant. The reverse reaction gives the flux of solute from the liquid that is incorporated into the solid monolayer, i.e.,

$$J_{L \rightarrow S} = f\nu\lambda(c_L^i)(1 - c_S^i(t))\exp(-[Q + (\Delta\mu'_B - \Delta\mu'_A)]/RT). \quad (4.3)$$

The quantity μ' is the redistribution potential which is the difference between the actual chemical potential and the contribution from the ideal mixing entropy, e.g., for A and B in solid,

$$\mu'_A = \mu_A(1 - c_S, T) - RT \ln(1 - c_S),$$

$$\mu'_B = \mu_B(c_S, T) - RT \ln(c_S).$$

The quantity $\Delta\mu'$ denotes the difference between the values of μ' in the solid adjacent to the interface, and its value in the liquid adjacent to the interface. Notice that in both (4.2) and

(4.3) above, the second and third factors involve the concentrations of B and the concentration of A , either side of the interface. This reflects the fact that the rate of $A - B$ exchange is proportional to the concentration of B and A in the corresponding phases [19]. The final factor in the expressions represent the fraction of attempted interchanges that are successful.

Assuming negligible diffusivity in the bulk solid, conservation of mass requires the following relationship to hold

$$\frac{dc_S^i}{dt} = \frac{(J_{L \rightarrow S} - J_{S \rightarrow L})}{\lambda}. \quad (4.4)$$

Substituting for $J_{S \rightarrow L}$ and $J_{L \rightarrow S}$ in (4.4), we arrive at the following differential equation for $c_S^i(t)$,

$$\frac{dc_S^i}{dt} = \frac{-D_i}{\lambda^2} [c_S^i(t)(1 - c_L^i) - \kappa_e c_L^i(1 - c_S^i(t))], \quad (4.5)$$

where $D_i \equiv f\nu\lambda^2 \exp(-Q/RT)$ and $\kappa_e \equiv \exp[\Delta(\mu'_A - \mu'_B)]$. In the dilute solution limit, this is just,

$$\frac{dc_S^i}{dt} = \frac{-D_i}{\lambda^2} [c_S^i(t) - k_e c_L^i], \quad (4.6)$$

where k_e is the equilibrium partition coefficient. Note that, for dilute solution,

$$\kappa_e(T) = \exp[\Delta(\mu_A - \mu_B) + RT \ln k_e(T)]/RT.$$

Also, at equilibrium, $\Delta\mu_A = 0 = \Delta\mu_B$, giving $\kappa_e(T) = k_e(T)$.

Equation (4.6) with the boundary condition $c_S^i(0) = c_L^i$ has the following solution,

$$c_S^i(t) = c_L^i \left(k_e + (1 - k_e) \exp \left[\frac{-D_i t}{\lambda^2} \right] \right). \quad (4.7)$$

At time $t = \tau$, this is just

$$c_S^i(\tau) = c_S = c_L \left(k_e + (1 - k_e) \exp \left[\frac{-V_D}{V} \right] \right), \quad (4.8)$$

which gives,

$$k(v) = \frac{c_S}{c_L} = k_e + (1 - k_e) \exp(-V_D/V), \quad (4.9)$$

where the diffusive speed $V_D = D_i/\lambda$, $V = \lambda/\tau$, and c_L^i is assumed constant throughout. The form for k given in (4.9) has the right variation with velocity, i.e., it increases monotonically from its equilibrium value k_e to unity, as the velocity, V , increases.

4.2.2 Continuous Growth Model (CGM).

Continuous growth of solid occurs when the interface is diffuse, i.e., when a large part of the solid-liquid interface is favourable for the deposition of atoms from the liquid phase. This

results in a uniform growth of solid, and hence the interface advances uniformly into the liquid. Under such ideal conditions, a less atomistic approach can be used to model solidification.

Due to the almost uniform growth of solid, it is reasonable to assume a steady state in the reference frame of the interface implies that $\partial c/\partial t = 0$, where $c(z, t) = c_S^i(z, t)$, is the solidus concentration of the solute. In the reference frame of the crystal lattice, this becomes,

$$\frac{\partial c}{\partial t} + V \frac{\partial c}{\partial z} = 0. \quad (4.10)$$

Again, mass conservation requires that $\partial c/\partial t = (J_{L \rightarrow S} - J_{S \rightarrow L})/\lambda$ where the fluxes are assumed steady. Because $\partial c/\partial z = (c_L - c_S)/\lambda$, the steady state requirement becomes,

$$V(c_L - c_S) = J_{S \rightarrow L} - J_{L \rightarrow S} \equiv J_D. \quad (4.11)$$

The left hand side of equation (4.11) is defined as the interdiffusion flux J_D , which is the physical flux of solute atoms that are diffused away from the crystal lattice. It is the difference between the flux of solute atoms in the liquid adjacent to the interface, (i.e., $c_L V$), and the flux of solute atoms that are successfully incorporated into the crystal, (i.e., $c_S V$).

The rate equations (4.2) and (4.3) also apply in this case (with c_S replacing $c_S^i(t)$ and c_L replaces c_L^i), and they are inserted into equation (4.11) to give,

$$(c_L - c_S)(V/V_D) = c_S(1 - c_L) - \kappa_e c_L(1 - c_S), \quad (4.12)$$

which can be solved for the partition coefficient to give,

$$k(v) = \frac{c_S}{c_L} = \frac{V/V_D + \kappa_e}{V/V_D + 1 - (1 - \kappa_e)c_L}. \quad (4.13)$$

In the dilute limit, this is just

$$k(v) = \frac{V/V_D + \kappa_e}{V/V_D + 1}, \quad (4.14)$$

where, the velocity dependence of k is qualitatively the same as the SGM result. Equation (4.14) is referred as ‘the simple CGM result’.

This result may also be derived from the SGM model if, we assume the monolayers are added randomly in time, rather than periodically. If we define E to be the event that a given layer is not covered at time t , but during the next interval dt (where dt is very small), then the probability that E occurs is given by $P(t)dt$ where,

$$P(t) = \frac{e^{-t/\tau}}{\tau}. \quad (4.15)$$

(E may be interpreted as the *waiting time* before the next layer is added. Waiting times are commonly modelled as an exponential distribution, in this case, with parameter $1/\tau$ [58]).

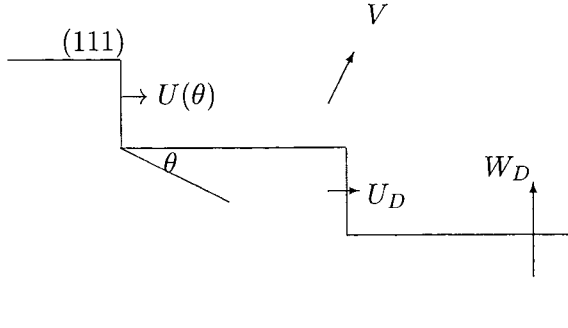


Figure 4.2: Solidification via lateral motion of (111) step, where the (111) step makes an angle $(\pi/2 - \theta)$ with the direction of the interface velocity. The flux of solute atoms escapes laterally across the moving step [20].

The partition coefficient is obtained by taking the average of k over many τ , which gives,

$$k = \int_0^\infty c_r(t)P(t)dt = \frac{V/V_D + k_e}{V/V_D + 1}, \quad (4.16)$$

which is the simple CGM result (4.14), where $c_r(t) = c_S^i(t)/c_L^i$ (see (4.7)).

4.2.3 Aperiodic Stepwise Growth Model.

This model uses the assumption that the growth of crystal occurs by the lateral motion of (111) steps (see Fig. 4.2), separated by an interval determined by the velocity and the orientation of the interface, with the additional assumption that solute atoms may diffuse away along the normal to the terraces. The trapping along the step edges, which occurs as soon as a layer is added along the steps, (i.e., at time $t = 0$), is characterised by CGM and accounted for by the following equation,

$$c_r(0) = \frac{[U(\theta)/U_D] + k_e}{[U(\theta)/U_D] + 1}, \quad (4.17)$$

where $c_r(t)$ is as defined at the end of the last section, $U = V \sin \theta$ is the growth velocity of the steps, $U_D = D_i^u/\lambda_u$ is the diffusive speed of solute atoms along the terraces (D_i^u is the coefficient of interdiffusion along the terraces and λ_u is the length of each terraces). Before the next layer is added, solute atoms have time to escape through the terraces, the decay of solute composition is given by a differential equation similar to (4.6), but with the interdiffusion coefficient equal to D_i^w , which is its value perpendicular to the terraces, the direction in which

the solute atoms are escaping. Therefore we have,

$$\frac{dc_S^i}{dt} = - \left(\frac{D_i^w}{\lambda^2} \right) [c_S^i(t) - k_e c_L^i]. \quad (4.18)$$

Integrating (4.18), using the initial condition given in (4.17), we arrive at the following expression for $c_r(t)$,

$$c_r(t) = k_e + [(\beta_u + k_e)/(\beta_u + 1)] - k_e \exp(-[D_i^w t / \lambda^2]), \quad (4.19)$$

where $\beta_u = U/U_D$. For randomly spaced ledges, we apply the same idea we used for random interval SGM (i.e., equation (4.16)) to get,

$$k = \frac{k_e + \beta_w [(\beta_u + k_e)/(\beta_u + 1)]}{\beta_w + 1}, \quad (4.20)$$

where $\beta_w = W/W_D = (V \cos \theta)/W_D$, with $W_D = D_i^w/\lambda_w$ and λ_w being the height of the terraces. Again the correct $k - V$ dependence is captured by equation (4.20), namely, k rises from its equilibrium value, k_e , when V small (β_u and β_w small), to unity when V is large (β_u and β_w large).

4.3 Experimental Results.

In order to investigate the trapping behaviour in non-equilibrium solidification experimentally, a suitable technique is needed to ensure the growth velocity is sufficiently large for the system to significantly deviate from equilibrium. The pulsed-laser melting (PLM) technique has been identified as an ideal technique for such studies. It is capable of establishing re-growth velocities in the metre-per-second regime. Early studies of non-equilibrium solidification that employ the PLM technique have met with some difficulties in the calculation of the interface velocity and the melt duration. The heat flow calculations that were used to estimate the interface velocity proved to be unreliable due to the uncertainties in the measured laser energy and pulse duration [59, 60, 61]. In his studies of solute trapping [4, 8, 20], Aziz used the transient conductance measurement (TCM) technique to measure the interface velocity during solidification. The TCM technique exploits the change in resistivity of the alloy upon melting to determine the depth to which a thin-film resistor has been melted. The velocity of the solid-liquid interface, V , can easily be measured by performing these measurements with nanosecond resolution.

The implanted impurity distribution and final profiles were determined by Rutherford Backscattering Spectrometry (RBS). In order to determine the partition coefficient, k , this final profile is compared with that from a simulated process with a known value of k . The

value of k that corresponds to the simulated profile that looks closest to the experimentally observed profile is accepted as the estimated value for k for that particular V .

The redistribution of ion-implanted solutes in the solvent films during solidification is modelled by simple diffusion and partition simulations with use of a finite element solution of the diffusion equations. The simulations treat implanted impurity profile and melt depth as functions of time for each sample. Impurity diffusion was assumed to occur in the liquid phase but neglected in the solid phase. During solidification, a fraction k of the impurity in the liquid at the interface, is incorporated into the crystal. The bulk liquid phase diffusion, D_L , and the partition coefficient during solidification were allowed to vary to fit the experimentally observed solute profile. This way, unique values for D_L and k were obtained.

The dependence of the partition coefficient on re-growth velocity is measured by performing the measurements for several values of the velocity. This is done by altering the thermal conductivity properties of each sample, which effectively alters the interface velocity.

The first experimental measurement of the partition coefficient k was carried out for Bi in Si(001) by Aziz and co-workers [8] and the result was compared with several solute trapping models. Although all the models agreed qualitatively with the dependence of k and V observed in the experiment, the Continuous Growth Model fits the data best for interface speeds of 2 and 14m/s. Subsequent work by Aziz and White [20] demonstrated the orientation dependence of k at constant V for Bi in Si. This work was carried out to resolve the matter which arose when measurements of $k(V)$ for Bi in Si(001) and Bi in Si(111), both of which were well described by CGM, gave two different values of the diffusive speed V_D . These results prompted the development of the ASGM [62]. It was shown to have an excellent quantitative agreement with experimental data.

The single fitting parameter of CGM, namely the diffusive speed V_D , was originally estimated as D_L/L where D_L is the diffusion coefficient in the bulk liquid and L is the interface width. Experiments performed by Smith, Reitano and Aziz [4] which produced measurements for both V_D and D_L for dilute concentrations of various solute in Silicon, indicated that the above estimate suggested that L varies from 6Å to 400Å. This casts doubts on the validity of the estimate, as one would expect the interface width to be independent of the solute species for dilute solute concentrations. Having realised this implication, they examined correlation between V_D (obtained through fitting $k - V$ data with CGM) and various alloy properties, for example, equilibrium partition coefficient k_e , the diffusivity of the solute in the bulk liquid D_L , the diffusivity of the solute in the solid D_S , and the maximum limit of solubility of the solute in the solvent. They found a **strong correlation between V_D and k_e** but no apparent

relation between V_D and either D_L or D_S . This is the first experimental result to relate V_D to a measurable quantity of the alloy. It provides a very useful guideline for finding a better estimate for V_D .

Chapter 5

The sharp interface limit of WBM2 when the solid-liquid interface is curved

In the near-equilibrium solidification of dilute binary alloys, the interface temperature T_I is generally obtained from the phase diagram, and its form is given by,

$$T_I = T_M^A + m_L c_L, \quad (5.1)$$

where the phase diagram is assumed linear near $c \approx 0$ (i.e., concentration of solute in the alloy is small, see chapter 2), the liquidus slope is given by m_L , and c_L denotes the liquidus concentration of solute. This assumption neglects an important equilibrium phenomenon, known as the ‘undercooling’ effect, which is a decrease in the interface temperature below the normal melting point by an amount ΔT_c say. Undercooling arises from two sources, i) the curvature of the interface - the so-called Gibbs-Thomson effect, ii) the motion of the interface - kinetic undercooling.

The Gibbs-Thomson effect arises because there is an equilibrium surface energy associated with the interface. Broadly speaking, a curved interface has a greater surface energy, thus, the energy of the system is increased by the effect. This increase in energy is balanced by a decrease in the solid bulk free energy relative to the liquid which results in the interface temperature being reduced [63]. The amount ΔT_c has been shown to be proportional to the **curvature** of the interface and the constant of proportionality involves the surface energy, i.e.,

$$\Delta T_c = T_M \Gamma \mathcal{K}, \quad (5.2)$$

where Γ is the capillary constant defined as the ratio between the surface energy and the latent heat, and \mathcal{K} is the curvature of the interface. The relationship in (5.2) is commonly called the *Gibbs-Thomson Relation* [12, 63, 64].

The undercooling effect is also observed to occur in a system that deviates from equilibrium. In such cases, the undercooling provides the driving force for growth, thus the greater the undercooling (i.e. the driving force), the greater the growth rate. It is referred to as the ‘kinetic undercooling’, ΔT_k say, and its magnitude is proportional to the growth rate [63, 29]. In general, ΔT_k is given by,

$$\Delta T_k = \frac{V}{\mu_A}, \quad (5.3)$$

where μ_A is the so-called attachment kinetic parameter.

In this chapter, we apply the WBM2 model to a solidification process with a **curved** solid-liquid interface. The governing equations are expressed in an appropriate curvilinear coordinates, and non-dimensionalised with respect to the $l_\delta = \delta\sqrt{v_m/RT}$ length scale. In the sharp interface limit, boundary conditions across the interface are obtained, from which we find an expression for the interface temperature. This expression is observed to capture both the Gibbs-Thomson effect and the kinetic undercooling effect.

5.1 The governing equations

We consider the model described in section 3.5.1, where the governing equations are given by,

$$\frac{\partial \phi}{\partial t} = -M_1 \frac{\delta \mathcal{F}}{\delta \phi}, \quad (5.4)$$

$$\frac{\partial c}{\partial t} = \nabla \cdot M_2 \left(c(1-c) \nabla \frac{\delta \mathcal{F}}{\delta c} \right), \quad (5.5)$$

where

$$\begin{aligned} \frac{\delta \mathcal{F}}{\delta \phi} &= \frac{\partial f}{\partial \phi} - \epsilon^2 \nabla^2 \phi, \\ \frac{\delta \mathcal{F}}{\delta c} &= \frac{\partial f}{\partial c} - \delta^2 \nabla^2 c, \end{aligned}$$

and f and \mathcal{F} are given by (3.21) and (3.20). The material is assumed to be of a finite volume, and situated in the region Ω , where the conditions at the boundary of Ω is given by,

$$\frac{\partial \phi}{\partial \bar{\mathbf{n}}} = \frac{\partial c}{\partial \bar{\mathbf{n}}} = \frac{\partial (\nabla^2 c)}{\partial \bar{\mathbf{n}}} = 0,$$

where $\bar{\mathbf{n}}$ is the outward unit normal to this boundary.

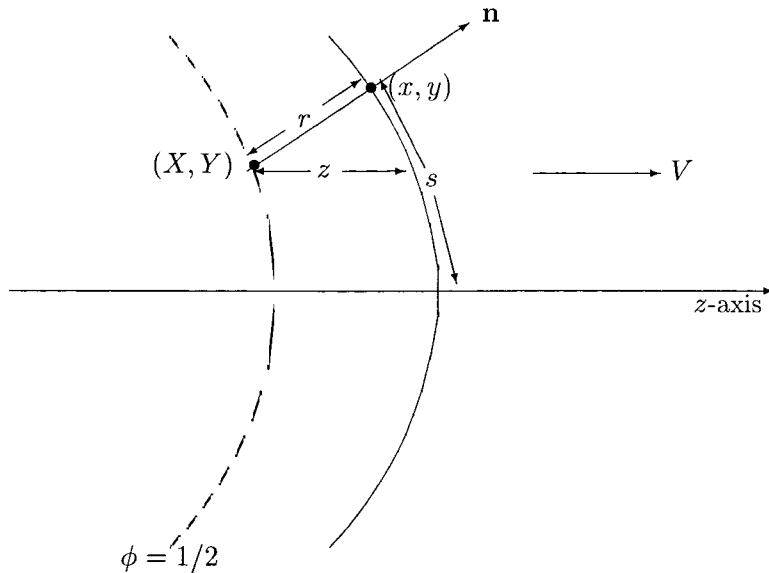


Figure 5.1: A schematic diagram of the moving curved interface, showing the direction of the coordinates (r, s) with respect to the Cartesian coordinates.

We introduce the curvilinear coordinates (r, s) local to the moving interface. Specifically, we let $r = 0$ represent $\phi = 1/2$ with r and s coordinates measured normal to and along $\phi = 1/2$ (see Fig. 5.1), i.e., the liquid phase occupies the region $r > 0$ and the solid phase occupies the region $r < 0$. The coordinate transformation from the Cartesian coordinates to the curvilinear coordinates are carried out using the procedure employed by McFadden et. al. [34], the details of which can be found in Appendix A. We have used tensor calculus to transform the gradient ∇ and the Laplacian ∇^2 into the new coordinate system (r, s) , from which the following relations are obtained,

$$\nabla\psi = \psi_r \hat{r} + \frac{1}{h^2} \psi_s \hat{s}, \quad (5.6)$$

and

$$\nabla^2\psi = \frac{1}{h} \left[(h\psi_r)_r + \left(\frac{1}{h} \psi_s \right)_s \right], \quad (5.7)$$

where ψ is an arbitrarily chosen differentiable function, $h(r, s)$ is the Jacobian, $\det \begin{pmatrix} z_r & z_s \\ x_r & x_s \end{pmatrix}$, and is given in [34] as,

$$h = 1 + r\mathcal{K}(s).$$

Here, \mathcal{K} denotes the local curvature of the interface.

We use (5.6) and (5.7) to transform the governing equations (5.4) and (5.5) to the (r, s) coordinate system. Again, we need to express the equations in the local moving reference frame of the interface, in which case, we find it is appropriate to consider the motion of the interface along its normal, with normal velocity denoted by V_n . In the asymptotic limit $\epsilon/\delta \rightarrow 0$ an interfacial layer forms and variations across the layer (with respect to r) dominate over those along the layer (with respect to s). Thus, for simplicity of presentation, we only retain the partial r derivatives in which case the governing equations are

$$\epsilon^2 \frac{\partial^2 \phi}{\partial r^2} + \left(\epsilon^2 \frac{h_r}{h} + \frac{V_n}{M_1} \right) \frac{\partial \phi}{\partial r} - f_\phi = 0, \quad (5.8)$$

and

$$\begin{aligned} \frac{\partial}{\partial r} \left(c(1-c) \frac{\partial}{\partial r} \left[-\delta^2 \frac{\partial^2 c}{\partial r^2} - \delta^2 \frac{h_r}{h} \frac{\partial c}{\partial r} + f_c \right] \right) \\ + c(1-c) \frac{h_r}{h} \frac{\partial}{\partial r} \left[-\delta^2 \frac{\partial^2 c}{\partial r^2} - \delta^2 \frac{h_r}{h} \frac{\partial c}{\partial r} + f_c \right] + \frac{V_n}{M_2} \frac{\partial c}{\partial r} = 0. \end{aligned} \quad (5.9)$$

The equations above are non-dimensionalised with respect to the l_δ length scale where the resulting non-dimensional representation of the equations is given below,

$$\tilde{\epsilon}^2 \frac{\partial^2 \phi}{\partial \tilde{r}^2} + \tilde{\epsilon}^2 \left(\tilde{\mathcal{K}} + \frac{\tilde{V}_n}{\tilde{m}} \right) \frac{\partial \phi}{\partial \tilde{r}} - [\tilde{\epsilon}^{-2} \tilde{f}_\phi^{(-2)} + \tilde{f}_\phi^{(0)}] = 0, \quad (5.10)$$

$$\begin{aligned} \frac{\partial}{\partial \tilde{r}} \left(c(1-c) \frac{\partial}{\partial \tilde{r}} \left[-\frac{\partial^2 c}{\partial \tilde{r}^2} - \tilde{\mathcal{K}} \frac{\partial c}{\partial \tilde{r}} + \tilde{\epsilon}^{-2} \tilde{f}_c^{(-2)} + \tilde{f}_c^{(0)} \right] \right) + \frac{\partial^2 c}{\partial \tilde{r}^2} + \\ \tilde{\mathcal{K}} \left(c(1-c) \frac{\partial}{\partial \tilde{r}} \left[-\frac{\partial^2 c}{\partial \tilde{r}^2} - \tilde{\mathcal{K}} \frac{\partial c}{\partial \tilde{r}} + \tilde{\epsilon}^{-2} \tilde{f}_c^{(-2)} + \tilde{f}_c^{(0)} \right] \right) + (\tilde{\mathcal{K}} + \tilde{V}_n) \frac{\partial c}{\partial \tilde{r}} = 0, \end{aligned} \quad (5.11)$$

where

$$\tilde{\mathcal{K}} = \mathcal{K} l_\delta, \quad \tilde{r} = r/l_\delta,$$

and all the other non-dimensional quantities are defined as in section 3.5.1. We have assumed the interface is thin, i.e. \tilde{r} is small, that h_r/h may be approximated as $\tilde{\mathcal{K}}$.

There are two characteristic length scales that are important in this problem. They are,

$$l_\epsilon = \epsilon \sqrt{\frac{v_m}{RT}}, \quad l_\delta = \delta \sqrt{\frac{v_m}{RT}}, \quad (5.12)$$

which characterise the transition layer thickness of the phase-field and the solute field in the interfacial zone respectively [2]. It was noted by Wheeler et. al. [1] (see also, section 3.2) that the sharp interface limit is equivalent to the limit $\epsilon \rightarrow 0$. In our analysis, we will employ the equivalent limit of $\tilde{\epsilon} \rightarrow 0$, with δ constant, following a similar analysis in [2]. In this limit, the

ratio l_ϵ/l_δ reduces to zero because the phase-field, ϕ , changes more rapidly from its value in the liquid to that in the solid, than the solute field c .

5.2 Asymptotic analysis in the limit $\epsilon/\delta \rightarrow 0$

The asymptotic analysis carried out in this section follows a similar procedure used by Wheeler et. al. [1, 2] for a planar interface, which we described in chapter 3. In both of their analyses, it was observed that as $\tilde{\epsilon} \rightarrow 0$, an interior layer is formed within the region occupied by the alloy. Outside the layer, the solute field variable varies while the phase-field variable was found to be either 0 (when $\tilde{r} > 0$) or 1 (when $\tilde{r} < 0$). Significant variations in ϕ are only observed inside the layer. This layer, which represents the interface, is called the ‘inner region’ and the region outside is called the ‘outer region’. The solutions in the inner region are matched with solutions in the outer region, thereby, provide a set of ‘matching conditions’ which gives rise to a set of boundary conditions across the interface. The matching procedure is described in detail in section 5.2.3.

5.2.1 The outer region

The solutions in this region are expressed as regular perturbation series in $\tilde{\epsilon}^2$ to give,

$$\phi = \phi^{(0)}(\tilde{r}) + \tilde{\epsilon}^2 \phi^{(2)}(\tilde{r}) + \mathcal{O}(\tilde{\epsilon}^4), \quad (5.13)$$

$$c = c^{(0)}(\tilde{r}) + \tilde{\epsilon}^2 c^{(2)}(\tilde{r}) + \mathcal{O}(\tilde{\epsilon}^4). \quad (5.14)$$

The expansions above are substituted into the governing equations (5.10) and (5.11), where at leading order in $\tilde{\epsilon}^2$, the phase-field equation is given as,

$$\tilde{f}_\phi^{(-2)}(\phi^{(0)}, c^{(0)}) = 0, \quad (5.15)$$

which solves to give $\phi = 0$ when $\tilde{r} > 0$ (i.e. in the liquid), and $\phi = 1$ when $\tilde{r} < 0$ (i.e. in the solid). The corresponding leading order equation for the solute field is,

$$\begin{aligned} \frac{\partial}{\partial \tilde{r}} \left\{ c^{(0)}(1 - c^{(0)}) \frac{\partial}{\partial \tilde{r}} \left[-\frac{\partial^2 c^{(0)}}{\partial \tilde{r}^2} - \tilde{\mathcal{K}} \frac{\partial c^{(0)}}{\partial \tilde{r}} + (c^{(0)} \widetilde{\Delta F}_B - (1 - c^{(0)}) \widetilde{\Delta F}_A) \right] \right\} \\ + \tilde{\mathcal{K}} \left\{ c^{(0)}(1 - c^{(0)}) \frac{\partial}{\partial \tilde{r}} \left[-\frac{\partial^2 c^{(0)}}{\partial \tilde{r}^2} - \tilde{\mathcal{K}} \frac{\partial c^{(0)}}{\partial \tilde{r}} + (c^{(0)} \widetilde{\Delta F}_B + (1 - c^{(0)}) \widetilde{\Delta F}_A) \right] \right\} \\ + \frac{\partial^2 c^{(0)}}{\partial \tilde{r}^2} + (\tilde{\mathcal{K}} + \tilde{V}_n) \frac{\partial c^{(0)}}{\partial \tilde{r}} = 0, \end{aligned} \quad (5.16)$$

where $\widetilde{\Delta F}_A$ and $\widetilde{\Delta F}_B$ are defined in section 3.5.1.

5.2.2 The inner region

The rapid change in ϕ in this region suggests that it is characterised by a much smaller length scale than l_δ . Thus we rescale \tilde{r} with $\tilde{\epsilon}^2$ and introduce the stretched variable $\tilde{\rho} = \tilde{\epsilon}^{-2}\tilde{r}$. The solutions in this region are denoted by hats and they are expressed as regular expansions in $\tilde{\epsilon}^2$, i.e.,

$$\hat{\phi} = \hat{\phi}^{(0)}(\tilde{\rho}) + \tilde{\epsilon}^2 \hat{\phi}^{(2)}(\tilde{\rho}) + \mathcal{O}(\tilde{\epsilon}^4), \quad (5.17)$$

$$\hat{c} = \hat{c}^{(0)}(\tilde{\rho}) + \tilde{\epsilon}^2 \hat{c}^{(2)}(\tilde{\rho}) + \mathcal{O}(\tilde{\epsilon}^4). \quad (5.18)$$

The expansions are substituted in the governing equations and we obtain the following set of equations,

$$\frac{\partial^2 \hat{\phi}}{\partial \tilde{\rho}^2} + \tilde{\epsilon}^2 \left(\tilde{\mathcal{K}} + \frac{\tilde{V}_n}{\tilde{m}} \right) \frac{\partial \hat{\phi}}{\partial \tilde{\rho}} - \left(\tilde{f}_\phi^{(-2)} + \tilde{\epsilon}^2 \tilde{f}_\phi^{(0)} \right) = 0, \quad (5.19)$$

and

$$\begin{aligned} & \frac{\partial}{\partial \tilde{\rho}} \left\{ \hat{c}(1 - \hat{c}) \frac{\partial}{\partial \tilde{\rho}} \left[-\frac{\partial^2 \hat{c}}{\partial \tilde{\rho}^2} - \tilde{\epsilon}^2 \tilde{\mathcal{K}} \frac{\partial \hat{c}}{\partial \tilde{\rho}} + \tilde{\epsilon}^2 \tilde{f}_c^{(-2)} + \tilde{\epsilon}^4 \tilde{f}_c^{(0)} \right] \right\} \\ & + \tilde{\epsilon}^2 \tilde{\mathcal{K}} \left\{ \hat{c}(1 - \hat{c}) \frac{\partial}{\partial \tilde{\rho}} \left[-\frac{\partial^2 \hat{c}}{\partial \tilde{\rho}^2} - \tilde{\epsilon}^2 \tilde{\mathcal{K}} \frac{\partial \hat{c}}{\partial \tilde{\rho}} + \tilde{\epsilon}^2 \tilde{f}_c^{(-2)} + \tilde{\epsilon}^4 \tilde{f}_c^{(0)} \right] \right\} \\ & + \tilde{\epsilon}^4 \frac{\partial^2 \hat{c}}{\partial \tilde{\rho}^2} + \tilde{\epsilon}^6 \left(\tilde{\mathcal{K}} + \tilde{V}_n \right) \frac{\partial \hat{c}}{\partial \tilde{\rho}} = 0. \end{aligned} \quad (5.20)$$

The appropriate boundary conditions in this region is given by the following matching conditions,

$$(\hat{\phi}, \hat{c}) \rightarrow \begin{cases} (0, c_{+\infty}) & \text{as } \tilde{\rho} \rightarrow +\infty, \\ (1, c_{-\infty}) & \text{as } \tilde{\rho} \rightarrow -\infty, \end{cases} \quad (5.21)$$

where $c_{+\infty}$ and $c_{-\infty}$ are constants representing the solute concentrations in the liquid and solid phases of the outer region respectively.

Equations (5.19) and (5.20) express the governing equations as regular perturbations in $\tilde{\epsilon}$ where the leading-order equations in $\tilde{\epsilon}^2$ are found to be the following,

$$\frac{\partial^2 \hat{\phi}^{(0)}}{\partial \tilde{\rho}^2} - \tilde{f}_\phi^{(-2)}(\hat{\phi}^{(0)}, \hat{c}^{(0)}) = 0, \quad (5.22)$$

$$\frac{\partial}{\partial \tilde{\rho}} \left[\hat{c}^{(0)}(1 - \hat{c}^{(0)}) \frac{\partial}{\partial \tilde{\rho}} \left(-\frac{\partial^2 \hat{c}^{(0)}}{\partial \tilde{\rho}^2} \right) \right] = 0. \quad (5.23)$$

Equation (5.23) is integrated twice, and the matching condition (5.21) is applied to give

$$\frac{\partial \hat{c}^{(0)}}{\partial \tilde{\rho}} = 0, \quad (5.24)$$

which has solutions that are constants in $\tilde{\rho}$, i.e.,

$$\hat{c}^{(0)}(\tilde{\rho}) = \hat{c}^{(0)}(-\infty) = \hat{c}^{(0)}(+\infty) = \chi(\tilde{V}_n, T, \tilde{\mathcal{K}}). \quad (5.25)$$

The leading order phase field equation (5.22) is solved to give the following leading order solution,

$$\hat{\phi}^{(0)}(\tilde{\rho}) = \frac{1}{2}[1 - \tanh(3\tilde{\sigma}_\chi\tilde{\rho})], \quad (5.26)$$

where $\tilde{\sigma}_\chi$ represents the weighted average of the surface energies of the two components of the alloy at the interface, its value is given by,

$$\tilde{\sigma}_\chi = \sqrt{\chi\tilde{\sigma}_B^2 + (1-\chi)\tilde{\sigma}_A^2}.$$

Similarly, at the next order, i.e., $\mathcal{O}(\tilde{\epsilon}^2)$, we obtain the following pair of equations,

$$\frac{\partial^2 \hat{\phi}^{(2)}}{\partial \tilde{\rho}^2} + \left(\tilde{\kappa} + \frac{\tilde{V}_n}{\tilde{m}} \right) \frac{\partial \hat{\phi}^{(0)}}{\partial \tilde{\rho}} - \hat{\phi}^{(2)} \tilde{f}_{\phi\phi}^{(-2)}(\hat{\phi}^{(0)}, \hat{c}^{(0)}) - \hat{c}^{(2)} \tilde{f}_{\phi c}^{(-2)}(\hat{\phi}^{(0)}, \hat{c}^{(0)}) - \tilde{f}_{\phi}^{(0)}(\hat{\phi}^{(0)}, \hat{c}^{(0)}) = 0, \quad (5.27)$$

and

$$\frac{\partial}{\partial \tilde{\rho}} \left\{ \hat{c}^{(0)}(1 - \hat{c}^{(0)}) \frac{\partial}{\partial \tilde{\rho}} \left[-\frac{\partial^2 \hat{c}^{(2)}}{\partial \tilde{\rho}^2} - \tilde{\kappa} \frac{\partial \hat{c}^{(0)}}{\partial \tilde{\rho}} + \tilde{f}_c^{(-2)}(\hat{\phi}^{(0)}, \hat{c}^{(0)}) \right] \right\} = 0, \quad (5.28)$$

The solute equation (5.28) is integrated twice and the matching conditions are applied to give,

$$\frac{\partial^2 \hat{c}^{(2)}}{\partial \tilde{\rho}^2} = \tilde{f}_c^{(-2)}(\hat{\phi}^{(0)}, \hat{c}^{(0)}), \quad (5.29)$$

which is integrated once again to give,

$$\left[\frac{\partial \hat{c}^{(2)}}{\partial \tilde{\rho}} \right]_{\tilde{\rho}=-\infty}^{\tilde{\rho}=+\infty} = \tilde{\Upsilon} = \frac{\tilde{\sigma}_B^2 - \tilde{\sigma}_A^2}{2\tilde{\sigma}_\chi}. \quad (5.30)$$

The first-order equations (5.27) and (5.29) can be rewritten as,

$$\mathcal{L}(\hat{\Phi}^{(2)}) = \begin{bmatrix} -\left(\tilde{\kappa} + \frac{\tilde{V}_n}{\tilde{m}} \right) \frac{\partial \hat{\phi}^{(0)}}{\partial \tilde{\rho}} + \tilde{f}_{\phi}^{(0)}(\hat{\phi}^{(0)}, \hat{c}^{(0)}) \\ \tilde{f}_c^{(-2)}(\hat{\phi}^{(0)}, \hat{c}^{(0)}) \end{bmatrix} \quad (5.31)$$

where \mathcal{L} is a linear operator acting on vector $\hat{\Phi}^{(2)}$, where

$$\hat{\Phi}^{(2)} = \begin{bmatrix} \hat{\phi}^{(2)} \\ \hat{c}^{(2)} \end{bmatrix}, \quad (5.32)$$

$$\mathcal{L}(\hat{\Phi}^{(2)}) = \begin{bmatrix} \frac{\partial^2 \hat{\phi}^{(2)}}{\partial \tilde{\rho}^2} - \hat{\phi}^{(2)} \tilde{f}_{\phi\phi}^{(-2)}(\hat{\phi}^{(0)}, \hat{c}^{(0)}) - \hat{c}^{(2)} \tilde{f}_{c\phi}^{(-2)}(\hat{\phi}^{(0)}, \hat{c}^{(0)}), \\ \frac{\partial^2 \hat{c}^{(2)}}{\partial \tilde{\rho}^2} \end{bmatrix}. \quad (5.33)$$

Notice that \mathcal{L} is a **self-adjoint** operator because the following relationship holds for vectors Ψ_1 and Ψ_2 , whose respective i th entries are suitably differentiable functions ψ_1^i and ψ_2^i say,

$$\mathcal{L}(\Psi_1) \cdot \Psi_2 = \Psi_1 \cdot \mathcal{L}(\Psi_2), \quad (5.34)$$

where the inner product is defined below as,

$$\begin{aligned}\Psi_1 \cdot \Psi_2 &= \psi_1^1 \cdot \psi_2^1 + \psi_1^2 \cdot \psi_2^2, \\ &= \int_{-\infty}^{+\infty} (\psi_1^1 \psi_2^1 + \psi_1^2 \psi_2^2) d\tilde{\rho},\end{aligned}\tag{5.35}$$

where, in this case, $\Psi_1 = (\psi_1^1, \psi_1^2)^T$ and $\Psi_2 = (\psi_2^1, \psi_2^2)^T$. Also, after differentiating equations (5.22) and (5.24) once with respect to $\tilde{\rho}$, the resulting homogeneous equations are found to be of the forms,

$$\mathcal{L} \left[\frac{\partial \hat{\Phi}^{(0)}}{\partial \tilde{\rho}} \right] = \mathbf{0},\tag{5.36}$$

where

$$\hat{\Phi}^{(0)} = \begin{bmatrix} \hat{\phi}^{(0)} \\ \hat{c}^{(0)} \end{bmatrix}.$$

Equation (5.36), together with the fact that \mathcal{L} is self-adjoint, leads to the following **solvability condition**,

$$\frac{\partial \hat{\Phi}^{(0)}}{\partial \tilde{\rho}} \cdot \mathcal{L}(\hat{\Phi}^{(2)}) = 0.\tag{5.37}$$

The vector $\mathcal{L}(\hat{\Phi}^{(2)})$ in (5.37) is replaced with the vector in the right-hand side of equation (5.31), and after computing the inner product, we arrive at the equation below, which relates the temperature to the curvature term,

$$-\left(\tilde{\kappa} + \frac{\tilde{V}_n}{\tilde{m}}\right) \tilde{\sigma}_\chi - \left[\frac{1}{2} \left(\frac{\partial \hat{c}^{(2)}}{\partial \tilde{\rho}} \right)^2 \right]_{-\infty}^{+\infty} + [\tilde{f}^{(0)}(\hat{\phi}^{(0)}, \hat{c}^{(0)})]_{-\infty}^{+\infty} = 0.\tag{5.38}$$

Proceeding to the next order, we find the $\mathcal{O}(\epsilon^4)$ equation for the solute field, which is given by,

$$\begin{aligned}\frac{\partial}{\partial \tilde{\rho}} \left\{ \chi(1-\chi) \left[-\frac{\partial^2 \hat{c}^{(4)}}{\partial \tilde{\rho}^2} - \tilde{\kappa} \frac{\partial \hat{c}^{(2)}}{\partial \tilde{\rho}} + \hat{\phi}^{(2)} \tilde{f}_{c\phi}^{(-2)}(\hat{\phi}^{(0)}, \hat{c}^{(0)}) + \hat{c}^{(2)} \tilde{f}_{cc}^{(-2)}(\hat{\phi}^{(0)}, \hat{c}^{(0)}) + \tilde{f}_c^{(0)}(\hat{\phi}^{(0)}, \hat{c}^{(0)}) \right] \right\} \\ - \tilde{\kappa} \chi(1-\chi) \frac{\partial^3 \hat{c}^{(2)}}{\partial \tilde{\rho}^3} + \frac{\partial^2 \hat{c}^{(0)}}{\partial \tilde{\rho}^2} - \tilde{\kappa}^2 \chi(1-\chi) \frac{\partial^2 \hat{c}^{(0)}}{\partial \tilde{\rho}^2} + \tilde{\kappa} \chi(1-\chi) \frac{\partial}{\partial \tilde{\rho}} [\tilde{f}_c^{(-2)}(\hat{\phi}^{(0)}, \hat{c}^{(0)})] = 0,\end{aligned}\tag{5.39}$$

After being integrated once, applying the matching conditions accordingly, we are left with,

$$\left[\frac{\partial^2 \hat{c}^{(4)}}{\partial \tilde{\rho}^2} \right]_{\tilde{\rho}=-\infty}^{\tilde{\rho}=+\infty} = [\tilde{f}_c^{(0)}(\hat{\phi}^{(0)}, \hat{c}^{(0)})]_{\tilde{\rho}=-\infty}^{\tilde{\rho}=+\infty} - \tilde{\kappa} \tilde{\Upsilon}.\tag{5.40}$$

Equations (5.25), (5.30), (5.38) and (5.40) are matched with the corresponding solutions in the outer region; this is explained in detail in the next section.

5.2.3 Matched asymptotic analysis

The existence of the outer and inner region implies that there is an overlap domain in which the inner solutions and the outer solutions are equivalent. The matching principle states that [65],

Inner representation of the outer expansion = outer representation of the inner expansion.

In our notation, this means,

$$\lim_{\tilde{r} \rightarrow 0^-} c(\tilde{r}) = \lim_{\tilde{\rho} \rightarrow -\infty} \hat{c}(\tilde{\rho}), \quad (5.41)$$

$$\lim_{\tilde{r} \rightarrow 0^+} c(\tilde{r}) = \lim_{\tilde{\rho} \rightarrow +\infty} \hat{c}(\tilde{\rho}), \quad (5.42)$$

respectively, and similarly for ϕ . This principle allows us to find a set of boundary condition for the solute field across the interface. More precisely, we obtain a set of ‘jump conditions’ for c and its derivatives, by matching equations (5.25), (5.30) and (5.40) with the corresponding equations in the outer region.

The inner representation of the outer expansion of the solute field is derived by first, expanding the regular expansion for $c(\tilde{r})$ (given in equation (5.14)) in the outer region, using a Taylor series, in terms of $\tilde{r} = \tilde{\epsilon}^2 \tilde{\rho}$, and then, taking the ‘inner limit’ of this new expansion. This is the limit of $\tilde{\epsilon}^2 \rightarrow 0$ with $\tilde{\rho}$ fixed (i.e. for example, on the solid side, this is the limit $\tilde{r} \rightarrow 0^-$). Thus, the inner representation of the expansion, on the solid side, is given by

$$\begin{aligned} \lim_{\tilde{r} \rightarrow 0^-} c(\tilde{r}) = & c^{(0)}(0^-) + \tilde{\epsilon}^2 \left\{ c^{(2)}(0^-) + \tilde{\rho} \left[\frac{\partial c^{(0)}}{\partial \tilde{r}} \right]_{\tilde{r}=0^-} \right\} \\ & + \tilde{\epsilon}^4 \left\{ c^{(4)}(0^-) + \frac{\tilde{\rho}^2}{2} \left[\frac{\partial^2 c^{(0)}}{\partial \tilde{r}^2} \right]_{\tilde{r}=0^-} + \tilde{\rho} \left[\frac{\partial c^{(2)}}{\partial \tilde{r}} \right]_{\tilde{r}=0^-} \right\} + \mathcal{O}(\tilde{\epsilon}^6). \end{aligned} \quad (5.43)$$

The inner representation of the expansion in the liquid is obtained similarly, where the limit $\tilde{\epsilon}^2 \rightarrow 0$, with $\tilde{\rho}$ fixed, is equivalent to the limit $\tilde{r} \rightarrow 0^+$.

Similarly, the outer representation of the inner expansion for c is obtained by taking the ‘outer limit’ of the inner expansion given in (5.18). This is the limit of $\tilde{\epsilon}^2 \rightarrow 0$ with \tilde{r} fixed (i.e. on the solid side, this is the limit $\tilde{\rho} \rightarrow -\infty$). As a result, we arrive at the following outer representation of the inner solution \hat{c} (on the solid side),

$$\lim_{\tilde{\rho} \rightarrow -\infty} \hat{c}(\tilde{\rho}) = \hat{c}^{(0)}(-\infty) + \tilde{\epsilon}^2 \hat{c}^{(2)}(-\infty) + \tilde{\epsilon}^4 \hat{c}^{(4)}(-\infty) + \mathcal{O}(\tilde{\epsilon}^6). \quad (5.44)$$

Again, the outer representation of the inner expansion on the liquid side is obtained by taking the limit $\tilde{\rho} \rightarrow +\infty$.

Now, the matching principle (5.41) and (5.42), also implies that the outer limit of the derivatives of \hat{c} with respect to $\tilde{\rho}$, is equal to the inner limit of the derivatives of c with respect to $\tilde{\rho}$, i.e., on the solid side we have,

$$\lim_{\tilde{\rho} \rightarrow -\infty} \frac{\partial \hat{c}}{\partial \tilde{\rho}} = \lim_{\tilde{r} \rightarrow 0^-} \frac{\partial c}{\partial \tilde{\rho}}, \quad \lim_{\tilde{\rho} \rightarrow -\infty} \frac{\partial^2 \hat{c}}{\partial \tilde{\rho}^2} = \lim_{\tilde{r} \rightarrow 0^-} \frac{\partial^2 c}{\partial \tilde{\rho}^2}, \quad \text{etc.} \quad (5.45)$$

Similar equations are implied on the liquid side.

We proceed by matching equations (5.43) and (5.44), and their derivatives with respect to $\tilde{\rho}$, from which we find,

$$\hat{c}^{(0)}(\tilde{\rho} = -\infty) = c^{(0)}(\tilde{r} = 0^-), \quad (5.46)$$

$$\left[\frac{\partial \hat{c}^{(2)}}{\partial \tilde{\rho}} \right]_{\tilde{\rho} = -\infty} = \left[\frac{\partial c^{(0)}}{\partial \tilde{r}} \right]_{\tilde{r} = 0^-}, \quad (5.47)$$

$$\left[\frac{\partial^2 \hat{c}^{(4)}}{\partial \tilde{\rho}^2} \right]_{\tilde{\rho} = -\infty} = \left[\frac{\partial^2 c^{(0)}}{\partial \tilde{r}^2} \right]_{\tilde{r} = 0^-}. \quad (5.48)$$

The corresponding equations on the liquid side are also matched to give a similar set of equations to the above. The outer representation of $\hat{c}^{(0)}$, $\partial \hat{c}^{(2)}/\partial \tilde{\rho}$ and $\partial^2 \hat{c}^{(4)}/\partial \tilde{\rho}^4$ on both sides of the interface are substituted into equations (5.25), (5.30) and (5.40) respectively, to give the following boundary conditions across the interface,

$$c(0^+) = c(0^-) = \chi(\tilde{V}_n, T, \tilde{\mathcal{K}}), \quad (5.49)$$

$$\left[\frac{\partial c}{\partial \tilde{r}} \right]_{\tilde{r} = 0^-}^{\tilde{r} = 0^+} = \tilde{\Upsilon}, \quad (5.50)$$

$$\left[\frac{\partial^2 c}{\partial \tilde{r}^2} \right]_{\tilde{r} = 0^-}^{\tilde{r} = 0^+} = \tilde{f}_c^{(0)}(0, \chi) - \tilde{f}_c^{(0)}(1, \chi) - \tilde{\mathcal{K}}\tilde{\Upsilon}, \quad (5.51)$$

where 0^+ and 0^- represent the limits \tilde{r} tends to zero, from above and below respectively. The solvability condition (5.38) is matched with the solutions in the outer region to give

$$\frac{\tilde{\Upsilon}}{2} \left(\left[\frac{\partial c}{\partial \tilde{r}} \right]_{\tilde{r} = 0^-} + \left[\frac{\partial c}{\partial \tilde{r}} \right]_{\tilde{r} = 0^+} \right) + \left(\tilde{\mathcal{K}} + \frac{\tilde{V}_n}{\tilde{m}} \right) \sqrt{\chi \tilde{\sigma}_B^2 + (1 - \chi) \tilde{\sigma}_A^2} = \tilde{f}^{(0)}(0, \chi) - \tilde{f}^{(0)}(1, \chi), \quad (5.52)$$

which provides an equation for the interface temperature T in terms of the interface concentration χ and the dimensionless interface curvature $\tilde{\mathcal{K}}$. The quantity $\tilde{\Upsilon}$ is shown in [2] to be roughly estimated by $(\tilde{\sigma}_B^2 - \tilde{\sigma}_A^2)/2$. This value is found to be small and may be approximated as zero.

5.3 Interface temperature

Having obtained an equation for the interface temperature, we proceed further by rearranging the equation to extract an exact expression for T . This is given below as,

$$T = T_0 - \frac{\left(\tilde{\mathcal{K}} + \frac{\tilde{V}_n}{\tilde{m}}\right) \tilde{\sigma}_\chi RT/v_m}{\chi L_B/T_M^B + (1 - \chi)L_A/T_M^A}, \quad (5.53)$$

where,

$$T_0 = \frac{(\chi L_B + (1 - \chi)L_A)}{(\chi L_B/T_M^B + (1 - \chi)L_A/T_M^A)},$$

and Υ is assumed to be zero. Note that, in the dilute solution limit, i.e., the limit $\chi \rightarrow 0$, $\tilde{\sigma}_\chi \approx \tilde{\sigma}_A$, and T_0 is given by the following expansion,

$$T_0 = T_M^A + \chi \left[\frac{T_M^A}{L_A} (L_B - L_A) - \frac{T_M^{A^2}}{L_A} \left(\frac{L_B}{T_M^B} - \frac{L_A}{T_M^A} \right) \right] + \mathcal{O}(\chi^2). \quad (5.54)$$

Hence, the **dimensional form** of the leading order in χ of (5.53) is given by,

$$T \approx T_M^A - \frac{T_M^A \sigma_A \mathcal{K}}{L_A} - \frac{V_n}{\tilde{m}D} \frac{T_M^A \sigma_A}{L_A}. \quad (5.55)$$

For a dilute alloy, a common form for the interface temperature is given by the equation below (a simplified version of equation (2.9) in chapter 2),

$$T = T_M^A + m_L(V_n)c_L - T_M^A \Gamma \mathcal{K} - \frac{V_n}{\mu_A}, \quad (5.56)$$

where the first two terms of the (5.56) is obtained from the phase diagram; the second and third terms are the undercooling terms due to the Gibbs-Thomson effect and the interface kinetic effect respectively, where $\Gamma = \sigma_A/L_A$ represents the capillary length, and μ_A denotes the dimensional attachment kinetic parameter.

After comparing equation (5.55) and (5.56), we identify the term proportional to $\tilde{\mathcal{K}}$ in (5.55) as the undercooling term due to the Gibbs-Thomson effect, and the term proportional to \tilde{V}_n as the kinetic undercooling term. Also, the second term in (5.56) is approximated by the first order term in (5.54), i.e., the term proportional to the interface concentration, χ .

The undercooling terms from the (5.55) and (5.56) imply that,

$$\tilde{m} = \frac{\epsilon^2 M_1}{D} \quad (5.57)$$

$$= \frac{\mu_A \sigma_A T_M^A}{L_A D}. \quad (5.58)$$

Thus we see that equation (5.58) relates the non-dimensional phase-field parameter \tilde{m} directly to the material parameters of A, where here we have shown that \tilde{m} is exactly equal to the non-dimensional attachment kinetic parameter. For the Nickel-Copper alloy, this value turns out to be approximately 500.

Chapter 6

Phase diagram for a regular solution model

A phase diagram (sometimes known as an equilibrium diagram) is one way of relating the temperature at the solid-liquid interface and the interfacial concentration of solute, while capturing the notion of equilibrium in alloy solidification. It may be thought of as an analogue to the notion of melting point for the case of a pure material. The phase diagram indicates the equilibrium compositions, at a given temperature, of the two phases separated by a stationary interface. The loci of the solid and the liquid compositions as functions of temperature are called the solidus and liquidus curves respectively. These two curves act as boundaries separating a region where a single phase exists from the region where two phases co-exist. The simplest phase diagram of a binary alloy is one that characterizes the solidification of ideal liquid to ideal solid solutions. Such a phase diagram consists of a liquidus and a solidus curve, joined together at the points corresponding to the melting points of the pure components to make up the shape of a convex lens (see Fig. 2.2).

In this section we investigate how phase diagrams may change as each phase of the alloy deviates from being ideal, by introducing regular solution terms in the free energy functions. They are constructed from the common tangent conditions obtained from the conditions at equilibrium.

6.1 The free energy

The corresponding free energy density for a regular solution model may be given by the following equation,

$$f(\phi, c) = cf_B(\phi) + (1 - c)f_A(\phi) + \frac{RT}{v_m}[c \ln c + (1 - c) \ln(1 - c)] + G(\phi)c(1 - c), \quad (6.1)$$

where $G(\phi)$ is the energy of pairwise interactions of the atoms in the solution and is given by $G(\phi) = G_L + \phi(G_S - G_L)$ as suggested by Wheeler et. al. [1]. It has the value G_S in the solid (when $\phi = 1$) and G_L in the liquid (when $\phi = 0$). The quantities R , T and v_m are respectively the universal gas constant, the temperature of the system and the molar volume (assumed constant).

The contribution of the entropy of mixing of a regular solution model to the Helmholtz free energy density is given by the terms proportional to RT/v_m and the term proportional to $G(\phi)$ (the free energy density for the ideal solution may be recovered by setting $G(\phi) \equiv 0$). For simplicity, we set G_L to zero, to give a phase transformation from an ideal liquid solution to a regular solid solution. The functions $f_A(\phi)$ and $f_B(\phi)$ assume the form given in (3.2) and given below as,

$$f_A(\phi) = \frac{W_A}{4}\phi^2(\phi - 1)^2 + \frac{W_A\beta_A(T)}{6}\phi^2(3 - 2\phi), \quad (6.2)$$

$$f_B(\phi) = \frac{W_B}{4}\phi^2(\phi - 1)^2 + \frac{W_B\beta_B(T)}{6}\phi^2(3 - 2\phi). \quad (6.3)$$

To analyse the effect of the regular solution term on the free energies, we plot the free energy curves against composition for a fixed G_S and vary the temperature. For the purpose of illustration we have included the plots of the free energy curves for $G_S = 2000 Jcm^{-3}$ where significant effects are observed (see Fig. 6.1).

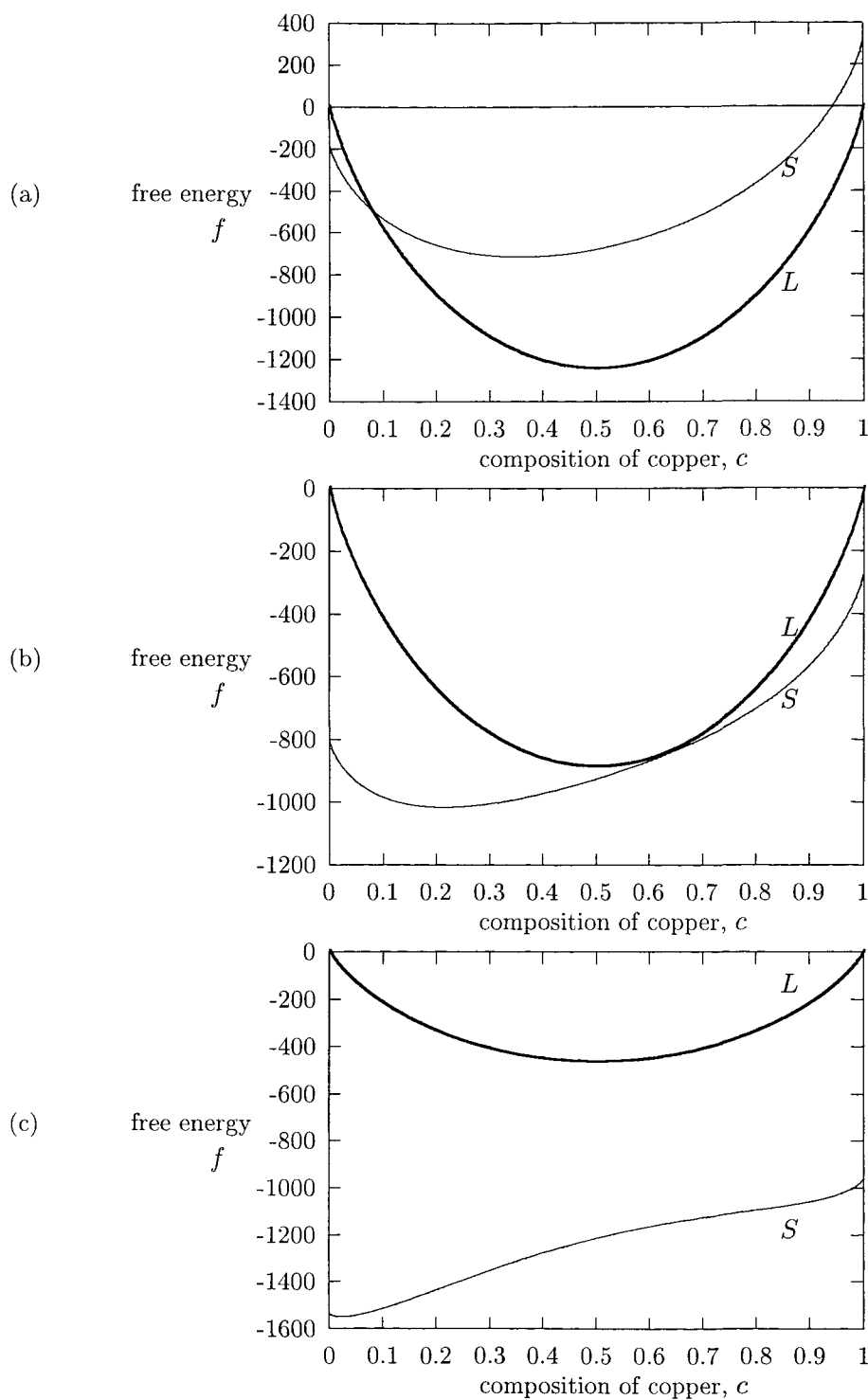


Figure 6.1: Free energy curves for solid and liquid of Nickel-Copper alloy, displayed as functions of composition of Copper at temperatures (a) 1600K, (b) 1140K, and (c) 600K (miscibility gap), with $G_S = 2000\text{Jcm}^{-3}$ and $G_L = 0$.

From studying the behaviour of the free energy curves for the solid and liquid of our model, we notice that for a fixed G_S , while the shape of the liquid curve remains convex, the solid curve becomes concave at a sufficiently low temperature. We define the critical temperature T_{crit} as the temperature at which the curvature of the solid free energy curve is zero, i.e., its second and third derivatives are identically zero (Lupis [66]). This condition allows us to find the following explicit expressions for T_{crit} and the corresponding concentration c_{crit} ;

$$T_{crit} = \frac{G_S v_m}{2R} \quad (6.4)$$

and

$$c_{crit} = 0.5. \quad (6.5)$$

Below the critical temperature, the solid free energy curve becomes a double-well with respect to c and a *miscibility gap* is said to occur.

Positive values of G_S suggest positive deviations from ideality of the solid phase. In other words, like atoms in the solution have a greater affinity for each other. Sufficiently large values of G_S cause instability in the system when the temperature decreases below the critical temperature. The region with a miscibility gap that starts to form at this point is a region where the solid solution segregates into two phases, one rich in A and the other rich in B giving two solid crystals of two different concentrations, which can exist in a state of equilibrium.

6.2 Common tangent constructions

6.2.1 Classical thermodynamics

Equilibrium in a heterogeneous system (i.e., a system containing more than one phase) is related to the chemical potential of the components, such that at this state, the chemical potentials of all the components in the system are equal in all phases (Lupis [66]). So for a solid-liquid system of a binary alloy with components A and B , we require $\mu_A^L = \mu_A^S$ and $\mu_B^L = \mu_B^S$, where μ_A^L and μ_A^S are the chemical potentials of A in the liquid and solid respectively. Similarly for μ_B^L and μ_B^S .

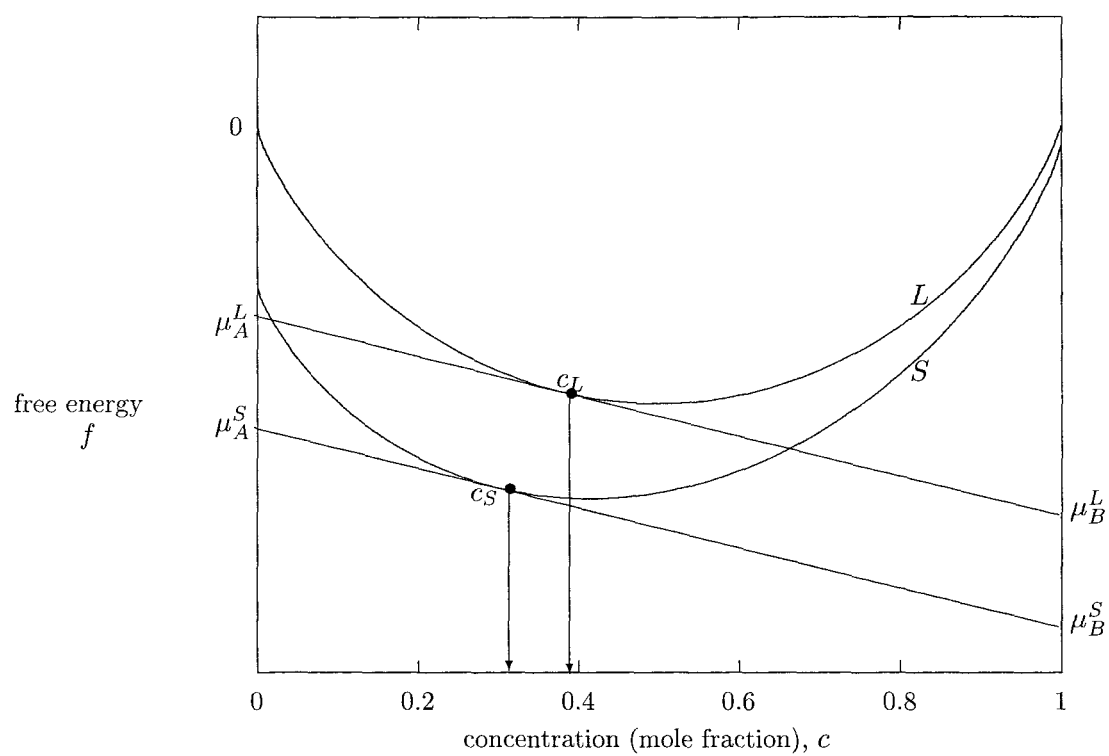


Figure 6.2: Tangents to the energy curves at $c = c_S$ and $c = c_L$, when the system is not at equilibrium. The curves labelled L and S are the free energy curves of the liquid and solid phases respectively.

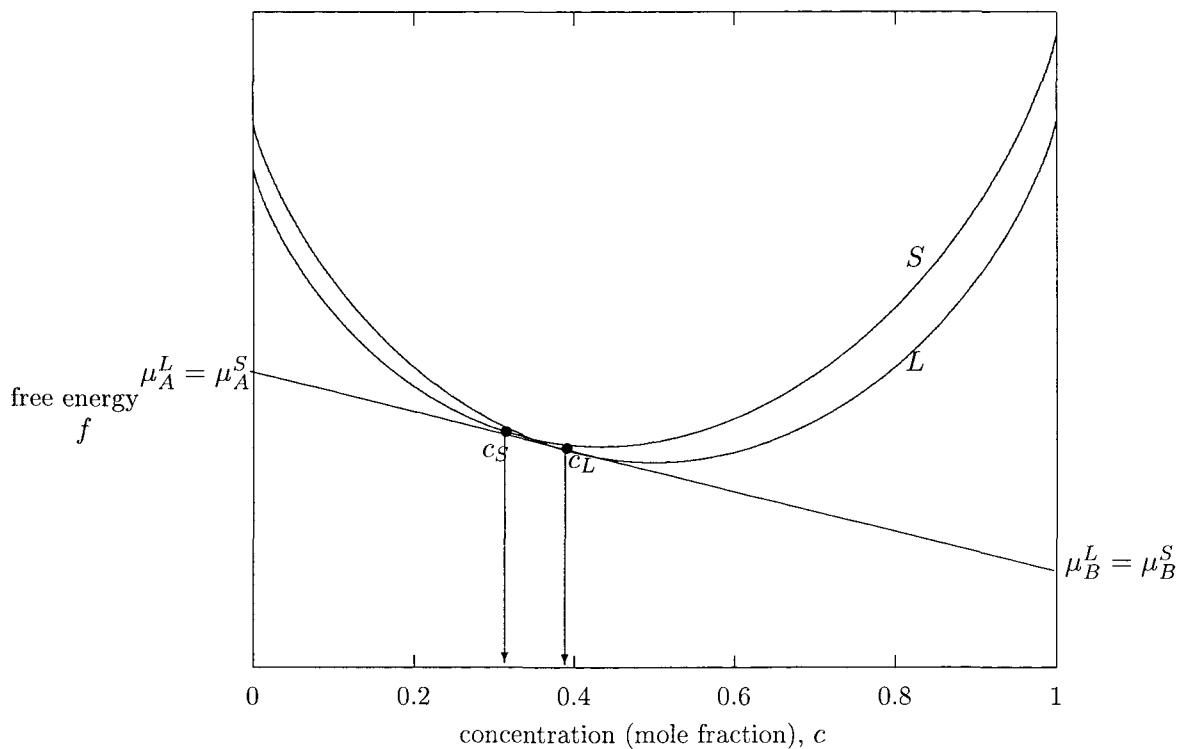


Figure 6.3: A common tangent when the system is in equilibrium. The curves labelled L and S are the free energy curves of the liquid and solid phases respectively.

The chemical potential of a component may be obtained through *the method of intercept*. For example, for a given concentration, the intercept of the corresponding tangent to the liquid free energy curve with the f -axis at $c = 0$, gives μ_A^L , the intercept with the f -axis at $c = 1$ gives μ_B^L . Similarly, the intercepts of the tangent to the solid free energy tangent give μ_A^S and μ_B^S (see Fig. 6.2).

At equilibrium, because $\mu_A^L = \mu_A^S$ and $\mu_B^L = \mu_B^S$, the two tangents are coincident (see Fig. 6.3), forming a common tangent between the two points, $(c_S, f(1, c_S))$ and $(c_L, f(0, c_L))$ on the free energy curves, with corresponding concentrations c_S and c_L which represent the equilibrium concentrations in the solid and liquid respectively. Denoting the slope of the common tangent by Λ we have that,

$$\Lambda = \frac{f(0, c_L) - \mu_A^L}{c_L} = \frac{f(1, c_S) - \mu_A^S}{c_S}. \quad (6.6)$$

Also,

$$\Lambda = f_c(0, c_L) = f_c(1, c_S). \quad (6.7)$$

Writing $F(\phi, c) = f(\phi, c) - \Lambda c$, we arrive at the following common tangent conditions,

$$F(1, c_S) = F(0, c_L), \quad (6.8)$$

$$F_c(1, c_S) = F_c(0, c_L) = 0. \quad (6.9)$$

6.2.2 Phase-field model

Employing the phase-field model WBM2, we may construct the phase diagram by using the fact that the solid and liquid phases are separated by a stationary planar interface. The corresponding steady, one-dimensional solutions of the governing equations, in this case are

$$-\epsilon^2 \phi_{zz} + f_\phi = 0, \quad (6.10)$$

for the phase-field; where z measures distance normal to the interface. After integrating the solute equation (3.22) twice and employing the far-field conditions (3.24), we have

$$-\delta^2 c_{zz} + f_c = \Lambda, \quad (6.11)$$

where Λ is a constant of integration. We rewrite equations (6.10) and (6.11) in the form

$$\epsilon^2 \phi_{zz} + F_\phi = 0, \quad (6.12)$$

$$\delta^2 c_{zz} + F_c = 0, \quad (6.13)$$

where F is the function defined in the last section. We require that the solution matches to the solid and liquid bulk phases and therefore impose the boundary conditions

$$(\phi, c) \rightarrow (1, c_S) \text{ as } z \rightarrow -\infty, \quad (6.14)$$

$$(\phi, c) \rightarrow (0, c_L) \text{ as } z \rightarrow +\infty. \quad (6.15)$$

This is equivalent to requiring a heteroclinic connection between $(1, c_S)$ and $(0, c_L)$ of the ordinary differential equations (6.12) and (6.13). We therefore insist that $(1, c_S)$ and $(0, c_L)$ are critical points, i.e., $F_c(1, c_S) = F_c(0, c_L) = 0$ which simply recovers the common tangent condition in (6.9), derived from the classical results. Note the form of f automatically ensures $F_\phi(1, c_S) = F_\phi(0, c_L) = 0$. A first integral of (6.12) and (6.13) gives

$$\frac{\epsilon^2}{2}(\phi_z)^2 + \frac{\delta^2}{2}(c_z)^2 + F = \text{constant}, \quad (6.16)$$

on the heteroclinic orbit connecting $(1, c_S)$ and $(0, c_L)$. Thus, because ϕ_z and $c_z \rightarrow 0$ as $z \rightarrow \pm\infty$, we have $F(1, c_S) = F(0, c_L)$, the other condition (6.8) for the common tangent construction.

Note that for an ideal solution, (6.8) and (6.9) can be solved exactly, to give expressions for the solidus and liquidus concentration, c_S and c_L , in terms of the interfacial temperature T . They are,

$$c_S = \frac{(\exp(\widetilde{\Delta F_A}) - 1)}{(\exp(\widetilde{\Delta F_A}) - \exp(\widetilde{\Delta F_B}))}, \quad (6.17)$$

$$c_L = c_S \exp(\widetilde{\Delta F_B}), \quad (6.18)$$

which implies,

$$k_e = \frac{c_S}{c_L} = \frac{1}{\exp(\widetilde{\Delta F_B})} \quad (6.19)$$

Using a similar common tangent construction, the equilibrium between solid a and solid b , due to the formation of the miscibility gap in the free energy curve, leads to the following conditions,

$$F(1, c_a) = F(1, c_b) \quad (6.20)$$

$$F_c(1, c_a) = F_c(1, c_b) = 0 \quad (6.21)$$

where c_a and c_b are the concentrations of solid a and solid b respectively, at equilibrium.

6.3 Numerical results

We solved numerically the common tangent equations (6.8) and (6.9) for T , c_S and c_L , and equations (6.20) and (6.21) for T , c_a and c_b . Plots of T versus c_S and T versus c_L give the solidus and liquidus curves for the solid-liquid phase transition while plots of T versus c_a and T versus c_b give the curves for the solid-solid phase transition. The two types of curves are plotted on the same axis for three increasing values of G_S .

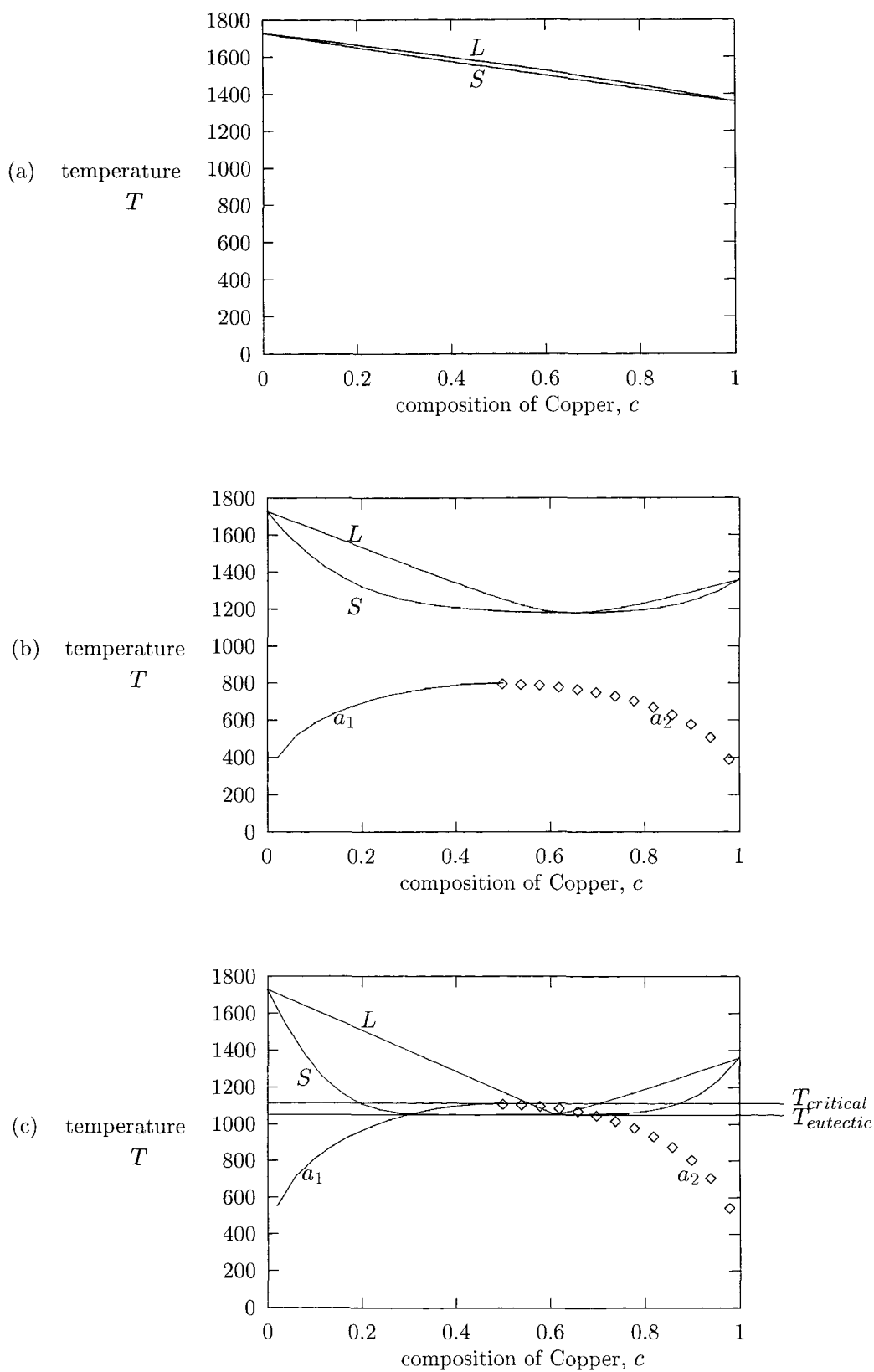


Figure 6.4: Solidus-liquidus and solidus-solidus phase diagrams for Nickel-Copper alloy, drawn for $G_S =$ (a) 0, (b) 1800 and (c) 2500 J cm⁻³, G_L is assumed to be zero. The bottom most diagram displays the eutectic point.

From the plots, we see that when $G_S = 0$, a lens-shaped diagram is obtained for the solid-liquid phase transition. For nonzero values of G_S , the liquidus exhibits a minima which touches the solidus curve. For small values of G_S , this occurs at a concentration close to $c = 1$. As G_S increases this concentration moves away from $c = 1$. The temperature corresponding to this minima is known as the *congruent melting point*, a point where the free energy curves of solid and liquid are tangent to each other (see Fig. 6.1, for $T = 1140K$). At this temperature, the liquid of the alloy solidifies without any change in its composition.

The critical temperature, T_{crit} , defined in (6.4) to be proportional to G_S , is the temperature corresponding to the maximum point observed in the solid-solid phase diagram. Therefore, as G_S increases this maximum starts to move upwards, to higher values of T . When T_{crit} becomes greater than the congruent melting point, a *eutectic point* is formed (Fig. 6.4(c)). At this point, the common tangent to the free energies of solid and liquid is also a common tangent to the two convex parts of the free energy curve of the solid. The congruent melting point is now referred to as the eutectic temperature.

Chapter 7

Numerical Computations of the Phase-field Model

As we have seen in section 3.5, solute trapping behaviour is observed in the WBM2 theory as the interface velocity is increased, when the analysis is confined to a particular distinguished limit. This is the limit $\epsilon/\delta \rightarrow 0$ (with δ fixed), where ϵ and δ are the phase field and solute field **gradient energy coefficient** respectively. A natural question arises as to whether this limit is *required* to observe solute trapping and, moreover, whether it is necessary to have a solute gradient energy (i.e., $\delta \neq 0$), incorporated into the free energy functional for the model. The numerical analysis carried out in this chapter is aimed at providing an answer to these questions. For this purpose, the governing equations are nondimensionalised with respect to the length scale, l_ϵ , representing the distance over which ϕ changes, where $l_\epsilon = \epsilon \sqrt{\frac{v_m}{RT}}$. A quantity $\Delta = \delta/\epsilon$ is introduced, which is a positive constant and may be set to zero, consequently excluding the solute gradient energy term from the model.

A numerical code has been written to solve the dimensionless forms of equations (3.4) and (3.22). Following WBM2, the equations are formulated for a planar solid-liquid interface moving with a constant speed V . In the frame of reference of the moving interface, the equations in 1-D are given by,

$$\epsilon^2 \frac{d^2 \phi}{dz^2} + \frac{V}{M_1} \frac{d\phi}{dz} - f_\phi = 0, \quad (7.1)$$

and

$$\frac{d}{dz} \left(M_2 c(1-c) \frac{d}{dz} \left[-\delta^2 \frac{d^2 c}{dz^2} + f_c \right] \right) + V \frac{dc}{dz} = 0, \quad (7.2)$$

where we have assumed steady states in this frame of reference.

Two cases are considered in the numerical calculations:

(1) when the diffusivity in the solid, D_S , equals the diffusivity in the liquid, D_L ;

(2) when D_S is not equal to D_L .

In the latter case, D_S is distinguished from D_L by letting D (which is related to M_2 through equation (3.23)) to be a function of ϕ satisfying the conditions $D = D_S$, $dD/d\phi = 0$ when $\phi = 1$ and $D = D_L$, $dD/d\phi = 0$ when $\phi = 0$. The following choice of $D(\phi)$ satisfies all the conditions and is monotonic in ϕ ,

$$D(\phi) = (D_S - D_L)\phi^2(3 - 2\phi) + D_L. \quad (7.3)$$

7.1 Dimensionless equations

Under the assumption of constant diffusivity throughout the region $(-\infty, +\infty)$, i.e., M_2 is constant, we nondimensionalise equations (7.1) and (7.2) using $l_\epsilon = \epsilon\sqrt{v_m/RT}$ as the reference length and we set $\delta = \epsilon\Delta$ where Δ is a positive constant. Specifically, we introduce the dimensionless variables $\tilde{z} = z/l_\epsilon$ into the governing equations. The dimensionless equations are therefore

$$\frac{d^2\phi}{d\tilde{z}^2} + \frac{\tilde{V}_\epsilon}{\tilde{m}} \frac{d\phi}{d\tilde{z}} - (\tilde{f}_\phi^{(-2)} + \tilde{f}_\phi^{(0)}) = 0, \quad (7.4)$$

and

$$\frac{d}{d\tilde{z}} \left(c(1 - c) \frac{d}{d\tilde{z}} \left[-\Delta^2 \frac{d^2c}{d\tilde{z}^2} + (\tilde{f}_c^{(-2)} + \tilde{f}_c^{(0)}) \right] \right) + \frac{d^2c}{d\tilde{z}^2} + \tilde{V}_\epsilon \frac{dc}{d\tilde{z}} = 0, \quad (7.5)$$

or equivalently,

$$c(1 - c) \frac{d}{d\tilde{z}} \left[-\Delta^2 \frac{d^2c}{d\tilde{z}^2} + (\tilde{f}_c^{(-2)} + \tilde{f}_c^{(0)}) \right] + \frac{dc}{d\tilde{z}} + \tilde{V}_\epsilon c = \tilde{V}_\epsilon c_\infty. \quad (7.6)$$

Equation (7.6) is obtained after integrating (7.5) once and applying the following boundary conditions,

$$(\phi, c) \rightarrow \begin{cases} (1, c_\infty), & \text{as } z \rightarrow -\infty, \\ (0, c_\infty), & \text{as } z \rightarrow +\infty, \end{cases} \quad (7.7)$$

where the far-field concentrations $c_{-\infty}$ and $c_{+\infty}$ are assumed equal. The dimensionless interfacial velocity is now defined by

$$\tilde{V}_\epsilon = \frac{Vl_\epsilon}{D}, \quad (7.8)$$

and the interfacial mobility \tilde{m} has the same definition as in (3.29). The nondimensional representation of the free energy density (3.30) is used here, where the contribution from the pure component A is given by,

$$\tilde{f}_A(\phi) = \tilde{f}_A^{(-2)}(\phi) + \tilde{f}_A^{(0)}(\phi), \quad (7.9)$$

with a similar expression for B . The notations $\tilde{f}_A^{(-2)}$ and $\tilde{f}_A^{(0)}$ are the same as those used in (3.32).

The equations above may be generalised to the case where the diffusivity varies across the region, by simply replacing D with $D(\phi)$ from (7.3). This gives

$$\frac{d^2\phi}{d\tilde{z}^2} + \frac{\tilde{V}}{\tilde{m}} \frac{d\phi}{d\tilde{z}} - (\tilde{f}_\phi^{(-2)} + \tilde{f}_\phi^{(0)}) = 0, \quad (7.10)$$

and

$$\begin{aligned} \frac{d}{d\tilde{z}} \left\{ c(1-c) \left[\left(\frac{D_S}{D_L} - 1 \right) \phi^2(3-2\phi) + 1 \right] \frac{d}{d\tilde{z}} \left[-\Delta^2 \frac{d^2c}{d\tilde{z}^2} + (\tilde{f}_c^{(-2)} + \tilde{f}_c^{(0)}) \right] \right\} \\ + \frac{d}{d\tilde{z}} \left\{ \left[\left(\frac{D_S}{D_L} - 1 \right) \phi^2(3-2\phi) + 1 \right] \frac{dc}{d\tilde{z}} \right\} + \tilde{V}_\epsilon \frac{dc}{d\tilde{z}} = 0, \end{aligned} \quad (7.11)$$

where now

$$\tilde{V}_\epsilon = \frac{Vl_\epsilon}{D_L}, \quad \tilde{m} = \frac{M_1\epsilon^2}{D_L}.$$

Note that equations (7.10) and (7.11) reduce to (7.4) and (7.6) when we set $D_S/D_L = 1$.

7.2 Numerical procedures

The governing equations (7.4) and (7.6), together with boundary conditions given in (7.7) make up a nonlinear boundary value problem with variables varying on an infinite domain. In the sharp-interface limit, the solute field forms a boundary layer adjacent to the interface, and its length scale is characterized by the ratio of the diffusivity to the interface velocity, i.e., D/V [1]. This length scale is much larger than the characteristic length scale of the phase-field, which is l_ϵ . In order to solve for the solute and phase field equations numerically, the region is truncated to some finite domain of length, L_N (where N is the number of points), chosen to be ‘large’ enough so that the boundary condition in the solid bulk phase is applied at $\tilde{z} = -L_N/2$, and the condition in the liquid bulk phase is applicable at $\tilde{z} = L_N/2$. Because the variation in the phase-field, ϕ , occurs on the length scale, l_ϵ , in the vicinity of the interface, and the solute c varies on a much larger length scale, which decreases monotonically as the interface velocity increases [2], problems may arise when solving the governing equations. This is due to the fact that the difference in the length scale is accentuated when the interface velocity is small. Thus in order to ensure the far-field boundary conditions for c are met, a much larger domain is needed. This often causes problem in obtaining ‘well-resolved’ solutions for **both** ϕ and c .

We tackle this problem by allowing the uniform interval between each of the evaluation points to vary with L_N . This has the effect of letting the length scale in the numerical code to change with velocity. We set L_N and the scaled interface velocity \tilde{V}_ϵ , to be input parameters so that everytime \tilde{V}_ϵ changes, L_N can also be changed. Consequently, for a specific value of \tilde{V}_ϵ , L_N can be altered until the boundary conditions are satisfied and the program converges satisfactorily. Because the interval between each evaluation points is defined as, $l = L_N/N$, increasing L_N alone will make the solution ‘less well-resolved’ (i.e., l is large). Therefore, in order to increase the resolution, N can be increased.

Other input parameters include the latent heats of the pure components of the alloy, L_A and L_B , their melting temperatures, T_M^A and T_M^B , the equilibrium segregation coefficient k_e , the far-field concentration c_∞ , the diffusivity ratio D_S/D_L , ϵ and Δ . The boundary value problem is solved using a second order *Finite Difference Method*. Instead of imposing the *Dirichlet* boundary conditions in (7.7), *Neumann* boundary conditions are employed at $\tilde{z} = -L_N/2$ and $\tilde{z} = L_N/2$, for both ϕ and c . An additional equation is added to the system of equations, to solve for the extra variable in the problem, namely, the interfacial temperature T . This extra equation is an integral condition (applied numerically using *Simpson’s Rule*) given below,

$$\int_{\tilde{z}=L_N/2}^{\tilde{z}=-L_N/2} \left[\phi(\tilde{z}) - \frac{1}{2} \right] d\tilde{z} = 0. \quad (7.12)$$

The finite difference discretization of the governing equations is given in appendix C. The discretized equations and the integral equation make up a system of nonlinear algebraic equations for the nodal values of ϕ , c and the value of T . This system of equations is solved using subroutine SNSQE, which contains an algorithm for solving N nonlinear equations in N variables by a modification of the *Powell Hybrid Method* [67].

After a successful convergence, the program calculates the maximum value of solute concentration and computes a value for the partition coefficient k , which we define as $k = c_\infty/c_{\max}$, where c_{\max} is the maximum value of the solute concentration.

Most of the calculations we performed are based on the Nickel-Copper alloy data given in appendix B. The phase diagram of the Nickel-Copper alloy has been experimentally determined to have the lens shape, and hence the phase transition may be assumed to occur from an ideal liquid mixture to an ideal solid mixture. Unfortunately, the near-equilibrium solidification of most alloys cannot be represented by the lens-shaped phase diagram. As we have shown in chapter 5, the shape of the phase diagram depends on the type of mixtures (e.g., ideal, regular, subregular, etc.) which exist in the two distinct phases of the solidifying material. The current model can be extended to non-ideal alloys by adding the term corre-

sponding to the contribution of the entropy of mixing of components A and B (the case of a regular solution mixture has been demonstrated in chapter 3), to the free energy density function.

7.2.1 Initial guesses

The subroutine SNSQE employed in the numerical algorithm contains a procedure for solving nonlinear functions which uses the *Newton's Method*. This method requires a good initial guess in order for the code to converge satisfactorily and produce the required solutions. The nature of the solidification process itself, which departs from the near equilibrium state as the solidification velocity is increased, produces solutions that have very different behaviour for different values of \tilde{V}_ϵ . Therefore, in order to achieve successful convergence of the numerical code, different initial guesses are needed at low \tilde{V}_ϵ and high \tilde{V}_ϵ . Thus we have used two different forms of initial guesses corresponding to the two different cases below:

1. At low \tilde{V}_ϵ , the ϕ and c lie close to the solutions correspond to a stationary interface, and these are given by [2],

$$\phi = \frac{1}{2}[1 - \tanh(3\tilde{\sigma}^*z)], \quad (7.13)$$

$$c = \frac{1}{(1 + \exp(-\tilde{f}_c^L))}, \quad (7.14)$$

$$T = 1700, \quad (7.15)$$

where,

$$\begin{aligned} \tilde{f}_c^L &= \tilde{f}_c(\phi = 0, c = c_L) \\ &= 18(\tilde{\sigma}_B^2 - \tilde{\sigma}_A^2)\phi^2(1 - \phi)^2 + (\widetilde{\Delta F}_B - \widetilde{\Delta F}_A)\phi^2(3 - 2\phi) + \ln(c_L/(1 - c_L)), \\ \sigma^* &= \sqrt{c_\infty\sigma_B^2 + (1 - c_\infty)\sigma_A^2}, \\ \tilde{\sigma}^* &= \sigma^*/(\epsilon\sqrt{RT/v_m}), \\ \tilde{\sigma}_A &= \sigma_A/(\epsilon\sqrt{RT/v_m}), \\ \widetilde{\Delta F}_A &= \frac{L_A}{RT/v_m} \left(\frac{T - T_M^A}{T_M^A} \right), \end{aligned}$$

with $c_\infty (= c_S)$ and c_L correspond to the solidus and liquidus concentrations of the alloy (obtained from the phase diagram), and T is the corresponding temperature.

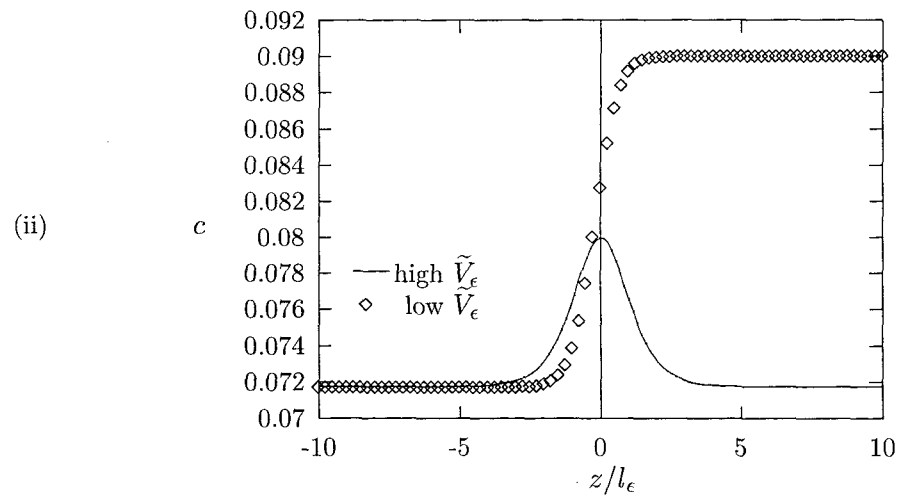
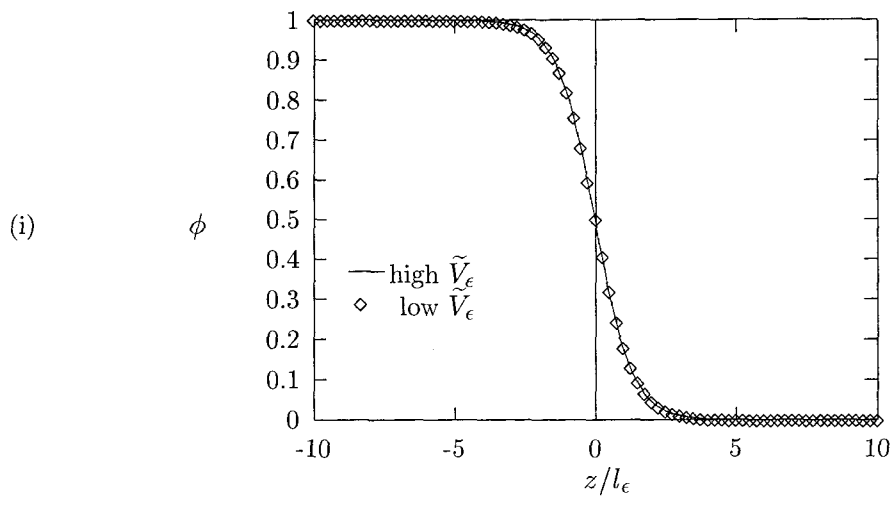


Figure 7.1: (i) initial guess for ϕ , (ii) initial guess for c .

2. At high \tilde{V}_ϵ , the solutions can be approximated as asymptotic expansions in \tilde{V}_ϵ^{-1} (described in chapter 8), i.e.,

$$\phi = \frac{1}{2}[1 - \tanh(3\tilde{\sigma}_0^* \tilde{z})], \quad (7.16)$$

$$c = c_\infty + \tilde{V}_\epsilon^{-1} c^{(1)}, \quad (7.17)$$

$$T = T_0 \quad (7.18)$$

where,

$$\begin{aligned} c^{(1)} &= - \left[\left(\frac{D_S}{D_L} - 1 \right) \phi^2 (3 - 2\phi) + 1 \right] c_\infty (1 - c_\infty) \frac{d\phi}{d\tilde{z}} \left(\tilde{f}_{c\phi}^{(-2)}(\phi, c_\infty) + \tilde{f}_{c\phi}^{(0)}(\phi, c_\infty) \right), \\ \tilde{f}_{c\phi}^{(-2)} &= 36(\tilde{\sigma}_B^2 - \tilde{\sigma}_A^2) \phi (1 - \phi) (1 - 2\phi), \\ \tilde{f}_{c\phi}^{(0)} &= 6(\widetilde{\Delta F}_B - \widetilde{\Delta F}_A) \phi (1 - \phi), \\ T_0 &= \frac{c_\infty L_B + (1 - c_\infty) L_A}{c_\infty L_B / T_M^{(B)} + (1 - c_\infty) L_A / T_M^{(A)}}, \\ \tilde{\sigma}_0^* &= \sigma^* / \left(\epsilon \sqrt{RT_0 / v_m} \right). \end{aligned}$$

Both the initial profiles for solutions at low and high \tilde{V}_ϵ are shown in Fig. 7.1.

Notice that at low velocities, the initial guesses depend on the values of the solidus and liquidus concentrations (and hence k_e). Therefore, it is vital that the equilibrium phase diagram of the alloy is known in order to obtain reasonably accurate solutions at low interface velocities.

7.2.2 Grid resolution

We have described earlier how the size of the domain of computation can affect the convergence of the numerical code and the quality of the computed solutions. As a demonstration, we computed the solutions for three different values of the domain size, L_N , with all other parameters fixed (see Fig. 7.2 and 7.3). We can see from the solute profiles in Fig. 7.2 that, although the code converges when the size of L_N is too small, the discrete points on the solution curve are observed to ‘oscillate’ about the ‘actual’ solution of the problem. This is evident from the fact that a very ‘rough’ and ‘jagged’ curve is obtained when all the points are connected by straight lines. This solution clearly does not accurately satisfy the boundary conditions at the end points (i.e., $dc/d\tilde{z} \neq 0$). As we increase the size of L_N , the solution curve becomes much smoother and its gradient approaches zero gradually near the edge of the computational domain (see Fig. 7.2(ii)). On the other hand, the phase-field profiles (see Fig. 7.3) are generally smooth, with the far-field boundary conditions adequately satisfied at the end points, for all the three values of L_N .

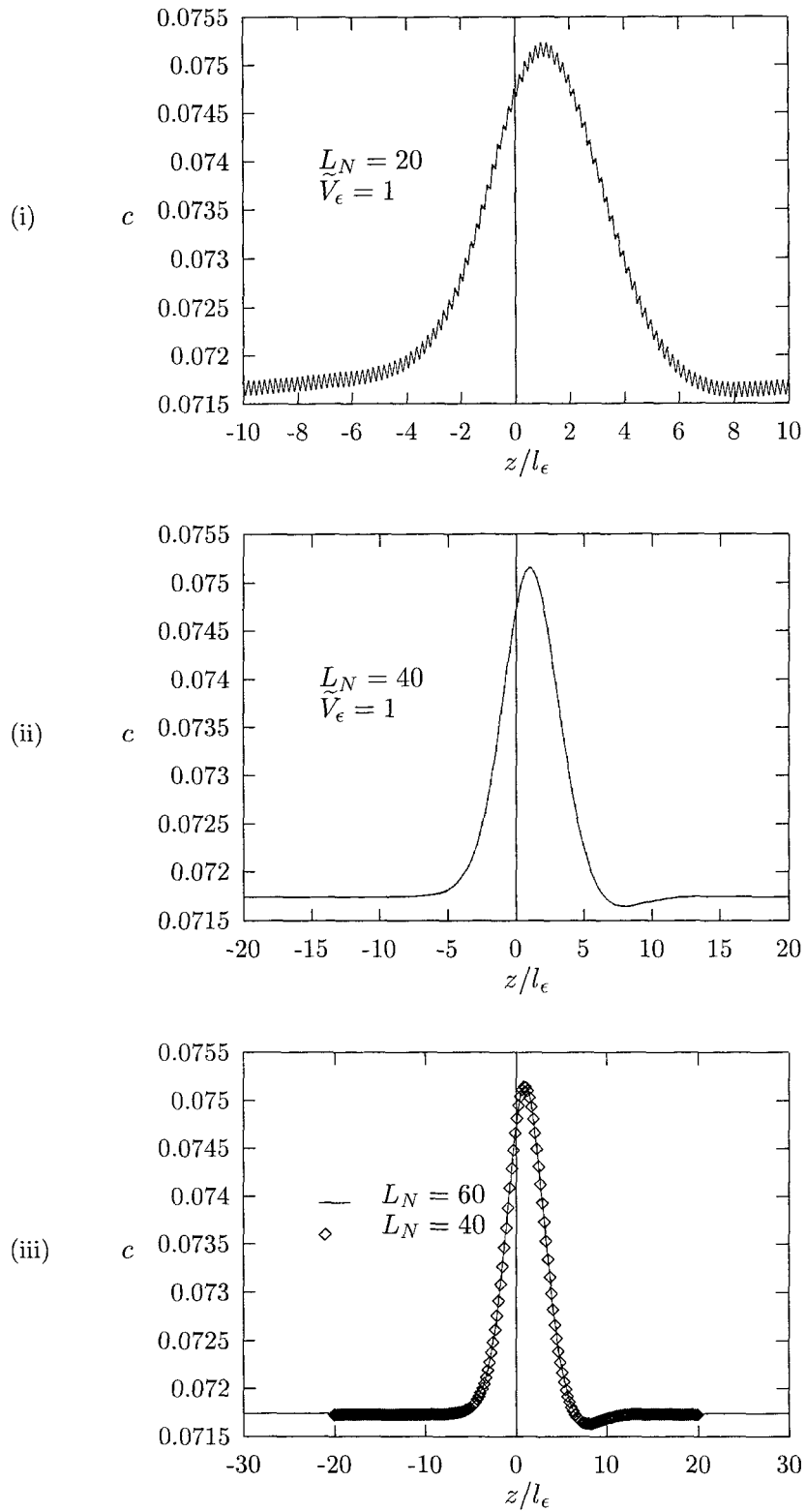


Figure 7.2: The solute profile computed for three different values of L_N , $L_N = 20$, $L_N = 40$ and $L_N = 60$. The values of \tilde{V}_ϵ , and Δ are fixed in all cases. The figure in (iii) shows that once the appropriate size of the domain length is achieved (i.e., when the far-field boundary conditions are satisfied, in this case $L_N = 40$), increasing L further will not change the solution in any way.

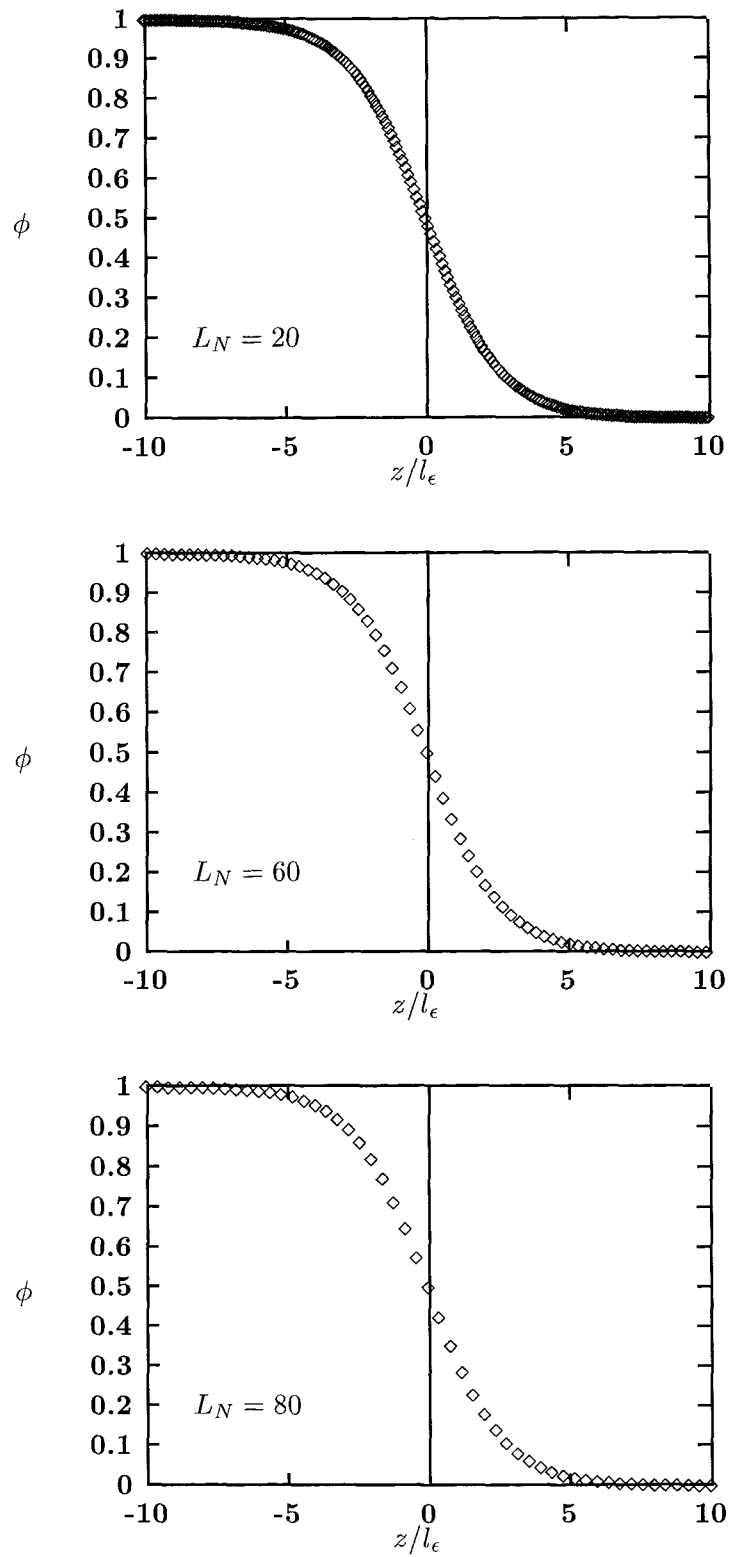


Figure 7.3: The phase-field profile produced for three different L_N . Although the profiles satisfied the neuman boundary conditions in the far-field for all three values of L_N , the number of evaluation points in the interfacial region are reduced as L_N is increased, i.e., reducing the resolution of the solution. In order to improve the resolution, N has to be increased (while keeping L_N fixed).

Once the correct boundary conditions are satisfied, the solution can be further improved by increasing the number of mesh points, N , i.e., decreasing the grid size, where the grid size l is defined as L_N/N . In order to demonstrate how the solutions improve as we increase N , we define the area under the solute curve as,

$$C = \int_0^L (c(\tilde{z}) - c_\infty) d\tilde{z}. \quad (7.19)$$

The integral (7.19) was evaluated numerically using the Simpson's Rule, where as N is increased, we can expect C to take the value given below,

$$C = C_{N_\infty} - \alpha_1/N^2 - \alpha_2/N^4, \quad (7.20)$$

where C_{N_∞} is the value of C when $N = \infty$ and α_1 and α_2 are constants. The terms of orders $1/N^2$ and $1/N^4$ are the truncation errors from the finite difference method and the Simpson's rule respectively. Assuming the term of order $1/N^4$ is small, we expect the solutions to be linear in $1/N^2$.

The value of C for various values of N are tabulated in Table 7.1, where it can be seen that the computed values of C approaches a fixed number, namely C_{N_∞} as N is increased. Assuming $C_\infty \sim C_{600}$, we calculated the value of α_1 corresponding to $N = 50, \dots, 500$ using equation (7.20) (with $\alpha_2/N^4 = 0$), and the values of C given in Table 7.1. The average of the five different values of α_1 obtained from the calculation, namely α_{av} is found to be 0.022. Equation (7.20) can now be estimated as,

$$C = C_\infty - \alpha_{av}/N^2, \quad (7.21)$$

or equivalently,

$$\ln(C_\infty - C) = -2\ln(N) + \ln(\alpha_{av}), \quad (7.22)$$

which is represented by a straight line with slope -2 that intersects the vertical axis at the point $(0, \ln(\alpha_{av}))$. This line is drawn against the corresponding numerical data in Fig 7.4, and the plot shows that all the data points lie approximately on it. This agreement validates the claim we made in (7.20) and therefore confirms the accuracy of the solutions.

Number of points, N	C
50	1.695632×10^{-2}
100	1.696344×10^{-2}
200	1.696460×10^{-2}
300	1.696511×10^{-2}
400	1.696515×10^{-2}
500	1.696532×10^{-2}
600	1.696535×10^{-2}

Table 7.1: A table of the values of C for increasing values of the number of mesh points, N .

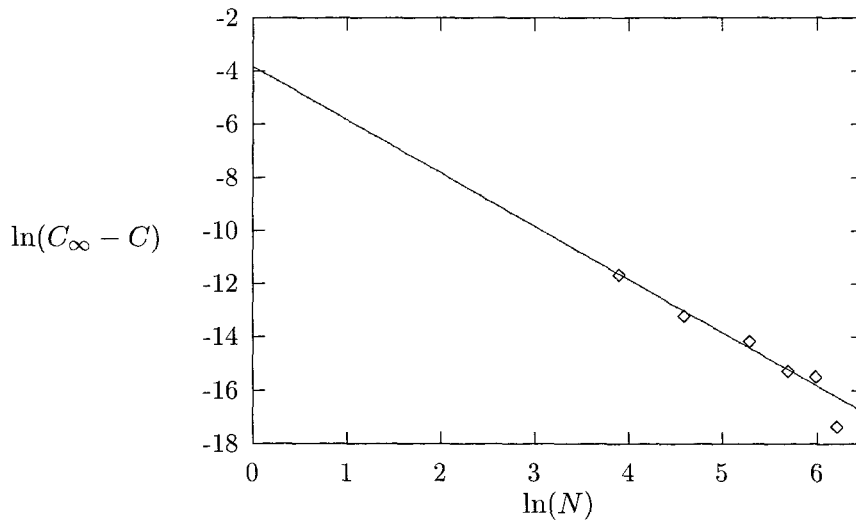


Figure 7.4: The computed values of $\ln(C_\infty - C)$ are plotted against $\ln(N)$. The data lies very closely to the straight line $\ln(C_\infty - C) = \alpha_{av}/N^2$, where $C_{N_\infty} = 1.696535 \times 10^{-2}$ and $\alpha_{av} = 0.022$.

7.3 Numerical results

The numerical calculations are carried out using the data from the Nickel-Copper alloy (see Appendix B). The value for the far-field concentration c_∞ is fixed throughout the calculation. It is estimated as the solidus concentration of the solute and this is determined using the common tangent conditions described in chapter 5. For an interface temperature of $1700K$, the solidus concentration is found to be 7.17441×10^{-2} , and it corresponds to an equilibrium partition coefficient of 0.7965. The value of $6.6 \times 10^{-6} J^{1/2} cm^{-1/2}$ is chosen for ϵ , and this is also fixed ¹. All calculations are carried out using $N = 200$.

7.3.1 Solutions when $D_S/D_L = 1$.

The solutions of the phase-field problem are first computed for a non-zero value of Δ . This is done for increasing values of the nondimensional speed \tilde{V}_ϵ , with constant diffusivity throughout the domain, (i.e., $D_S/D_L = 1$). The results are depicted in Fig. 7.5(i) and 7.5(ii). It can be clearly seen from the plots that the code has successfully produced solutions with much of the qualitative behaviour expected of rapid solidification. In Fig. 7.5(i), the maximum value of the concentration, c , decreases with increasing value of \tilde{V}_ϵ , resulting in a decrease of the degree of segregation between the solid and liquid, i.e, **solute trapping** occurs. We also observe a monotonic reduction in the characteristic length scale of the solute field as \tilde{V}_ϵ gets larger. On the other hand, the characteristic length scale of the phase-field remains almost constant for all values of \tilde{V}_ϵ (Fig. 7.5(ii)).

¹The behaviour of the solutions are similar for all values of ϵ . The size of ϵ determines the thickness of the interface (see section 7.4 later)

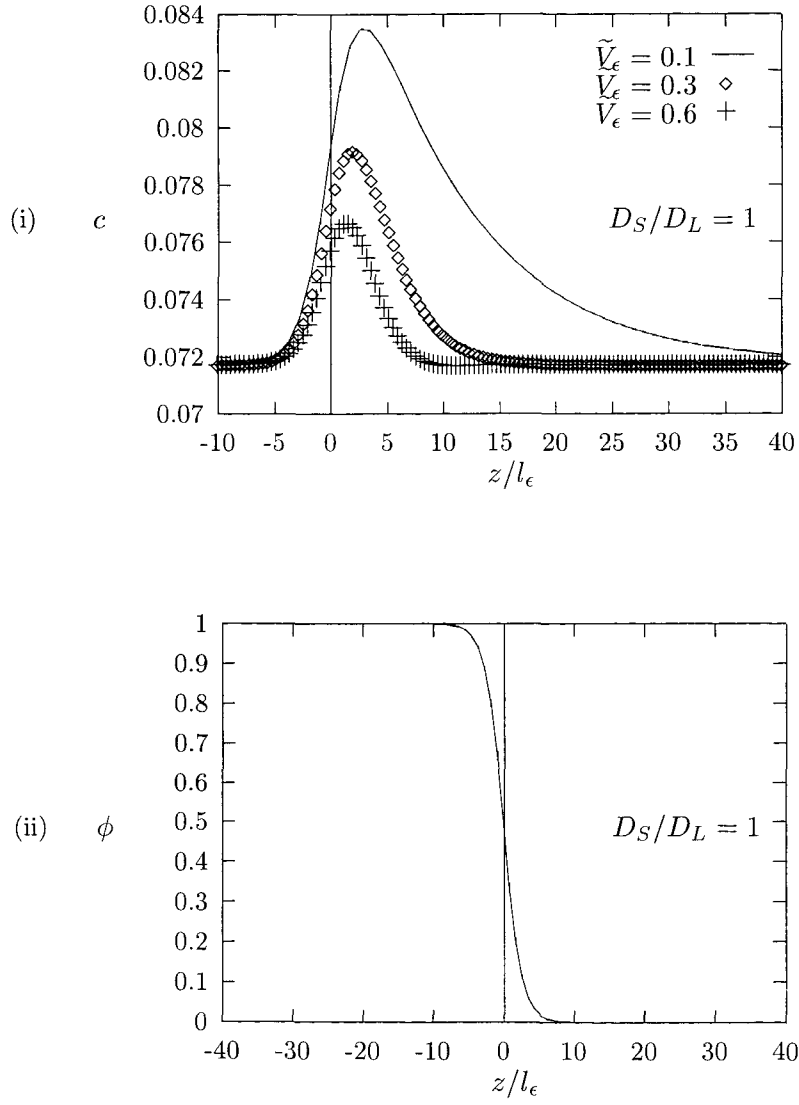


Figure 7.5: (i) The solute profile computed for different values of the dimensionless velocity \tilde{V}_ϵ , (ii) the corresponding phase-field profiles for the three different values of the dimensionless velocities are shown here to be indistinguishable. The diffusivity is assumed equal in both phases and distance has been nondimensionalised with respect to l_ϵ . The material parameters are those of Nickel-Copper alloy given in appendix B and the values of δ and ϵ are fixed at $3.3 \times 10^{-5} \text{ J}^{1/2} \text{ cm}^{-1/2}$ and $6.6 \times 10^{-6} \text{ J}^{1/2} \text{ cm}^{-1/2}$ (i.e., $\Delta = 5$) respectively.

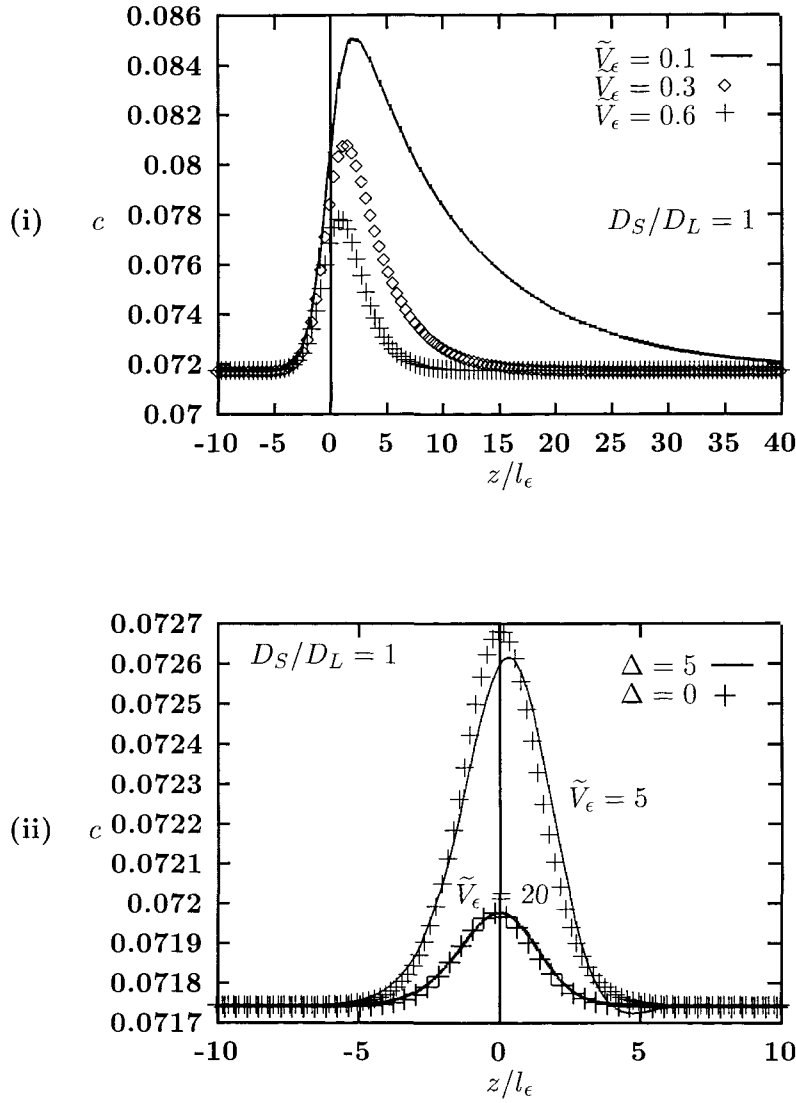


Figure 7.6: (i) The solute profile computed for different values of the dimensionless velocity \tilde{V}_ϵ , where diffusivity is equal in both phases. Distance has been nondimensionalised with respect to l_ϵ . The material parameters are those of Nickel-Copper alloy given in appendix B. The value of ϵ is $6.6 \times 10^{-6} \text{J}^{1/2} \text{cm}^{-1/2}$ and Δ is fixed at 0. (ii) The solute profiles for $\Delta = 5$ and $\Delta = 0$ are compared for increasing values of the dimensionless velocity \tilde{V}_ϵ .

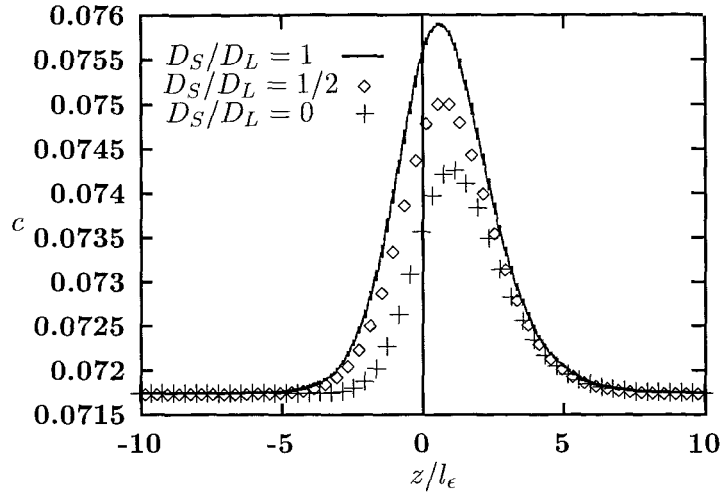


Figure 7.7: The solute profiles drawn for three different values of D_S/D_L . The solutions were computed with $\tilde{V}_\epsilon = 1$, where the value of ϵ is fixed at $6.6 \times 10^{-6} \text{ J}^{1/2} \text{ cm}^{-1/2}$ in all cases.

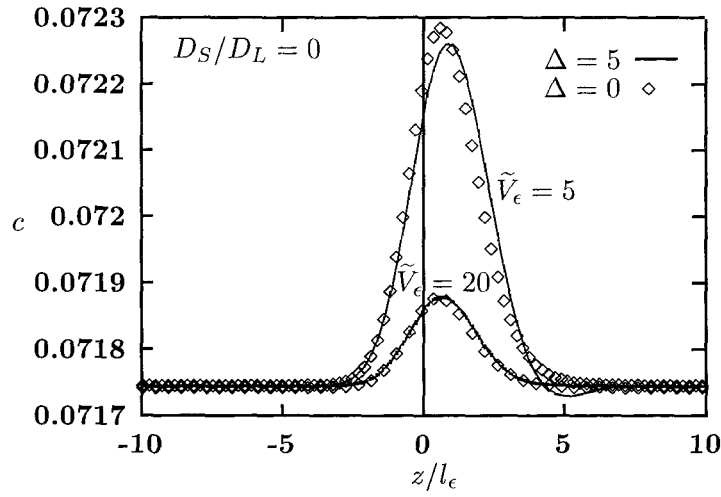


Figure 7.8: The solute profiles for $\Delta = 5$ and $\Delta = 0$ are compared for increasing values of the dimensionless velocity \tilde{V}_ϵ .

In order to investigate whether or not solute trapping occurs as a result of the inclusion of the solute gradient energy term in the free energy functional of the model, we repeat the calculations above for the case when Δ is identically zero, i.e., excluding the solute gradient energy term. For the three increasing values of \tilde{V}_ϵ we considered, i.e., $\tilde{V}_\epsilon = 0.1, 0.3$, and 0.6 (with the domain length L_N of 180, 80 and respectively), the solutions (shown in Fig. 7.6(i)) exhibit a similar trend to the solutions obtained in the previous case. Regardless of the absence of the solute gradient energy term, the degree of segregation decreases monotonically as \tilde{V}_ϵ is reduced. This suggests that the solute gradient energy term is **not a prerequisite** to solute trapping. The results also show a decrease in the characteristic length scale of the solute field as \tilde{V}_ϵ increases.

We go on to compare the solutions in the two cases $\Delta = 0$ and $\Delta \neq 0$, for a much larger value of \tilde{V}_ϵ , and it is found that the solute profile when $\delta \neq 0$ becomes very similar to the profile when $\delta = 0$ (see Fig. 7.6(ii)). In other words, the degree of segregation becomes **increasingly independent of δ** , as \tilde{V}_ϵ becomes large. Thus we can see that in the high \tilde{V}_ϵ regime, the term proportional to the velocity in the solute equation (see (7.6)) dominates the equation causing a minimal effect from the solute gradient term.

7.3.2 Solutions when $D_S/D_L \neq 1$

In real situations, the diffusivity in the solid phase is normally very small compared to that in the liquid. Typically, D_S is four orders of magnitude smaller than D_L . It is therefore natural to explore the changes in the solutions as the ratio of the diffusivities, D_S/D_L , approaches zero. We perform the computations using the same values of ϵ and c_∞ as before. The solute profiles for three different values of D_S/D_L are shown in Fig. 7.7, from which we can see that as the value of D_S/D_L approaches zero, there is a reduction in the maximum value of solute concentration. At the same time, the \bar{z} -coordinate at which the maxima occurs, becomes more positive.

In Fig. 7.8 we compute the solute profiles with $D_S/D_L = 0$, for two different values of \tilde{V}_ϵ , and compare the two cases $\Delta = 0$ and $\Delta \neq 0$. Again, solute trapping is observed with decreasing dependence on δ as \tilde{V}_ϵ is increased.

Model	length scale	limit(s)	dimensionless velocity	solute trapping?
WBM1	l_ϵ	$l_\epsilon/(D/V) \rightarrow 0$	$\tilde{V} = l_\epsilon/(D/V)$	no
WBM2 (Wheeler et. al.'s formulation)	l_ϵ, l_δ	$l_\epsilon/l_\delta \rightarrow 0$	$\tilde{V}_\delta = l_\delta/(D/V)$	yes
WBM2 (our formulation)	l_ϵ	none	$\tilde{V}_\epsilon = l_\epsilon/(D/V)$	yes

Table 7.2: A summary of the results from the analyses of the WBM model.

7.4 The determining factor of solute trapping

In section 7.1, we nondimensionalised the governing equations using the length scale l_ϵ , which is the length scale over which ϕ changes. This is also the length scale used in the WBM1 model [1], where, in the limit $l_\epsilon/(D/V) \rightarrow 0$, the model was unable to capture the solute trapping phenomena. In the generalisation of the WBM1 model, i.e., Wheeler et. al.'s formulation of the WBM2 model, another length scale was introduced, namely, l_δ . This is the length scale associated with the solute field, c . In the limit $l_\epsilon/l_\delta \rightarrow 0$, the model successfully predicts solute trapping when the interface velocity is large. The observations above raise the question of **whether the relative sizes of D/V and, either l_δ or l_ϵ , determine solute trapping**, a question which we will try to answer shortly.

In order to get a clear picture of the relationship between the different length scales and solute trapping, we summarise the results from the three different formulations of the WBM model, in Table 7.2, which shows that the three phase-field formulations share one thing in common, namely, all the dimensionless velocities are defined as the ratio of, either l_ϵ or l_δ , to D/V . The quantity D/V is in fact, the diffusive length scale of the solute field. Thus, in our formulation for example, when the dimensionless velocity, \tilde{V}_ϵ is large, this implies that D/V is ‘small’ compared to l_ϵ . Therefore, we identify the solute trapping phenomena, as the behaviour that results from D/V being **comparable** or **smaller** than the length, with which the interface velocity is scaled. This explains why solute trapping behaviour is captured in Wheeler et. al.'s formulation of the WBM2 model, **and not** in their earlier formulation, i.e., the WBM1 model. The sharp interface limit that was taken in their first analysis, i.e., the limit $l_\epsilon/(D/V) \rightarrow 0$, is equivalent to insisting the D/V is larger than l_ϵ . On the other hand, in the generalised version, the sharp interface limit, $l_\epsilon/l_\delta \rightarrow 0$ (with l_δ fixed), was taken

independent of D/V . Therefore, solute trapping is observed when \tilde{V}_δ is large.

The explanation above mainly concerns the technicalities involved in the nondimensionalisation of the interface velocity. In order to relate the technical aspect to physics, we need to take a closer look at l_ϵ and l_δ , and investigate their relationship with the thickness of the interface.

In section 3.2, the interface thickness is shown to be characterised by l_i , where l_i is given by

$$l_i = \frac{\epsilon^2}{6\sigma_A}. \quad (7.23)$$

This may be written as,

$$l_i = \frac{l_\epsilon}{6\tilde{\sigma}_{A_\epsilon}}, \quad (7.24)$$

where $\tilde{\sigma}_{A_\epsilon} = \sigma_A/(\epsilon\sqrt{RT/v_m})$, or,

$$l_i = \frac{l_\delta}{6\tilde{\sigma}_{A_\delta}}, \quad (7.25)$$

where $\tilde{\sigma}_{A_\delta} = \sigma_A/(\delta\sqrt{RT/v_m})$. Thus, we see that, both l_ϵ and l_δ , are directly proportional to the interface thickness l_i . Hence, we conclude, that **solute trapping occurs when D/V becomes comparable or smaller than the characteristic thickness of the interface.**

It is important to note that, we managed to arrive at the conclusion above, because the phase-field model prescribes a finite thickness to the interface. This is not possible in the CGM, or any of the solute trapping model described in chapter 4, because they are based on a **sharp interface formulation** of solidification. The assumption made in the models, that the interface has **negligible thickness**, prevents a direct relation between the physical length associated with the solute field, and the interface thickness.

7.5 Partition coefficient and diffusive speed

The partition coefficient k , which is defined here as the ratio of the far-field concentration to the maximum concentration of solute, is a parameter used for measuring the degree of solute trapping in rapid solidification. The solutions obtained through the numerical calculations provide a range of values of k for different values of \tilde{V}_ϵ . The observed dependence of k on \tilde{V}_ϵ agrees qualitatively with existing solute trapping models, in that its values increases to unity as \tilde{V}_ϵ gets larger. This is evident from the marked decrease in the maximum concentration of solute (see Fig. 7.6(i)) as \tilde{V}_ϵ increases.

However, many of the existing solute trapping models contain another parameter, namely the diffusive speed V_D , which does not appear explicitly in the WBM2 model. In most

experiments on solute trapping, for example in [4, 8], the value of the diffusive speed is obtained by fitting a suitable solute trapping model to the experimental data, where V_D is treated as a fitting parameter. We will use a similar method to derive a value for the diffusive speed from the numerical values for $k(\tilde{V}_\epsilon)$, and the procedure is described in the following section.

7.5.1 The diffusive speed

In order to demonstrate how V_D is calculated from the numerical solutions we have obtained, a set of values for k are computed for various values of the dimensionless velocity \tilde{V}_ϵ . We again use the data of the nickel copper alloy in appendix B, where ϵ is given as $3.3 \times 10^{-6} \text{J}^{1/2} \text{cm}^{-1/2}$, and k_e is chosen to be 0.7965 which corresponds to a solidus concentration of 7.17441×10^{-2} and temperature of 1700K. The diffusivity ratio D_S/D_L is fixed at 0.5.

A similar procedure as carried out with the experimental results is employed here onwards, i.e, the set of numerical k values is treated in the same way as the experimental k values. Thereby, we performed a *Least Squares Fitting* of the numerical k values with a suitable solute trapping model, which in this case is the Continuous Growth Model (CGM). The CGM is given below where the fitting parameter in this case is the nondimensional value of V_D , namely $\tilde{V}_D = V_D l_\epsilon / D$,

$$\bar{k} = \frac{k_e + \tilde{V}_\epsilon / \tilde{V}_D}{1 + \tilde{V}_\epsilon / \tilde{V}_D}. \quad (7.26)$$

In least squares method, the value of \tilde{V}_D for which CGM fits the numerical data best, is the value for which the following sum of squares, Q , is at its minimum [58],

$$Q = \sum_{i=1}^N (k_i - \bar{k}^i)^2, \quad (7.27)$$

where N is the number of evaluation points, k_i is the numerical value of k corresponds to the i -th value of \tilde{V}_ϵ i.e. \tilde{V}_ϵ^i , and \bar{k}^i is the value of k evaluated from (7.26) at \tilde{V}_ϵ^i . This is the sum of squares of the residuals between the two sets of k values. Q achieves its minimum value when its first derivative with respect to \tilde{V}_D (or $1/\tilde{V}_D$) is identically zero. Hence, the best fit value of \tilde{V}_D satisfies the following equation,

$$\sum_{i=1}^N \frac{d\bar{k}^i}{d(1/\tilde{V}_D)} (k_i - \bar{k}^i) = 0, \quad (7.28)$$

where here, we have differentiated Q with respect to $1/\tilde{V}_D$ for simplicity.

The numerical k values and the fitted k values from CGM are plotted in Fig. 7.9, in which the two sets of data are observed to be almost indistinguishable. The numerical k values are

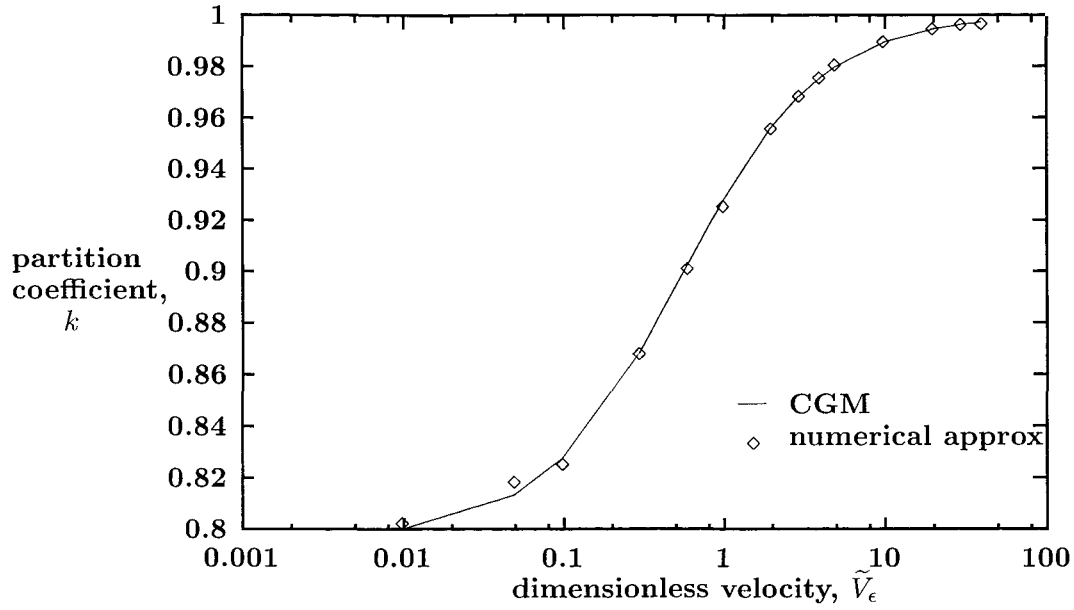


Figure 7.9: The numerical approximation of the partition coefficient k is plotted for various values of the dimensionless velocity \tilde{V}_ϵ . The smooth curve represents the results from least square fitting, with the best-fit value for $\tilde{V}_D = 0.5525$. The diffusivity ratio D_S/D_L is fixed at 0.5. The value of ϵ is $3.3 \times 10^{-6} \text{J}^{1/2} \text{cm}^{-1/2}$, which is the corresponding value for a Nickel-Copper alloy. The equilibrium segregation coefficient k_e is 0.7965 which corresponds to a solidus concentration of 7.17441×10^{-2} and temperature of 1700K.

shown to be close to the equilibrium value of 0.7965 for small \tilde{V}_ϵ , and as \tilde{V}_ϵ increases, k rises to unity. The best-fit value for \tilde{V}_D is found to be 0.5525 which corresponds to a dimensional value of 0.73m/s. Considering how good the numerical values of the partition coefficient for the WBM2 fits the CGM model, it is fair to suggest that the two models have similar physical attributes. This idea will be explored in detail later in section 8.5.

7.5.2 Dependence of V_D on k_e , D_S/D_L and ϵ

We use the least squares fitting method described above to compute \tilde{V}_D for various values of k_e , D_S/D_L and ϵ and extract a value for the dimensional diffusive speed by using the relationship,

$$V_D = \tilde{V}_D D / l_\epsilon.$$

The calculations are performed separately for each of the three parameters, (i.e., k_e , D_S/D_L and ϵ), keeping two of the parameters fixed while varying the third. The quantities D_S/D_L and ϵ are altered without making any changes to the other material parameters. On the other hand, k_e is varied by changing the values of the melting temperature and the latent heat of the

B component of the alloy, namely T_M^B and L_B , according to the relationship $k_e = \exp(-\widetilde{\Delta F_B})$ where $\widetilde{\Delta F_B} = (L_B/(RT/v_m))(T - T_M^B)/T_M^B$. This is equivalent to computing a series of values of V_D corresponding to several component A -based alloys (in our case, these are the Nickel-based alloys).

The values of the dimensional V_D are plotted against each of the three quantities k_e , D_S/D_L and ϵ in Fig. 7.10. In the first diagram, V_D is plotted against k_e in which V_D is observed to decrease with k_e ($k_e < 1$). This inverse correlation is consistent with experimental observation made by Smith et. al. [4]. Because V_D is the value that scales the interface velocity, V , (i.e., V has to be large compared to V_D in order to attain solute trapping), the result above suggests that if the solute partitioning at equilibrium is small (k_e close to unity) (i.e., the liquidus concentration of the solute is almost equal to the solidus concentration), solute trapping can occur at lower values of V . In Fig. 7.10(ii), V_D exhibits an approximately linear increase with the diffusivity ratio D_S/D_L , suggesting trapping of solute occurs more readily when, either D_S is small, i.e., limited diffusion in the solid phase, or D_L is large, i.e., complete diffusion in the liquid phase.

The last plot in Fig. 7.10 is $\ln(V_D)$ against $\ln(\epsilon)$ where the values of $\ln(V_D)$ are observed to decrease linearly with $\ln(\epsilon)$. A straight line of slope -2 is drawn against the data to show that almost all the data points lie near this line. We therefore deduce the following relationship for V_D and ϵ ,

$$\ln(V_D) = -2\ln(\epsilon) + \ln(C_0),$$

or equivalently,

$$V_D = C_1\epsilon^{-2}, \quad (7.29)$$

where C_0 and C_1 are constants, i.e., V_D is inversely proportional to ϵ^2 . But from (7.23), ϵ^2 is shown to be directly proportional to the interface width l_i , implying that V_D is also inversely proportional to l_i . This relationship agrees with the basic hypothesis of CGM that claims $V_D = D_i/l_i$, where D_i is the interface diffusion.

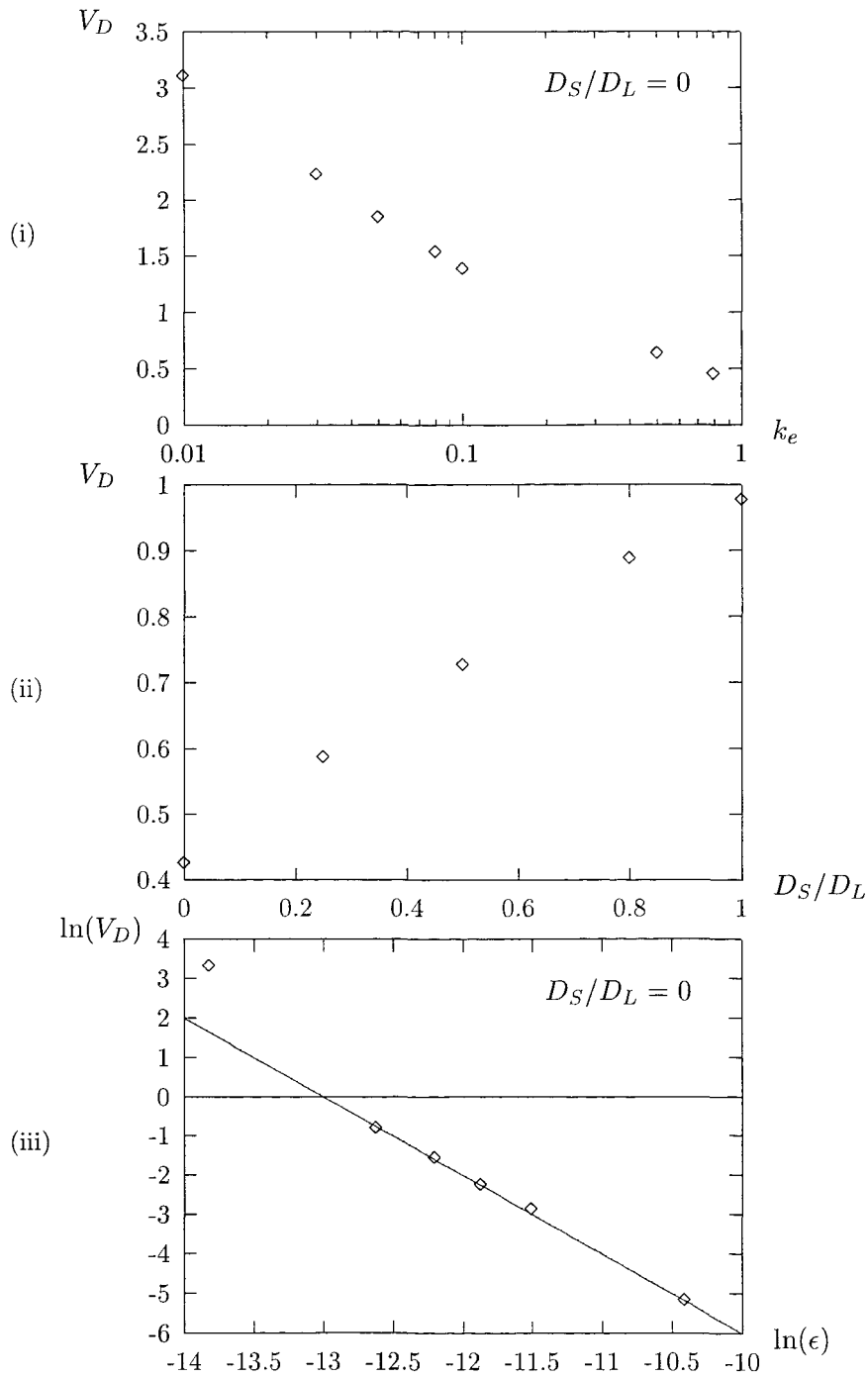


Figure 7.10: (i) A plot of the dimensional diffusive speed V_D against the equilibrium segregation coefficient k_e . The diffusivity ratio is assumed to be zero, and the value of ϵ is fixed at $3.3 \times 10^{-6} \text{ J}^{1/2} \text{ cm}^{-1/2}$, which is the corresponding value for a nickel-copper alloy (see appendix B). (ii) A plot of the dimensional diffusive speed V_D against the diffusivity ratio D_S/D_L . The values of k_e and ϵ are fixed at 0.7925 and $3.3 \times 10^{-6} \text{ J}^{1/2} \text{ cm}^{-1/2}$ respectively. (iii) A plot of $\ln(V_D)$ against $\ln(\epsilon)$, a straight line of slope -2 is drawn against the data showing them lying very close to this line. The value of k_e is fixed at 0.7965.

7.6 Interfacial temperature

The interface temperature appears as an eigenvalue of the governing equations of the WBM2 model. Its value is found numerically along side the phase field and the solute field. For the nickel-copper alloy data, three sets of values are obtained numerically for the temperature, these are for $\Delta = 0$, $\Delta = 10$ and $\Delta = 100$. The three sets of results are plotted in Fig. 7.11(i) where the values are shown to depend weakly on Δ at low interface velocities, this dependence slowly diminishes as \tilde{V}_ϵ is increased. At high velocities, there is a sharp decline in the temperature, exhibiting the so-called *kinetic undercooling* at the interface.

A measure for the undercooling of the melt adjacent to the interface is provided by the interfacial temperature T . Results from sharp interface models (see chapter 2) show that the temperature at the interface may be formulated as a function of the interface velocity V . For dilute alloys, this function is given by (2.9), which is applicable for a process where solute drag is limited. More generally, for dilute alloys with a fixed solid composition, c_∞ , the undercooling function has been derived to be,

$$T = T_M + \frac{m_L c_\infty}{k} \left(\frac{1 - k + \alpha \ln(k/k_e)}{1 - k_e} \right) - \frac{V}{\mu}, \quad (7.30)$$

where T_M is the pure (solvent) melting point, m_L is the slope of the liquidus, and μ is the interface kinetic coefficient for the pure solvent. The value of the parameter α depends on whether or not ‘solute drag’ effect is included, it is equal to k when solute drag is neglected and equal to unity when solute drag is included. This expression was deduced by Aziz and Boettinger [68] from the consideration of the effective free energy difference between liquid and solid during solidification, using Turnbull’s collision-limited growth model [69] and the Continuous Growth Model [19].

We compare the numerical values for the interface temperature corresponding to $\Delta = 0$, with the sharp interface prediction given in (7.30), by plotting the two results in Fig. 7.11(ii). For both cases, with and without solute drag, the numerical solution agrees very well with the sharp interface result. The agreement is observed to get better as the interface velocity increases.

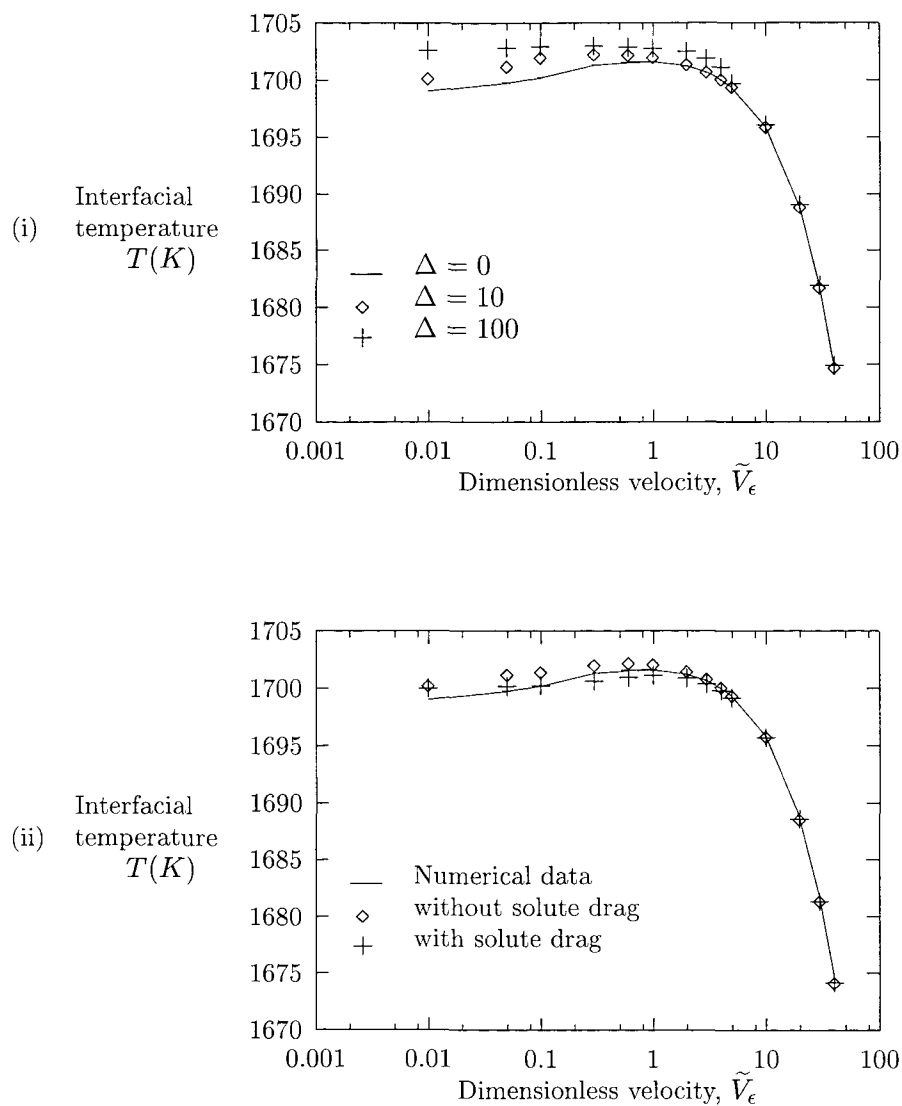


Figure 7.11: (i) The temperature profile is plotted for $\Delta = 0, 10$ and 100 , which corresponds to $\delta = 0, 3.3 \times 10^{-5}$ and $3.3 \times 10^{-4} \text{ J}^{1/2} \text{ cm}^{-1/2}$ respectively. (ii) The numerical solution for the interfacial temperature is compared with the sharp-interface predictions, with and without solute drag.

Chapter 8

The high solidification velocity limit with δ/ϵ constant

The numerical calculations in chapter 7 indicated that the WBM2 model has successfully captured the solute trapping behaviour, irrespective of the value of the solute gradient energy coefficient δ . Moreover, the solution for the solute field with δ nonzero, approaches the solution when $\delta = 0$, as \tilde{V}_ϵ is increased. This result provides a useful indication of the weak influence the solute gradient energy term has on the model when the interface velocity is large.

In order to investigate the trapping phenomenon further, it is appropriate to perform an asymptotic analysis of the governing equations in the large \tilde{V}_ϵ regime. This is carried out below for both cases when $D_S/D_L = 1$ and when $D_S/D_L \neq 1$. The asymptotic expressions for the partition coefficient k in both cases, are compared with the large V/V_D asymptotic expansion of the partition coefficient from the CGM, from which, expressions for the diffusive speed V_D are established. The values of V_D obtained from the more realistic expression where $D_S/D_L \approx 0$ are compared with the experimental values obtained by Smith et. al [4], and very good agreement is found.

8.1 Asymptotic analysis for $\tilde{V}_\epsilon \rightarrow \infty$

We will first explore the form of the solutions when the diffusivity ratio, D_S/D_L , is equal to unity. We proceed by expanding the solution as a regular perturbation series in \tilde{V}_ϵ^{-1} ,

$$\phi = \phi^{(0)}(\tilde{z}) + \tilde{V}_\epsilon^{-1}\phi^{(1)}(\tilde{z}) + \mathcal{O}(\tilde{V}_\epsilon^{-2}), \quad (8.1)$$

$$c = c^{(0)}(\tilde{z}) + \tilde{V}_\epsilon^{-1}c^{(1)}(\tilde{z}) + \mathcal{O}(\tilde{V}_\epsilon^{-2}), \quad (8.2)$$

as $\tilde{V}_\epsilon \rightarrow \infty$. Substituting these expansions into (7.4) and (7.6) gives, at leading order,

$$\frac{d^2\phi^{(0)}}{d\tilde{z}^2} + \frac{\tilde{V}_\epsilon}{\tilde{m}} \frac{d\phi^{(0)}}{d\tilde{z}} - \left(\tilde{f}_\phi^{(-2)}(\phi^{(0)}, c^{(0)}) + \tilde{f}_\phi^{(0)}(\phi^{(0)}, c^{(0)}) \right) = 0, \quad (8.3)$$

and

$$c^{(0)} = c_\infty. \quad (8.4)$$

The quantity \tilde{m} is shown in chapter 5 to be related to the dimensional interface kinetic coefficient of A , μ_A , by

$$\tilde{m} = \frac{\mu_A \sigma_A T_M^{(A)}}{L_A D}.$$

For the Ni-Cu alloy, this value turns out to be rather large compared to typical values of \tilde{V}_ϵ . Under this assumption, we infer that it is quite acceptable to assume $\tilde{V}_\epsilon/\tilde{m}$ is small and therefore assume the second term in (8.3) is negligible. In which case, the equation (8.3) has the solution,

$$\phi^{(0)}(\tilde{z}) = \frac{1}{2}[1 - \tanh(3\tilde{\sigma}^* \tilde{z})], \quad (8.5)$$

where

$$\tilde{\sigma}^* = \sigma^* / \left(\epsilon \sqrt{RT/v_m} \right)$$

with

$$\sigma^* = \sqrt{c_\infty \sigma_B^2 + (1 - c_\infty) \sigma_A^2};$$

when

$$\tilde{f}_\phi^{(0)} = 0.$$

This latter condition is met when

$$\tilde{f}(1, c_\infty) = \tilde{f}(0, c_\infty). \quad (8.6)$$

Solving for T from (8.6) gives the temperature when free energy curves of the solid and liquid intersect, i.e., solid and liquid phases have the same free energy density. Denoting this temperature by T_0 we find,

$$T_0 = \frac{c_\infty L_B + (1 - c_\infty) L_A}{c_\infty L_B / T_M^{(B)} + (1 - c_\infty) L_A / T_M^{(A)}}. \quad (8.7)$$

It is a simple matter to generalise the above, to the case when $\tilde{V}_\epsilon/\tilde{m}$ is not small where, in this case, the temperature is given by

$$T = T_0 - \frac{V \sigma^*}{\tilde{m} D [c_\infty L_B / T_M^B + (1 - c_\infty) L_A / T_M^A]}. \quad (8.8)$$

In the dilute limit, i.e., when $c_\infty \approx 0$, $T_0 \approx T_M^A$ and $\sigma^* \approx \sigma_A$, (8.8) may be approximated as

$$T \approx T_M^A - \frac{V}{\mu_A}. \quad (8.9)$$

Notice that the extra term in the temperature equation (8.8) is in fact the kinetic undercooling term, which is a non-equilibrium effect. Thus, by neglecting the term $\tilde{V}_\epsilon/\tilde{m}$, we are in fact neglecting the non-equilibrium effect on the temperature caused by the high interface velocity.

We proceed to find the next order term in the asymptotic solution for the solute concentration, and we obtain the following,

$$c^{(1)} = -c_\infty(1 - c_\infty) \frac{d\phi^{(0)}}{d\tilde{z}} \left(\tilde{f}_{c\phi}^{(-2)}(\phi^{(0)}, c_\infty) + \tilde{f}_{c\phi}^{(0)}(\phi^{(0)}, c_\infty) \right), \quad (8.10)$$

with $\phi^{(0)} = \frac{1}{2}[1 - \tanh(3\tilde{\sigma}_0^*\tilde{z})]$, where $\tilde{\sigma}_0^* = \sigma/(\epsilon\sqrt{RT_0/v_m})$. Writing (8.10) explicitly, we have

$$c^{(1)} = \frac{27}{2}c_\infty(1 - c_\infty)\tilde{\sigma}_0^*(\tilde{\sigma}_{B0}^2 - \tilde{\sigma}_{A0}^2)[1 - \tanh^2(3\tilde{\sigma}_0^*\tilde{z})]^2[\tanh(3\tilde{\sigma}_0^*\tilde{z}) + \tilde{\nu}], \quad (8.11)$$

where

$$\tilde{\nu} = \frac{\Delta\widetilde{F}_{B0} - \Delta\widetilde{F}_{A0}}{6(\tilde{\sigma}_{B0}^2 - \tilde{\sigma}_{A0}^2)}, \quad (8.12)$$

$$\tilde{\sigma}_{A0} = \sigma_A/(\epsilon\sqrt{RT_0/v_m}); \quad \tilde{\sigma}_{B0} = \sigma_B/(\epsilon\sqrt{RT_0/v_m}),$$

and,

$$\Delta\widetilde{F}_{A0} = \frac{L_A}{[RT_0/v_m]} \frac{(T_0 - T_M^A)}{T_M^A}; \quad \Delta\widetilde{F}_{B0} = \frac{L_B}{[RT_0/v_m]} \frac{(T_0 - T_M^B)}{T_M^B}.$$

Note that the form obtained for $c^{(1)}$ here is a quintic in $\tanh(3\tilde{\sigma}_0^*\tilde{z})$ (an asymmetric function), and it reduces to $\text{sech}^4(3\tilde{\sigma}_0^*\tilde{z})$ when $\tilde{\nu} \gg \tanh(3\tilde{\sigma}_0^*\tilde{z})$ (a symmetric function). This observation suggests a transition in the profile of $c^{(1)}$, from asymmetric to symmetric, as $\tilde{\nu}$ is increased. The plot of $c^{(1)}$ for increasing values of $\tilde{\nu}$ shown in Fig. 8.1 confirms this prediction. For small values of $\tilde{\nu}$, the profile has a local maximum and a local minimum. As we increase the value of $\tilde{\nu}$, the profile becomes symmetric about $\tilde{z} = \tilde{z}_{max}$, where \tilde{z}_{max} is the \tilde{z} coordinate of the local maximum of $c^{(1)}$. At this point, the local minimum disappears, at the same time, \tilde{z}_{max} becomes less negative and approaches zero.

We are now able to proceed to find the corresponding asymptotic expression for the partition coefficient k . This involves determining an estimate for the maximum concentration, which will be calculated from the asymptotic expression derived for c above. It is discussed in detail in the following section.

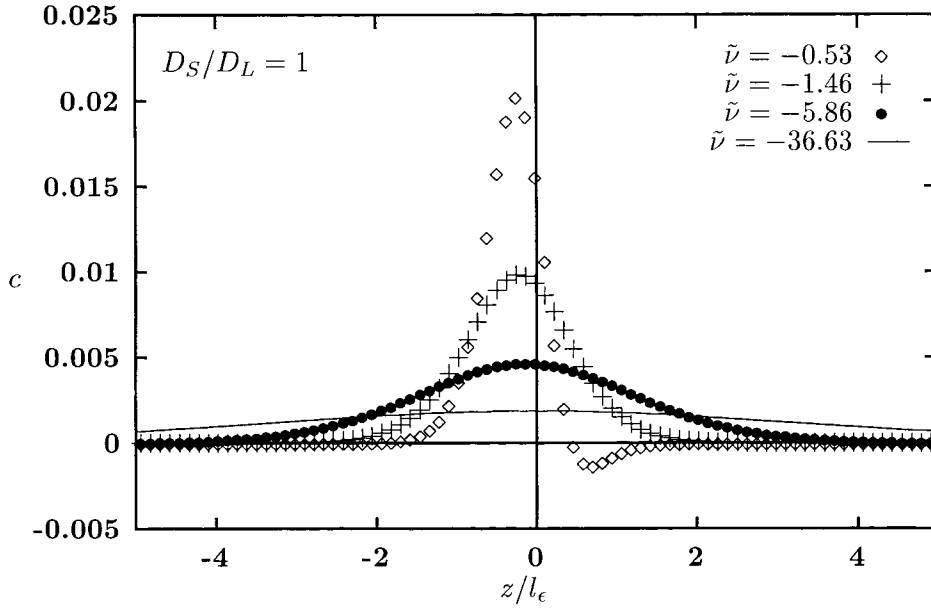


Figure 8.1: The $c^{(1)}$ profiles for values of $\tilde{\nu}$ ranging from -0.53 to -36.63 . These values correspond to values of ϵ of 1.98×10^{-6} , 3.3×10^{-6} , 6.6×10^{-6} and $1.65 \times 10^{-5} \text{ J}^{1/2} \text{ cm}^{-1/2}$ respectively.

8.1.1 Partition coefficient and solute trapping

In order to establish an asymptotic expansion for k in \tilde{V}_ϵ^{-1} , we need to calculate the maximum value of the solute concentration c , and therefore, a detailed analysis of the form of c is required. It is simple to see that, to $\mathcal{O}(\tilde{V}_\epsilon^{-1})$, c attains its maximum when $c^{(1)}$ is at its largest. Hence, we differentiate $c^{(1)}$ once with respect to \tilde{z} , in order to analyse its turning points, i.e., the \tilde{z} -coordinate for which $dc/d\tilde{z} = 0$. It follows from this analysis that the \tilde{z} -coordinate at which the maximum/minimum of $c^{(1)}$ occurs can be obtained by solving the following quadratic in $\tanh(3\tilde{\sigma}_0^* \tilde{z})$:

$$\tanh^2(3\tilde{\sigma}_0^* \tilde{z}) + \frac{4}{5} \tilde{\nu} \tanh(3\tilde{\sigma}_0^* \tilde{z}) - \frac{1}{5} = 0. \quad (8.13)$$

The solutions to (8.13) are given by the following equation,

$$\tanh(3\tilde{\sigma}_0^* \tilde{z}) = -\frac{2}{5} \tilde{\nu} \pm \sqrt{\frac{4}{25} \tilde{\nu}^2 + \frac{1}{5}}, \quad (8.14)$$

which gives two values for \tilde{z} ,

$$\tilde{z} = \tilde{z}_- = \frac{1}{3\tilde{\sigma}_0^*} \tanh^{-1} \left(-\frac{2}{5} \tilde{\nu} - \sqrt{\frac{4}{25} \tilde{\nu}^2 + \frac{1}{5}} \right), \quad (8.15)$$

and

$$\tilde{z} = \tilde{z}_+ = \frac{1}{3\tilde{\sigma}_0^*} \tanh^{-1} \left(-\frac{2}{5} \tilde{\nu} + \sqrt{\frac{4}{25} \tilde{\nu}^2 + \frac{1}{5}} \right), \quad (8.16)$$

Solutions (8.15) and (8.16) exist only when the modulus of the right hand side of equation (8.14) is less than unity. Therefore, in order to investigate which of the two roots exists, we expanding the square root in (8.14) for the two cases, $|\tilde{\nu}| > 1$ and $|\tilde{\nu}| < 1$, and obtain the following expansions for $\tanh(3\tilde{\sigma}_0^* \tilde{z})$,

(1) the case $|\tilde{\nu}| > 1$,

$$\tanh(3\tilde{\sigma}_0^* \tilde{z}) = \begin{cases} \frac{1}{4}\tilde{\nu}^{-1} - \frac{5}{64}\tilde{\nu}^{-3} + \mathcal{O}(\tilde{\nu}^{-5}), \\ \text{or} \\ -\frac{4}{5}\tilde{\nu} - \frac{1}{4}\tilde{\nu}^{-1} + \frac{5}{64}\tilde{\nu}^{-3} + \mathcal{O}(\tilde{\nu}^{-5}); \end{cases} \quad \text{as } |\tilde{\nu}| \rightarrow \infty. \quad (8.17)$$

(2) the case $|\tilde{\nu}| < 1$,

$$\tanh(3\tilde{\sigma}_0^* \tilde{z}) = \begin{cases} -\frac{\sqrt{5}}{5} - \frac{2}{5}\tilde{\nu} + \frac{2\sqrt{5}}{25}\tilde{\nu}^2 + \mathcal{O}(\tilde{\nu}^4), \\ \text{or} \\ \frac{\sqrt{5}}{5} - \frac{2}{5}\tilde{\nu} - \frac{2\sqrt{5}}{25}\tilde{\nu}^2 + \mathcal{O}(\tilde{\nu}^4), \end{cases} \quad \text{as } |\tilde{\nu}| \rightarrow 0. \quad (8.18)$$

We see that when $|\tilde{\nu}| < 1$, both roots exist. On the other hand, when $|\tilde{\nu}| > 1$, the modulus of the second expansion in (8.17) may become greater than unity, when $|\tilde{\nu}|$ is large enough. The critical value of $|\tilde{\nu}|$, i.e., the value that corresponds to $|\tanh(3\tilde{\sigma}_0^* \tilde{z})| = 1$, $|\tilde{\nu}_c|$ say, may easily be calculated from (8.13) to be unity. Therefore we infer that when $|\tilde{\nu}| > 1$, only \tilde{z}_- exists.

The two roots \tilde{z}_- and \tilde{z}_+ , determine the \tilde{z} coordinate of the turning points of $c^{(1)}$. Let us now refer to the profiles in Fig. 8.1, where $c^{(1)}$ is plotted for increasing values of $|\tilde{\nu}|$. The plot indicates that, for $|\tilde{\nu}| = 0.53$ (which is less than $|\tilde{\nu}_c|$), the two roots correspond to a **local maximum** and a **local minimum**. It also shows that the root corresponding to the local maximum (\tilde{z}_{max} say) is more negative than the root corresponding to the local minimum (denoted as \tilde{z}_{min}). Now, assuming $\tilde{\nu}$ is negative¹, equations (8.15) and (8.16) imply

$$\tilde{z}_- < \tilde{z}_+,$$

where we have assumed $\tanh(3\tilde{\sigma}_0^* \tilde{z}) \approx 3\tilde{\sigma}_0^* \tilde{z}$. We then infer that $c^{(1)}$ has a local maxima at

$$\tilde{z} = \tilde{z}_{max} = \tilde{z}_-,$$

and a local minimum at

$$\tilde{z} = \tilde{z}_{min} = \tilde{z}_+.$$

¹This is true when the surface energy of the B component of the alloy is less than that of the A component (i.e., $\sigma_B < \sigma_A$)

Thus, the concentration profile has a local maximum for all values of $|\tilde{\nu}|$, and the \tilde{z} coordinate of the maximum is given by (8.15).

It appears that the maximum value of $c^{(1)}$, i.e., $c^{(1)}(\tilde{z}_{max}) = c_{max}^{(1)}$, is very dependent on the magnitude of $\tilde{\nu}$, and because the partition coefficient, k , depends on the maximum value of the concentration (i.e., $c_{max}^{(1)}$), we also expect k to depend on $\tilde{\nu}$. In fact, it can be shown that $\tilde{\nu}$ is directly related to the **equilibrium partition coefficient**, k_e . In order to see this more clearly, we refer to equation (6.19), where for **ideal solutions**,

$$k_e = \exp(-\widetilde{\Delta F}_{B0}), \quad (8.19)$$

which implies that,

$$\widetilde{\Delta F}_{B0} = \ln(1/k_e). \quad (8.20)$$

Now, in the *dilute alloy limit*, i.e., the limit when the mole fraction of the B component of the alloy is very small compared to that of A , $c_\infty \approx 0$ and $T_0 \approx T_M^A$, which gives,

$$\begin{aligned} \tilde{\nu} &\approx \frac{\widetilde{\Delta F}_{B0}}{6(\tilde{\sigma}_{B0}^2 - \tilde{\sigma}_{A0}^2)}, \\ &= \frac{\ln(1/k_e)}{6(\tilde{\sigma}_{B0}^2 - \tilde{\sigma}_{A0}^2)}, \end{aligned} \quad (8.21)$$

thus, $|\tilde{\nu}|$ has a specific value for each alloy. Equation (8.21) indicates that large values of $|\tilde{\nu}|$ correspond to small values of k_e . A rough estimate for $c_{max}^{(1)}$ in this case, is given by,

$$c_{max}^{(1)} = \frac{27}{2} c_\infty (1 - c_\infty) \tilde{\sigma}_0^* (\tilde{\sigma}_{B0}^2 - \tilde{\sigma}_{A0}^2) \tilde{\nu} + \mathcal{O}(\tilde{\nu}^{-2}), \quad (8.22)$$

where we have approximated $\tanh(3\tilde{\sigma}_0^* \tilde{z})$ as $\frac{1}{4}\tilde{\nu}^{-1}$.

Equation (8.21) also shows that the case $|\tilde{\nu}|$ small, corresponds to $k_e \approx 1$. In such a case, from the first expansion in (8.18) that $\tanh(3\tilde{\sigma}_0^* \tilde{z}_{max}) \approx -\frac{\sqrt{5}}{5}$, it follows that

$$c_{max}^{(1)} = \frac{27}{2} c_\infty (1 - c_\infty) \tilde{\sigma}_0^* (\tilde{\sigma}_{B0}^2 - \tilde{\sigma}_{A0}^2) \left[-\frac{\sqrt{5}}{5} + \frac{3}{5} \tilde{\nu} + \frac{2\sqrt{5}}{25} \tilde{\nu}^2 + \mathcal{O}(\tilde{\nu}^4) \right]. \quad (8.23)$$

Having obtained the value for the maximum concentration, the partition coefficient may be derived as follows,

$$k = \frac{c_\infty}{c_{max}} \quad (8.24)$$

$$\begin{aligned} &= \frac{c_\infty}{c_\infty + \tilde{V}_\epsilon^{-1} c_{max}^{(1)} + \mathcal{O}(\tilde{V}_\epsilon^{-2})} \\ &= 1 - \frac{c_{max}^{(1)}}{c_\infty} \tilde{V}_\epsilon^{-1} + \mathcal{O}(\tilde{V}_\epsilon^{-2}). \end{aligned} \quad (8.25)$$

We see from this expression that as \tilde{V}_ϵ increases, k increases to unity, in other words **solute trapping** occurs. This result can be confirmed from the profiles of c for increasing values

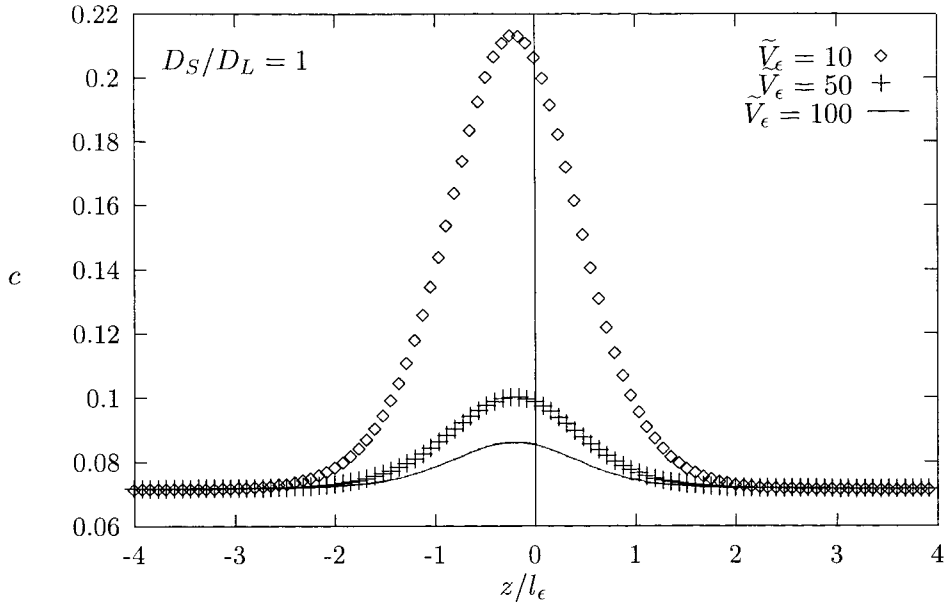


Figure 8.2: The profiles of the asymptotic solutions for c given in equation (8.2), with $c^{(1)}$ given by (8.11), Terms of $\mathcal{O}(\tilde{V}_\epsilon)$ and smaller are ignored. The profiles are drawn for $\tilde{V}_\epsilon = 10, 50$ and 100 . The value of $\tilde{\nu}$ corresponds to that of the Nickel-Copper alloy, which is -1.46 .

of \tilde{V}_ϵ , depicted in Fig. (8.2). The plots show a decrease in the maximum value of c as \tilde{V}_ϵ increases, exhibiting solute trapping. It is also important to note that, to first order in \tilde{V}_ϵ , k is independent of δ . This result is in agreement with the numerical results, from which it is implied that **the solute gradient energy is not needed** in the model, in order for it to capture the trapping phenomenon.

8.1.2 Diffusive speed

From the Continuous Growth Model (CGM) (see section (4.2.2)), the dilute limit of the partition coefficient is given by equation (4.14) and can be written as an asymptotic expansion in V_D/V ,

$$k = 1 + (k_e - 1) \frac{V_D}{V} + \mathcal{O}([V_D/V]^{-2}). \quad (8.26)$$

It is possible to obtain an expression for the diffusive speed V_D as a function of the equilibrium partition coefficient k_e , and the diffusivity D , if we assumed (8.26) is equal to (8.24), in which case, the following relation holds,

$$V_D = \left(\frac{c_{max}^{(1)}}{c_\infty} \right)^* \frac{D}{l_\epsilon(1 - k_e)}. \quad (8.27)$$

The quantity $\left(\frac{c_{max}^{(1)}}{c_\infty} \right)^*$ denotes the dilute limit of $\frac{c_{max}^{(1)}}{c_\infty}$.

Large $\tilde{\nu}$, small k_e

Now, for large $|\tilde{\nu}|$, we have

$$\begin{aligned} \frac{c_{max}^{(1)}}{c_\infty} &= \frac{27}{2} (1 - c_\infty) \tilde{\sigma}_0^* (\tilde{\sigma}_{B0}^2 - \tilde{\sigma}_{A0}^2) \tilde{\nu} + \mathcal{O}(\tilde{\nu}^{-2}), \\ &= \frac{9}{4} \tilde{\sigma}_0^* (\Delta \widetilde{F}_{B0} - \Delta \widetilde{F}_{A0}) + \mathcal{O}(\tilde{\nu}^{-2}). \end{aligned} \quad (8.28)$$

In the dilute limit, $T_0 \approx T_M^A$ and $c_\infty \approx 0$, therefore, the expansion in (8.28) can be approximated as,

$$\left(\frac{c_{max}^{(1)}}{c_\infty} \right)^* = \frac{9}{4} \tilde{\sigma}_A \ln(1/k_e) + \mathcal{O}(\tilde{\nu}^{-2}). \quad (8.29)$$

Substituting (8.29) into (8.27) we obtain the following expression for the diffusive speed,

$$V_D = \frac{9}{4} \frac{D \tilde{\sigma}_A \ln(1/k_e)}{l_\epsilon(1 - k_e)} + \mathcal{O}(\tilde{\nu}^{-2}). \quad (8.30)$$

Ignoring terms of $\mathcal{O}(\tilde{\nu}^{-2})$ and smaller, we write (8.30) in terms of the dimensional quantities, this is,

$$V_D = \frac{9}{4} \frac{D \sigma_A \ln(1/k_e)}{\epsilon^2(1 - k_e)}. \quad (8.31)$$

From (7.23),

$$\frac{\sigma_A}{\epsilon^2} = \frac{1}{6l_i},$$

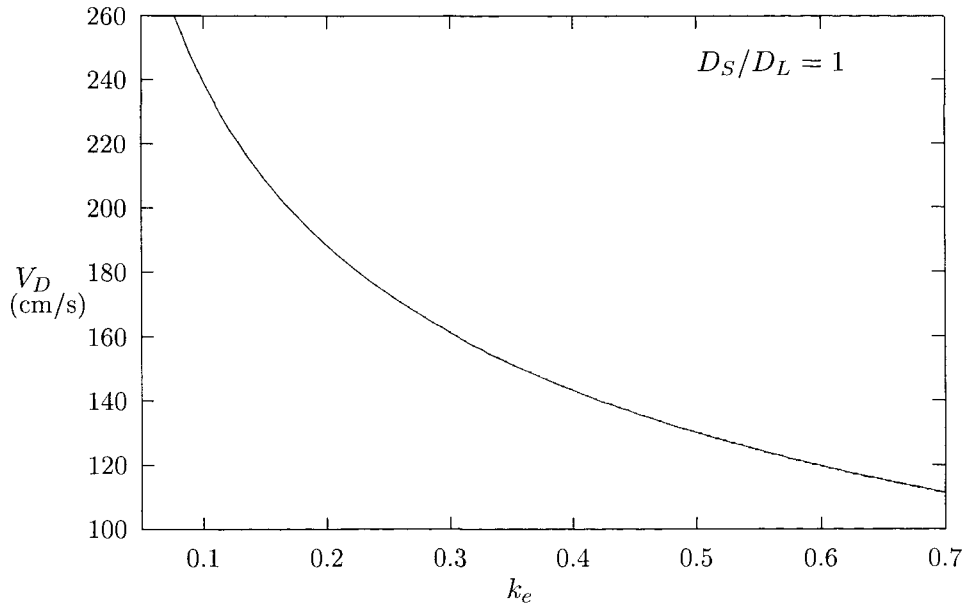


Figure 8.3: The dependence of the asymptotic approximation of V_D on k_e .

which, after substitution into (8.31) gives,

$$V_D = \frac{3 D \ln(1/k_e)}{8 l_i (1 - k_e)}. \quad (8.32)$$

This equation shows a direct relation between V_D and both the diffusion coefficient and the interface thickness, and it differs from the basic hypothesis of CGM, namely $V_D \approx D/l_i$, by a factor which is a function of k_e . We use this final expression to produce a plot of V_D against k_e (see figure (8.3)). It shows an inverse correlation between V_D and k_e , when k_e is small. This observation agrees with the experiment results obtained by Smith et. al. [4], where the prediction they made is based on alloys that have values of k_e ranging from 0.0007 to 0.3.

In this case, we have,

$$\left(\frac{c_{max}^{(1)}}{c_\infty}\right)^* = \frac{9}{4}\tilde{\sigma}_A(\tilde{\sigma}_{B0}^2 - \tilde{\sigma}_{A0}^2) \left[-\frac{\sqrt{5}}{5} + \frac{3}{5}\tilde{\nu} + \mathcal{O}(\tilde{\nu}^2)\right] \quad (8.33)$$

The diffusive speed, V_D , is then given by,

$$V_D = \frac{9}{4} \frac{D\tilde{\sigma}_A(\tilde{\sigma}_{B0}^2 - \tilde{\sigma}_{A0}^2)}{l_\epsilon(1 - k_e)} \left[-\frac{\sqrt{5}}{5} + \mathcal{O}(\tilde{\nu})\right], \quad (8.34)$$

where we can see that, to leading order in $\tilde{\nu}$, a singularity exists at $k_e = 1$.

The singularity is caused by the definition we have used for k_e (see equation (8.19)), which is derived using the common tangent construction, and restricted to alloys with the **idealised phase diagram**. This definition implies that $\widetilde{\Delta F}_{B0} = 0$ whenever $k_e = 1$, which in turn suggests that the interface temperature is equal to T_M^B , the melting temperature of the B component of the alloy (i.e., the solute). In other words, for the ideal solution case, this corresponds to the solidification of pure B , which is not applicable in the dilute limit we have taken (i.e., the limit $c \rightarrow 0$, where c is the mole fraction of B in the alloy). It clearly shows that the ideal solution model is not capable for estimating V_D for $k_e \approx 1$. A more adequate model would require the addition of non-ideal mixing entropy terms in the corresponding free energy density function, an example of which, is given in chapter 6, where the regular solution formulation of the WBM2 model is described.

In summary, the derivation of equation (8.32) is a breakthrough in the development of the theory of solute trapping. The equation, not only confirms the experimental prediction, it also provides an explicit form for the diffusive speed V_D , which, to date, remains as a fitting parameter. The direct relationship between the diffusive speed, V_D , and the material parameters, will enable us to provide an estimate of V_D , for any alloy systems in which the value is not available. Because equation (8.32) only applies for small values of k_e , a better estimate, which would hold for a wider range of k_e , is clearly needed. Such an estimate may be obtained by considering the phase-field formulation for non-ideal solutions.

8.1.3 Extension to cases $k_e > 1$ and $\tilde{V}_\epsilon < 0$.

In this section, the earlier analyses of the partition coefficient and the diffusive speed in the large \tilde{V}_ϵ limit, is extended to the two cases, i) $k_e > 1$ and, ii) $\tilde{V}_\epsilon < 0$, which are discussed separately below. We will only consider the case where $|\tilde{\nu}|$ is large in the following analyses, i.e., we ignore the region where $k_e \approx 1$.

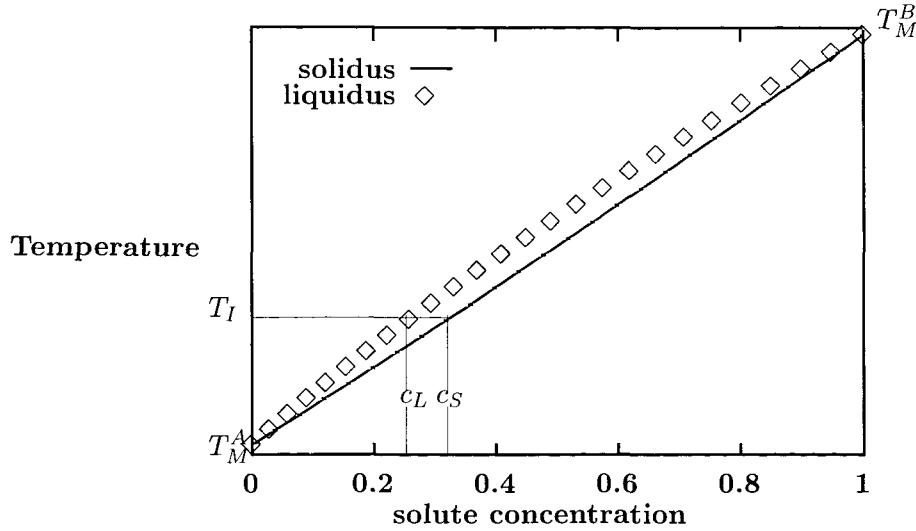


Figure 8.4: The ideal solution phase diagram for an alloy whose equilibrium segregation coefficient k_e is greater than 1.

The case $k_e > 1$.

Throughout the analysis of the WBM2 model, we have mainly assumed the equilibrium segregation coefficient k_e is less than unity. There are cases in which the alloys have $k_e > 1$. These are the cases where the melting point of the B component of the alloy (i.e., the solute) is higher than the melting point of the A component (i.e., the solvent). The idealised phase diagram for such a system is given in Fig. 8.4.

The asymptotic results can easily be extended to this case, where the only significant difference is that $T_M^A < T_M^B$. It will result in a change in the signs of $\widetilde{\Delta F}_{A0}$ and $\widetilde{\Delta F}_{B0}$, which in turns changes the sign of $c_{max}^{(1)}$, i.e., $c_{max*}^{(1)} = -c_{max}^{(1)}$ where $c_{max*}^{(1)}$ is the new value of $c_{max}^{(1)}$ (see definition of $c_{max}^{(1)}$ in (8.22)). This causes the asymptotic expansion for the partition coefficient k to differ slightly from the case $k_e < 1$, it is now given by,

$$\begin{aligned} k &= 1 - \frac{c_{max*}^{(1)}}{c_\infty} \tilde{V}_\epsilon^{-1} + \mathcal{O}(\tilde{V}_\epsilon^{-2}), \\ &= 1 + \frac{c_{max}^{(1)}}{c_\infty} \tilde{V}_\epsilon^{-1} + \mathcal{O}(\tilde{V}_\epsilon^{-2}), \end{aligned} \quad (8.35)$$

which shows that as $\tilde{V}_\epsilon \rightarrow \infty$, k approaches unity from above, i.e., solute trapping.

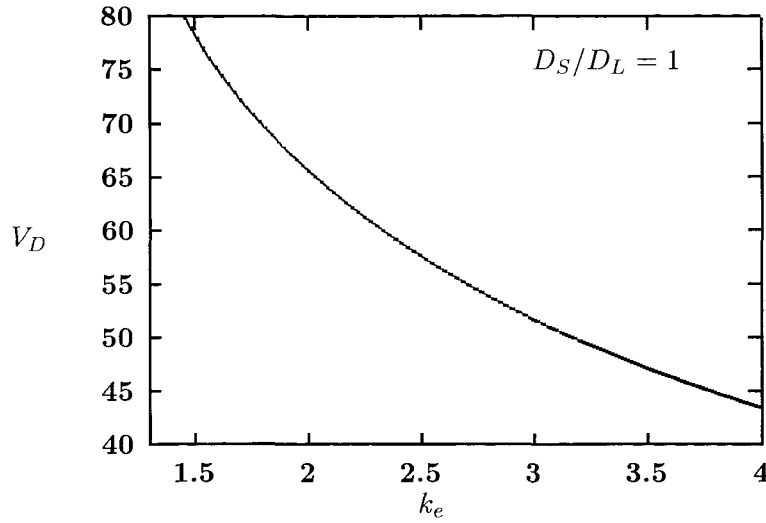


Figure 8.5: The diffusive speed V_D , is plotted against k_e , where k_e is greater than 1.

Because $\widetilde{\Delta F}_{B0}$ changes sign, so will the exponent of the earlier definition of k_e derived from common tangent construction (see equation (6.19)), giving the following new expression for it,

$$k_e = \exp(\widetilde{\Delta F}_{B0}).$$

Consequently, a corresponding expression (for $k_e \gg 1$) can be derived for the diffusive speed V_D , which is,

$$V_D = \frac{3}{8} \frac{D \ln(k_e)}{l_i(k_e - 1)}. \quad (8.36)$$

This new form for V_D is plotted against k_e in Fig. 8.5 and it displays exactly the same correlation as in the previous case with $k_e < 1$, i.e., V_D decreases with k_e . (Note that expression (8.36) is only valid for $k_e \gg 1$. The same singularity is found at $k_e = 1$ because of the same argument given for the case $k_e < 1$ earlier). With this evidence, we conclude that the solute trapping results obtained, is applicable for both cases $k_e < 1$ and $k_e > 1$.

The case $\widetilde{V}_\epsilon < 0$

This refers to a **melting** process, in which the solid-liquid interface advances into the solid. The expected ideal solution phase diagram for this process is shown in Fig. 8.6, where, for dilute alloys, the interface temperature lies close to the melting temperature of B . We can see from the phase diagram that $c_S > c_L$, which implies $k_e > 1$. Thus, we can expect to obtain similar forms for k and V_D as in the last case.

Minor changes are needed in the formulation of the problem in order to account for the melting process. The change in the direction of the interface requires \widetilde{V}_ϵ to be replaced

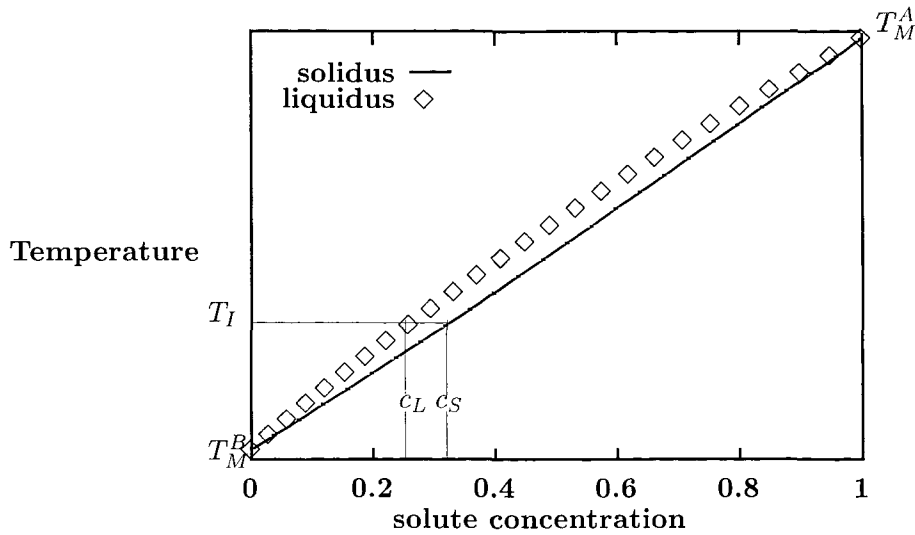


Figure 8.6: The ideal solution phase diagram for an alloy undergoing a melting process.

with $-\tilde{V}_\epsilon$. Also, from the phase diagram it is straightforward to see that the two melting temperatures have changed roles. For dilute alloys, the process occurs at the lower end of the temperature scale, i.e., near T_M^B . To alter the current model, we simply replace T_M^A , whenever it appears, with T_M^B .

Having worked through the asymptotic analysis again, applying all the required changes, we indeed find the same expressions for k and V_D as for the case $k_e > 1$. This shows that the two cases are equivalent when applied to the dilute limit. It also implies that solute trapping during melting occurs in a similar manner as we see in a solidification process.

8.2 Varying diffusivity

We can extend the analysis, as before in (7.10) and (7.11), where the diffusivity is allowed to be different in each phase. The analysis leads to the same leading order solutions (8.3) and (8.4). At $\mathcal{O}(\tilde{V}_\epsilon)$ we obtain

$$c^{(1)} = - \left[\left(\frac{D_S}{D_L} - 1 \right) \phi^{(0)2} (3 - 2\phi^{(0)}) + 1 \right] c_\infty (1 - c_\infty) \frac{d\phi^{(0)}}{d\tilde{z}} \left(\tilde{f}_{c\phi}^{(-2)}(\phi^{(0)}, c_\infty) + \tilde{f}_{c\phi}^{(0)}(\phi^{(0)}, c_\infty) \right), \quad (8.37)$$

which, after the substitution of $\phi^{(0)}$ gives,

$$c^{(1)} = \frac{27}{2} c_\infty (1 - c_\infty) \tilde{\sigma}_0^* (\tilde{\sigma}_{B0}^2 - \tilde{\sigma}_{A0}^2) (1 - \tanh^2(3\tilde{\sigma}_0^* \tilde{z}))^2 (\tanh(3\tilde{\sigma}_0^* \tilde{z}) + \tilde{\nu}) \\ \times \left[\frac{1}{4} \left(\frac{D_S}{D_L} - 1 \right) (2 - \tanh(3\tilde{\sigma}_0^* \tilde{z}) + \tanh^3(3\tilde{\sigma}_0^* \tilde{z})) + 1 \right]. \quad (8.38)$$

8.2.1 Partition coefficient

We repeat the calculations in section (8.1.1) and find that the turning points of $c^{(1)}$ are solutions of a quintic equation in $\tanh(3\tilde{\sigma}_0^* \tilde{z})$, which will be referred as P_5 and is given below as,

$$P_5 = \left(\frac{D_S}{D_L} - 1 \right) \left[\tanh^5(3\tilde{\sigma}_0^* \tilde{z}) + \frac{\tilde{\nu}}{2} \tanh^4(3\tilde{\sigma}_0^* \tilde{z}) - 5 \tanh^3(3\tilde{\sigma}_0^* \tilde{z}) \right] \\ + \left[5 \left(\frac{D_S}{D_L} + 1 \right) + 3\tilde{\nu} \left(\frac{D_S}{D_L} - 1 \right) \right] \tanh^2(3\tilde{\sigma}_0^* \tilde{z}) \\ + \left[4\tilde{\nu} \left(\frac{D_S}{D_L} + 1 \right) - 3 \left(\frac{D_S}{D_L} - 1 \right) \right] \tanh(3\tilde{\sigma}_0^* \tilde{z}) \\ - \left(\frac{D_S}{D_L} + 1 \right) - \frac{3}{2} \tilde{\nu} \left(\frac{D_S}{D_L} - 1 \right). \quad (8.39)$$

(Note that, when $D_S/D_L = 1$, this equation is reduced to (8.13)). Therefore we expect $c^{(1)}$ to have at most five turning points, which are either local minimas or maximas. Again, for real values of \tilde{z}_{max} (or \tilde{z}_{min}), the modulus of $\tanh(3\tilde{\sigma}_0^* \tilde{z})$ has to be less than unity. In order to investigate the zeros of (8.39) in this range, we plot the polynomial against $\tanh(3\tilde{\sigma}_0^* \tilde{z})$ for different values of D_S/D_L . From the plots shown in Fig. 8.7, we can see that the trend we found in the case $D_S/D_L = 1$ is repeated for the case when $D_S/D_L < 1$, i.e., when $|\tilde{\nu}| < 1$, two zeros (corresponding to two turning points) exist and as $|\tilde{\nu}|$ becomes greater than unity, one of the turning point disappears. The single turning point that remains, is found to become more positive as D_S/D_L is reduced.

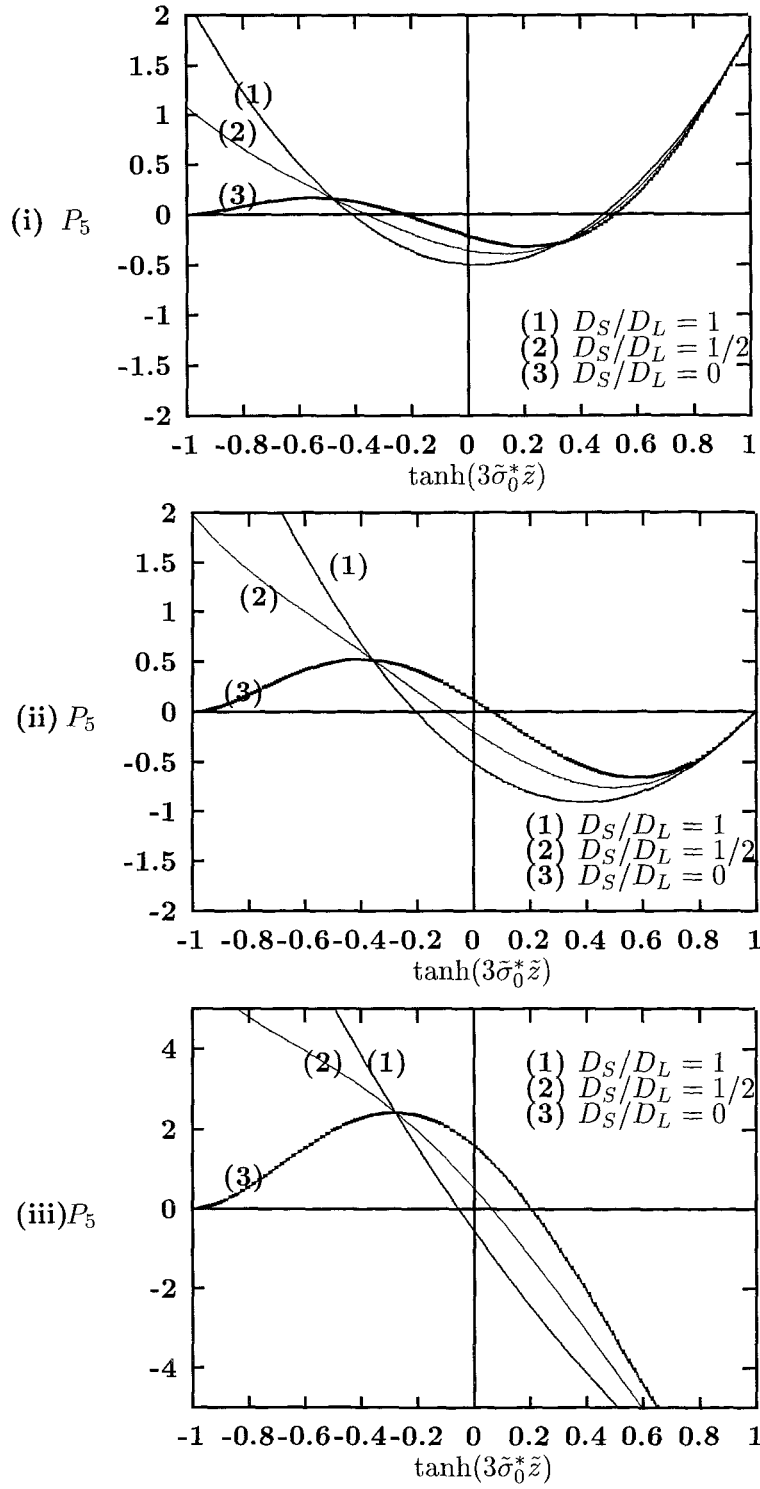


Figure 8.7: The polynomial P_5 plotted against $\tanh(3\tilde{\sigma}_0^* \tilde{z})$ for three different values of $\tilde{\nu}$, (i) $\tilde{\nu} = -0.1$, (ii) $\tilde{\nu} = -1.0$ and (iii) $\tilde{\nu} = -5.0$. Each plot consists of three curves representing the polynomials corresponding to different values of D_S/D_L .

We go on further to plot the profiles of $c^{(1)}$ for different values of D_S/D_L in Fig. (8.8(i)). The profiles confirm the observations we predicted above where we can see that the persistent turning point turns out to be a local maximum.

The profiles of c for increasing \tilde{V}_ϵ in Fig. 8.8(ii) showed that solute trapping persists for $D_S/D_L < 1$. The profiles are plotted using the Nickel-Copper alloy data with $\epsilon = 3.3 \times 10^{-6} \text{J}^{1/2} \text{cm}^{-1/2}$, where we see that for these values, the \tilde{z} -coordinate of c_{max} is shifted from $\tilde{z} = 0$ by a small value, say \bar{z} , i.e., $\tilde{z}_{max} = \bar{z}$ where \bar{z} satisfies (8.39). Expanding $\tanh(3\tilde{\sigma}_0^* \tilde{z}_{max})$ about $\tilde{z} = 0$ we have,

$$\tanh(3\tilde{\sigma}_0^* \tilde{z}) = 3\tilde{\sigma}_0^* \tilde{z} + \mathcal{O}(\tilde{z}^3),$$

which, after substituting in the homogeneous equation

$$P_5 = 0,$$

we can approximate \bar{z} as,

$$\bar{z} = \frac{\left[\frac{3}{2} \left(\frac{D_S/D_L - 1}{D_S/D_L + 1} \right) + \tilde{\nu}^{-1} \right]}{12\tilde{\sigma}_0^* \left[1 - \frac{3\tilde{\nu}^{-1}}{4} \left(\frac{D_S/D_L - 1}{D_S/D_L + 1} \right) \right]}. \quad (8.40)$$

For simplicity, we will restrict the remaining analysis to the case $|\tilde{\nu}|$ large, i.e., k_e is small and less than unity, in which case,

$$\bar{z} \approx \frac{1}{32\tilde{\sigma}_0^*} \left[4 \left(\frac{D_S/D_L - 1}{D_S/D_L + 1} \right) + \frac{8}{3} \tilde{\nu}^{-1} + 3 \left(\frac{D_S/D_L - 1}{D_S/D_L + 1} \right)^2 \tilde{\nu}^{-1} + \mathcal{O}(\tilde{\nu}^{-2}) \right]. \quad (8.41)$$

The approximate value for \bar{z} gives,

$$\begin{aligned} \tanh(3\tilde{\sigma}_0^* \bar{z}) &\approx 3\tilde{\sigma}_0^* \bar{z} \\ &= \frac{3}{32} \left\{ 4 \left(\frac{D_S/D_L - 1}{D_S/D_L + 1} \right) + \left[\frac{8}{3} + 3 \left(\frac{D_S/D_L - 1}{D_S/D_L + 1} \right)^2 \right] \tilde{\nu}^{-1} \right. \\ &\quad \left. + \mathcal{O}(\tilde{\nu}^{-2}) \right\}. \end{aligned} \quad (8.42)$$

Assuming $\tanh(3\tilde{\sigma}_0^* \bar{z})$ is small, where its estimate is given by the expression (8.42) above, an approximation for the maximum concentration $c_{max}^{(1)}$ can be found. This is,

$$\begin{aligned} c_{max}^{(1)} &= c^{(1)}(\bar{z}) \\ &= \frac{27}{4} c_\infty (1 - c_\infty) \tilde{\sigma}_0^* (\tilde{\sigma}_{B0}^2 - \tilde{\sigma}_{A0}^2) \left[\left(\frac{D_S}{D_L} + 1 \right) \tilde{\nu} + \left(\frac{D_S}{D_L} + 1 \right) \tanh(3\tilde{\sigma}_0^* \bar{z}) \right. \\ &\quad \left. - \frac{1}{2} \left(\frac{D_S}{D_L} - 1 \right) \tilde{\nu} \tanh(3\tilde{\sigma}_0^* \bar{z}) \right], \end{aligned} \quad (8.43)$$

where, we only retain the terms proportional to $\tanh(3\tilde{\sigma}_0^* \bar{z})$ and larger. After substituting for $\tanh(3\tilde{\sigma}_0^* \bar{z})$ in (8.43), we have

$$c_{max}^{(1)} = \frac{27}{4} c_\infty (1 - c_\infty) \tilde{\sigma}_0^* (\tilde{\sigma}_{B0}^2 - \tilde{\sigma}_{A0}^2) \tilde{\nu} \left[\left(\frac{D_S}{D_L} + 1 \right) - \frac{3}{16} \left(\frac{(D_S/D_L - 1)^2}{D_S/D_L + 1} \right) + \mathcal{O}(\tilde{\nu}^{-1}) \right]. \quad (8.44)$$

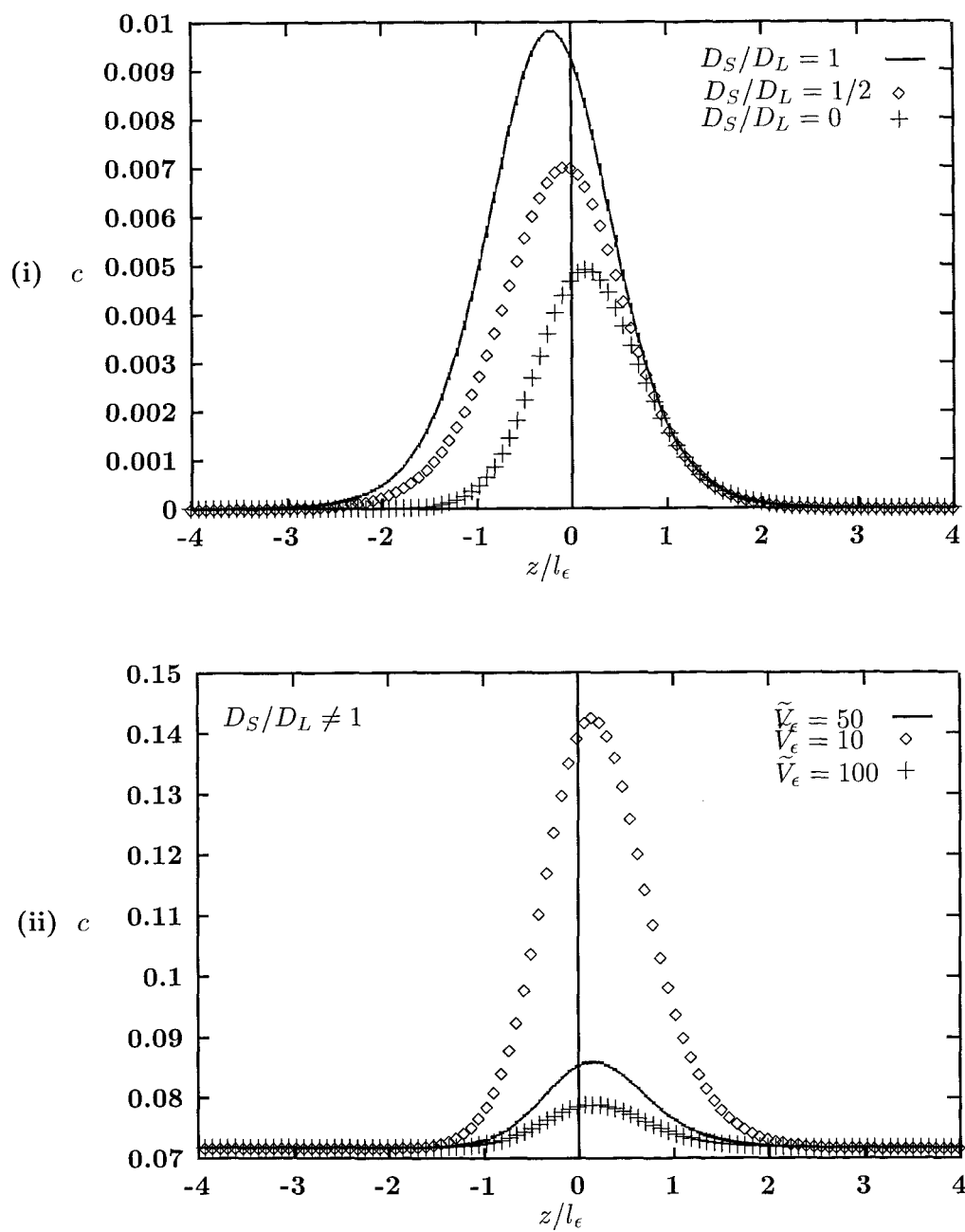


Figure 8.8: (i) The asymptotic solution for the solute field for different values of D_S/D_L . (ii) The profiles of the asymptotic solution for c when $D_S/D_L \neq 1$ exhibit solute trapping as \tilde{V}_ϵ increases.

The relationship (8.24) applies here for the partition coefficient, with $c_{max}^{(1)}$ given by (8.44), where we see the same trapping behaviour is produced.

8.2.2 Diffusive speed

We now look for an expression for the diffusive speed, V_D , by using the same method used in section (8.1.2). In the dilute limit, the form for $\frac{c_{max}^{(1)}}{c_\infty}$ is given below,

$$\left(\frac{c_{max}^{(1)}}{c_\infty}\right)^* = \frac{9}{8} \tilde{\sigma}_A \ln(1/k_e) \left[\left(\frac{D_S}{D_L} + 1\right) - \frac{3}{16} \left(\frac{(D_S/D_L - 1)^2}{D_S/D_L + 1}\right) + \mathcal{O}(\tilde{\nu}^{-1}) \right].$$

After substituting this expression into (8.27), and ignoring terms of $\mathcal{O}(\tilde{\nu}^{-1})$ and smaller, we obtain the following dimensional form for V_D ,

$$V_D = \frac{9}{8} \frac{\sigma_A D_L}{\epsilon^2} \frac{\ln(1/k_e)}{(1 - k_e)} \left[\left(\frac{D_S}{D_L} + 1\right) - \frac{3}{16} \left(\frac{(D_S/D_L - 1)^2}{D_S/D_L + 1}\right) \right]. \quad (8.45)$$

After substituting σ_A/ϵ^2 with $1/(6l_i)$, equation (8.45) becomes

$$V_D = \frac{3}{16} \frac{D_L}{l_i} \frac{\ln(1/k_e)}{(1 - k_e)} \left[\left(\frac{D_S}{D_L} + 1\right) - \frac{3}{16} \left(\frac{(D_S/D_L - 1)^2}{D_S/D_L + 1}\right) \right], \quad (8.46)$$

where (8.46) relates V_D directly to the material parameters of the alloy.

We now have a more realistic form for V_D , which exhibits the dependence of the diffusive speed on both the diffusivity in the solid bulk phase and the diffusivity in the liquid bulk phase. We note that, when both diffusion constants are equal, the expression reduces to (8.32). It is also interesting to note that, when the ratio $D_S/D_L \approx 0$, this final expression becomes,

$$V_D = \frac{39}{256} \frac{D_L}{l_i} \frac{\ln(1/k_e)}{(1 - k_e)}. \quad (8.47)$$

In order to see how well (8.47) approximates experimental data, we plot the $V_D - k_e$ data obtained from (8.47) and compare it with experimental values of V_D given in reference [4] (see Table 8.1). The form in (8.47) is plotted for four different values of the interface width l_i , $l_i = 3.46 \times 10^{-7}, 1 \times 10^{-7}, 6.2 \times 10^{-8}$ and 1.0×10^{-8} cm in Fig. 8.9. The first value of l_i is obtained by taking an average of the five different values of l_i that correspond to the experimental data in Table 8.1, where l_i is calculated using Aziz's approximation, which is $l_i \approx D_L/V_D$ and D_L is assumed to be $1.5 \times 10^{-4} \text{ cm}^2 \text{ s}^{-1}$ [54]. A physically reasonable value for l_i should be between 1×10^{-7} and 1×10^{-8} cm [70], the third value that we choose above is a more specific figure for l_i which was suggested by Kittl et. al. [54].

We see from Fig. 8.9 that a good agreement between (8.47) and experimental results is obtained when l_i is 6.2×10^{-8} , where the solid line represented by this value lies close to

<i>Alloy</i>	k_e	V_D (experiment)(m/s)
Si-Bi	0.0007	32
Si-In	0.004	57
Si-Ga	0.008	22
Si-Sn	0.016	17
Si-Ge	0.3	1.0

Table 8.1: A table of experimentally determined values of the diffusive speeds V_D and the corresponding equilibrium partition coefficient k_e for various Silicon-based alloys.

most of the experimental data (represented in the plot by dots). The plot **emphasizes the significance of the k_e dependence of V_D** . Furthermore, the fact that the asymptotic result and the experiment data agree best for a value of l_i which is within the physically reasonable range, **confirms the accuracy of our asymptotic approximation of V_D** .

Note that the basic hypothesis of CGM states that $V_D \approx D_i/\lambda$, where D_i is the diffusion coefficient across the interface and λ is the interatomic distance. The common approximation that $D_i \approx D_L$ and $\lambda \approx l_i$ is quite inaccurate as suggested by Cahn, Hillig and Sears [72]. Thus, Aziz's approximation of V_D should be corrected by some factor Π say, in order to account for the error in the approximations of D_i and λ . Our result suggests that this factor should be,

$$\Pi = \frac{3}{16} \frac{\ln(1/k_e)}{(1 - k_e)} \left[\left(\frac{D_S}{D_L} + 1 \right) - \frac{3}{16} \left(\frac{(D_S/D_L - 1)^2}{D_S/D_L + 1} \right) \right], \quad (8.48)$$

where it allows V_D to depend on k_e , capturing the correct dependence observed in experiments. It also shows how V_D relates to the ratio of the diffusion coefficients, namely D_S/D_L , which has not yet been determined successfully in experiments.

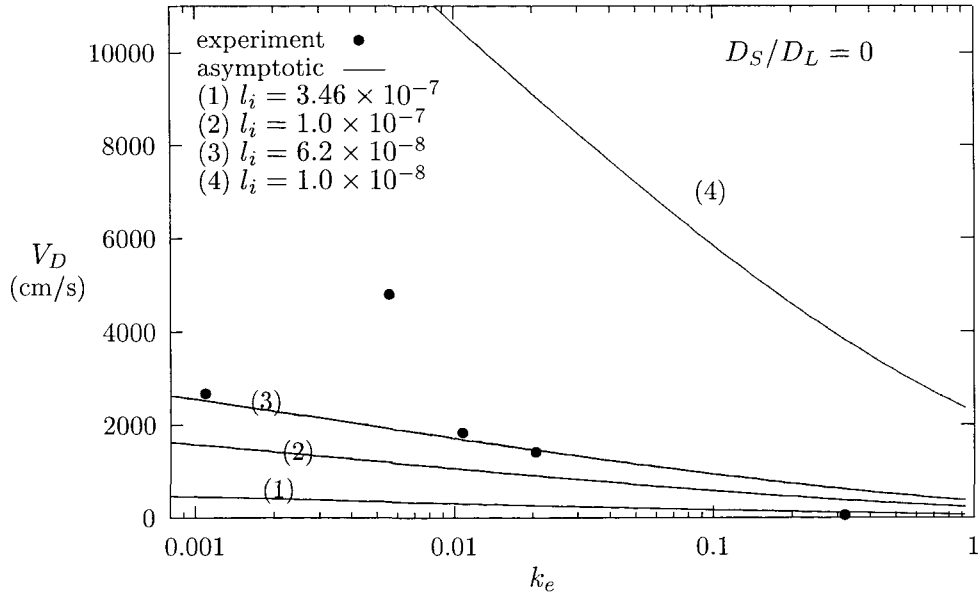


Figure 8.9: The values of the dimensional diffusive speed calculated from the functional form in (8.47) which corresponds to that of Silicon alloys are compared with the experimental values.

8.3 Comparing the asymptotic solutions with numerical solutions

The asymptotic analysis of the WBM2 model is one way of determining the reliability of the numerical calculations of the model. The results we have obtained so far are very encouraging, in that much of the behaviour of the solutions predicted in the numerical analysis is also observed in the asymptotic analysis. One important feature that was captured in the numerical calculation of the solute concentration is the trapping phenomena at high \tilde{V}_ϵ , which is independent of the solute gradient energy coefficient, δ . This behaviour is confirmed in the asymptotic analysis from the form of the partition coefficient k , which rises to one as \tilde{V}_ϵ increases, and, to first order of \tilde{V}_ϵ , k is independent of δ . Both analyses are also able to provide values for the diffusive speed V_D which show an inverse correlation with the equilibrium partition coefficient k_e , a trend that is also observed in experiments.

The agreements we have established between the two analyses are mostly qualitative. It is important to also obtain quantitative agreements in order to ascertain the range of values of \tilde{V}_ϵ for which the asymptotic approximations are valid. Such information can be acquired by comparing the numerical solutions with the regular expansions for ϕ , c and k in \tilde{V}_ϵ^{-1} .

A comparison of the solutions from the asymptotic and numerical calculations is shown in Fig. 8.10 and Fig. 8.11, where, they are observed to agree quantitatively. They contain the profiles of c and ϕ respectively, from the two calculations. An increasingly good agreement is observed for the c profiles in Fig. 8.10 between the asymptotic and the numerical solutions as \tilde{V}_ϵ gets large. The agreement is observed for both case $D_S/D_L = 1$ and $D_S/D_L = 0$. The ϕ profiles for both calculations are observed to be almost exactly the same, and this is found for all values of \tilde{V}_ϵ .

The partition coefficients are given in Fig. 8.13 (shown here as a plot of $\ln(1 - k)$ against $\ln(\tilde{V}_\epsilon)$) to determine how similar the solute trapping measurements are between the two calculations. The numerical values of k are observed to approach the solid line representing its asymptotic approximation, as \tilde{V}_ϵ gets large. A good quantitative agreement is obtained for $\tilde{V}_\epsilon > 30$ (equivalent to $V > 40\text{m/s}$). Although the asymptotic solution for c fails to capture the more detailed feature of the solute profile (see Fig. 8.10), for example, the small oscillatory behaviour of the solution near $\tilde{z} = 0$, it does not affect the maximum value of the concentration, which results in a good quantitative agreement between the values of k for the two calculations in the large \tilde{V}_ϵ range.

We have also compared, in Fig 8.12, the $V_D - k_e$ data of the Nickel based alloys with the values calculated from (8.47), where we have assumed l_i to be $4.9 \times 10^{-8}\text{cm}$. Both calculations produce values of V_D with the same qualitative behaviour with respect to k_e , where it decreases as k_e increases to unity. A better quantitative agreement is achieved between the two sets of results when $0.1 < k_e < 1$, which is the range where the numerical code performs at its best. This is also the range where the k_e value is approaching the value corresponding to the Nickel-Copper alloy. Because the numerical calculations of V_D are performed using artificial data for the alloys, we expect the results to be more reliable as k_e approaches the value corresponding to the real alloy.

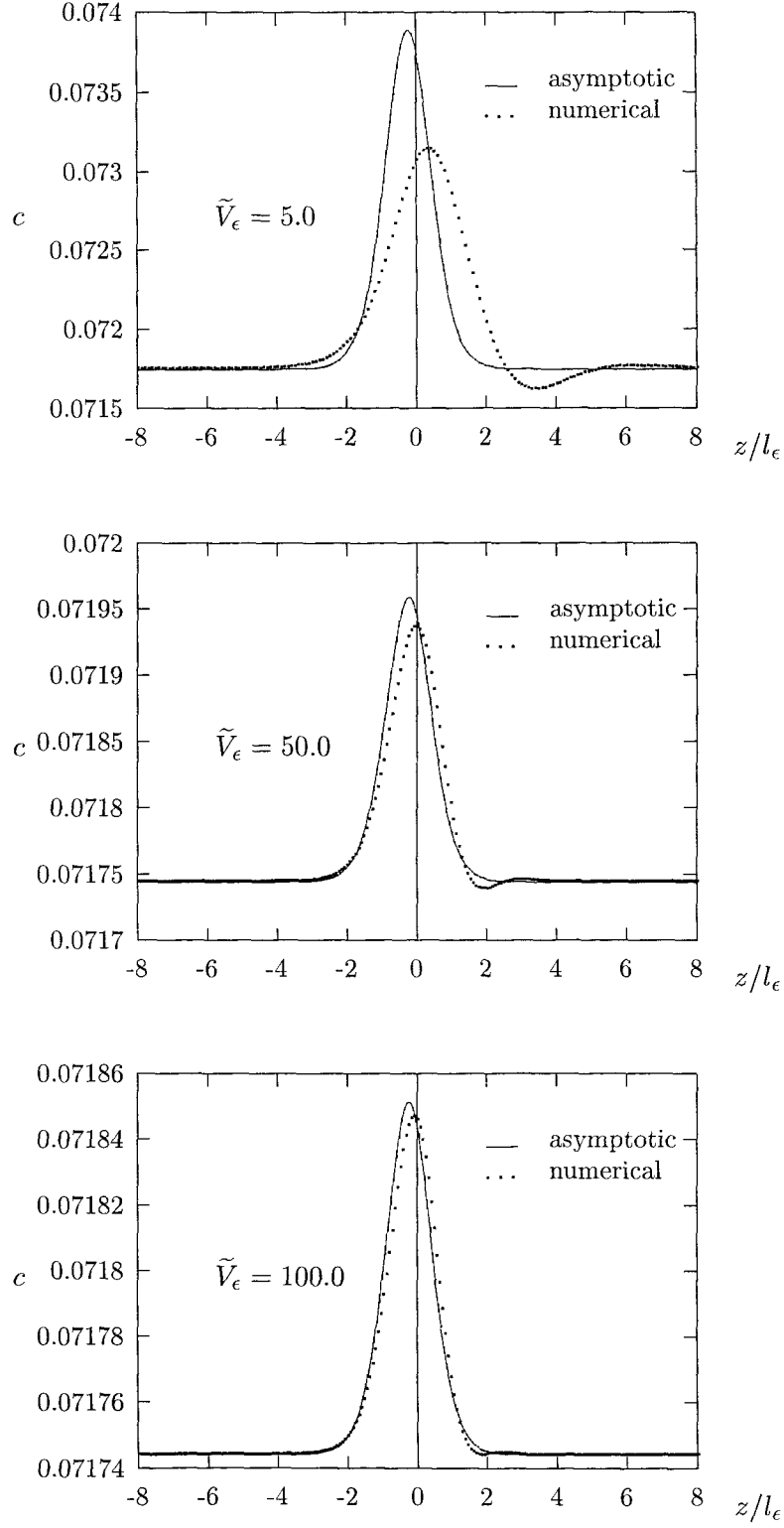


Figure 8.10: The asymptotic solutions for c are compared with the numerical solutions for three different values of \tilde{V}_ϵ . The solutions above are computed for $D_S/D_L = 1$, the result is similar for the case $D_S/D_L = 0$.

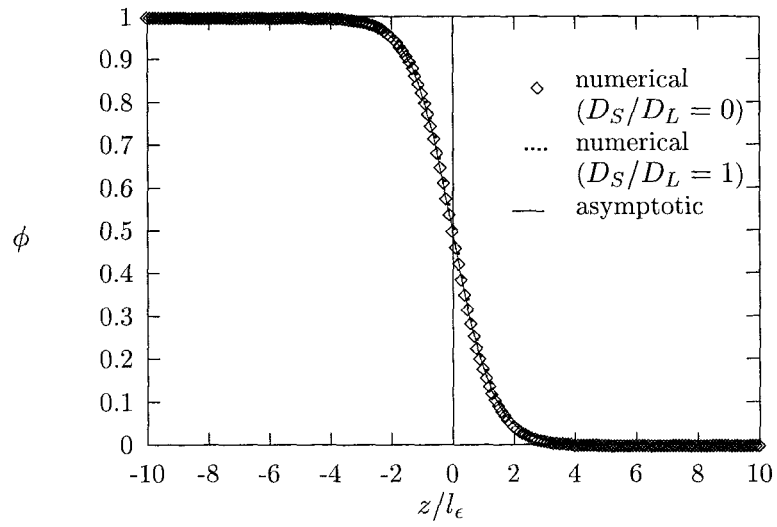


Figure 8.11: The asymptotic phase-field profile compared with the corresponding numerical profile for the two cases $D_S/D_L = 1$ and $D_S/D_L = 0$.

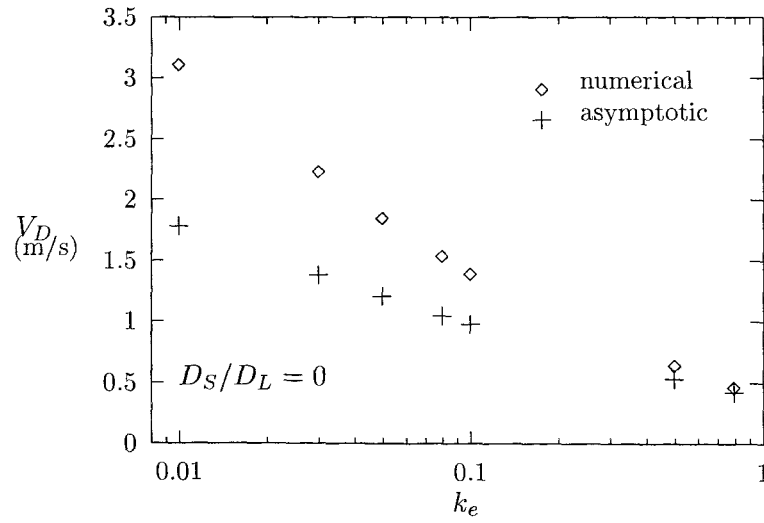


Figure 8.12: The asymptotic approximation for V_D for the Nickel-based alloy, plotted against the corresponding numerical values. The interface thickness is assumed to be 4.9×10^{-8} cm.

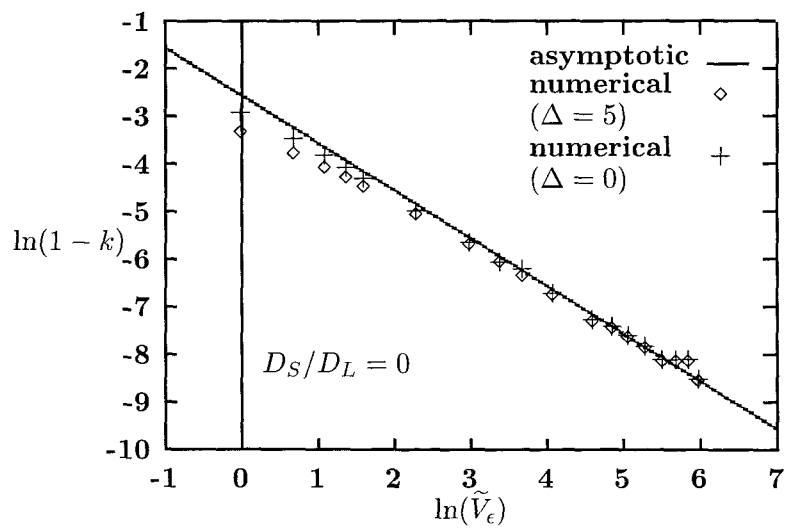
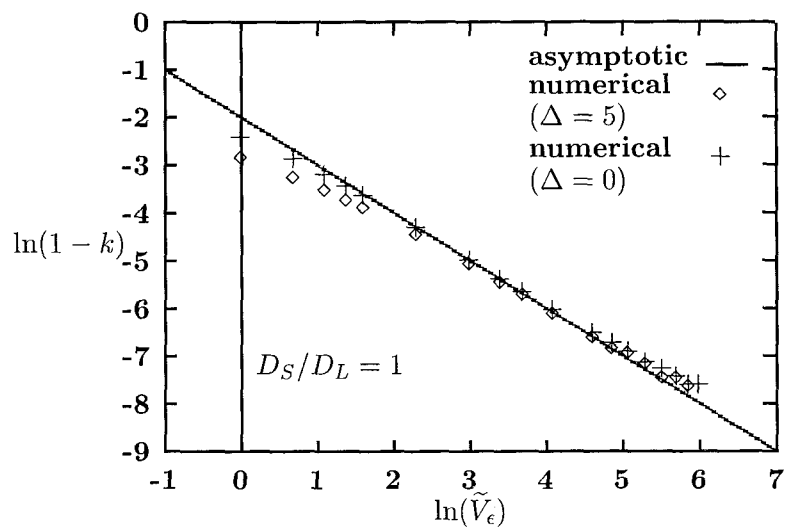


Figure 8.13: The asymptotic form for $\ln(1-k)$ (plotted against $\ln(\tilde{V}_\epsilon)$) is compared with the corresponding numerical values for $D_S/D_L = 1$ and $D_S/D_L = 0$.



8.4 The relationship between Continuous Growth Model and the WBM model

The numerical and the asymptotic analyses of the WBM2 model have both successfully provided predictions of the solute trapping phenomenon. We have also seen numerous similarities between the trapping behaviour predicted by WBM2 model and that of the CGM (see Fig. 7.9). Moreover, when the high \tilde{V}_e expansions of the partition coefficient from the two models are compared, we were able to extract a functional form for the diffusive speed V_D which depends on the equilibrium segregation k_e in the same way as predicted in experiments. These results provide strong indications that the two models share the same physical features.

The WBM2 model describes the solid-liquid interface as a thin transition layer with a finite thickness. This description fits that of a diffuse interface which we have described in chapter 2. This particular type of interface favors a continuous transition from the liquid to solid due to the continuous change in the thermodynamic properties of the layers of atoms within the interfacial zone [5]. It is therefore reasonable to expect the growth mechanism of the alloy modelled by WBM2, to resemble that of a continuous growth. Inevitably, some, if not all of the ensuing phenomena, characterised by a continuous growth should be predicted by the model. Thus we may expect a similarity between the predictions of solute trapping in WBM2 model and that of the CGM. The similarities can be seen more clearly in the definition of the interdiffusion flux of the two models.

In CGM, the interdiffusion flux, J_D , is defined as the difference between the forward flux of solute, i.e., the flux of solute from the liquid into the solid, and the reverse flux, i.e, the flux of solute from the solid back into the liquid. Therefore, adopting the same notation as in Chapter 4, we have,

$$\begin{aligned} J_D &= J_{S \rightarrow L} - J_{L \rightarrow S}, \\ &= [D_i/\lambda][c_S(1 - c_L) - \kappa_e c_L(1 - c_S)], \end{aligned} \quad (8.49)$$

where, λ is the interatomic distance and $\kappa_e = \exp[-(\Delta\mu'_B - \Delta\mu'_A)/RT]$. The chemical potentials $\Delta\mu'_A$ and $\Delta\mu'_B$, the interface diffusion D_i and other constants are defined in chapter 4. Assuming the exponent in the definition of κ_e is small, and for dilute alloys we can find a c^* such that $c^*(1 - c^*)(1 - \kappa_e) \approx c_S(1 - c_L) - \kappa_e c_L(1 - c_S)$, (8.49) can be approximated as,

$$J_D = \frac{D_i}{\lambda} c^*(1 - c^*)(\Delta\mu'_B - \Delta\mu'_A)/RT. \quad (8.50)$$

The conservation of solute in the system gives rise to the following equation,

$$\frac{\partial c}{\partial t} = \frac{(J_{L \rightarrow S} - J_{S \rightarrow L})}{\lambda} = -\frac{J_D}{\lambda}. \quad (8.51)$$

In the WBM2 model, the conservation of solute is achieved by postulating the following equation for the solute field,

$$\frac{\partial c}{\partial t} = \nabla \cdot \left[M_2 \left(c(1-c) \nabla \frac{\delta \mathcal{F}}{\delta c} \right) \right], \quad (8.52)$$

where M_2 is related to the diffusion coefficient by $D = M_2 RT/v_m$, and the free energy functional \mathcal{F} is defined by equation (3.1). In this model, the interdiffusion flux is proportional to the term $\nabla(\delta \mathcal{F}/\delta c)$ [1]. This term is identically equal to ∇f_c (assuming $\delta = 0$), which is the gradient of chemical potential of the alloy. In 1-D, (8.52) becomes

$$\frac{\partial c}{\partial t} = \frac{d}{dz} \left[M_2 \left(c(1-c) \nabla \frac{\delta \mathcal{F}}{\delta c} \right) \right]. \quad (8.53)$$

Comparing (8.51) and (8.53), we are able to identify the interdiffusion flux of the WBM2 model as,

$$J_D^* = -M_2 \left(c(1-c) \nabla \frac{\delta \mathcal{F}}{\delta c} \right) = \frac{Dv_m}{RT} \left[c(1-c) \nabla \frac{\delta \mathcal{F}}{\delta c} \right], \quad (8.54)$$

for one dimensional steady state fluxes.

Now, across a sharp interface, ∇f_c can be approximated as,

$$\nabla f_c \approx \frac{1}{\lambda} \left([f_B]_L^S - [f_A]_L^S \right) + E', \quad (8.55)$$

where E' is a constant and,

$$[f_A]_L^S = f_A(\text{solid}) - f_A(\text{liquid}).$$

The quantity f_A and f_B are the actual chemical potentials of A and B respectively, minus the contribution from the ideal mixing entropy. This is in fact the exact definition of μ'_A and μ'_B , i.e., $f_A = \mu'_A$ and $f_B = \mu'_B$, which gives,

$$[f_A]_L^S = \nabla \mu'_A, \quad (8.56)$$

$$[f_B]_L^S = \nabla \mu'_B. \quad (8.57)$$

On substituting (8.56) and (8.57) into (8.55), we obtain the following approximation for (8.54),

$$J_D^* \approx \frac{Dv_m}{\lambda} [c(1-c)(\nabla \mu'_B - \nabla \mu'_A)/RT] + E \quad (8.58)$$

$$\approx J_D + E, \quad (8.59)$$

where $E = \frac{Dv_m}{\lambda} c(1-c)E'$.

So we see that J_D^* is almost identical to J_D if $E \equiv 0$. The constant E depends on the concentration c , which, if we recall the nondimensionalisation of the governing equation we did earlier, this term is equal to $dc/d\tilde{z}$ (see governing equation (7.6)). In the limit $\tilde{V}_\epsilon \rightarrow \infty$, this term is found to appear in the first order equation as $dc^{(0)}/d\tilde{z}$, but because the leading order concentration is a constant, this term is identically zero. Therefore, in the limit the interface velocity $V \rightarrow \infty$, we deduce that

$$J_D^* = J_D. \quad (8.60)$$

In sections 7.1.2 and 7.2.2, we made an important assumption that the high velocity limit of the partition coefficient k from CGM is identically equal to the asymptotic expansion of k in the high \tilde{V}_ϵ limit from the WBM2 model. The relationship given by (8.60) offers a justification for this assumption. The interdiffusion flux determines the amount of solute atoms that successfully escape the advancing solid front. Indirectly, for a particular interface velocity, it offers a measure of the solute atoms that are trapped in the solid. Thus, it determines the extent of trapping at that velocity. The fact that the interdiffusion fluxes from the two models are almost identically equal in the high interface velocity limit (8.60), suggests that their forms for the partition coefficient are also equal.

Notice that the interdiffusion flux is dependent on the free energy density function $f(\phi, c)$. It may be possible to obtain a similar relationship between CGM and other phase-field models that adopt a different choice of $f(\phi, c)$, by conducting a similar investigation as above.

Chapter 9

Summary and future work

The analyses carried out in the previous chapters have dealt with a variety of aspects of the rapid solidification process, specifically the mechanisms that govern solute trapping. The results we obtained have explained several issues regarding the process, that have arisen in previous works on the subject. They also offer improvements to previous results which, in general, contribute to a further understanding of the process.

In this concluding chapter, we produce a summary of the results and discuss their significance in the development of the theories of rapid solidification. We also discuss a number of areas where the analysis can be extended and improved.

9.1 Summary and discussion of the results on solute trapping

In this section, we present the summary of the results obtained on solute trapping. Each result is outlined and discussed separately below.

9.1.1 The independence of solute trapping on δ

In their first model for the solidification of a binary alloy [1], Wheeler et. al. recovered a corresponding sharp interface problem in the limit of the ratio $l_\epsilon = \epsilon\sqrt{v_m/RT}$ to D/V , tends to zero, which failed to capture the solute trapping phenomenon. They modified this model in [2] by adding the gradient energy term for the solute field in the free energy functional. In a similar limit $\tilde{\epsilon} = l_\epsilon/l_\delta \rightarrow 0$ (with the solute gradient energy coefficient, δ , constant), where $l_\delta = \delta\sqrt{v_m/RT}$, solute trapping was predicted for large solidification velocities. However, it is not clear from this new model, whether the observed solute trapping behaviour is due to the solute energy gradient, or whether it is an outcome of the particular distinguished limit they considered.

In both the numerical and asymptotic analyses, we determined that the solute gradient energy term is **not needed** for solute trapping. The numerical profiles of the solute fields, computed with $\delta = 0$, show a marked decrease in the maximum concentration of solute as the velocity is increased, i.e., solute trapping. A similar observation is found with the asymptotic solution for the solute field in the high \tilde{V}_ϵ limit, where the first two terms in the expansions are independent of δ .

The result above is obtained from both analyses by considering the limit $\tilde{V}_\epsilon \rightarrow \infty$ with $\Delta = \delta/\epsilon$ fixed, where $\tilde{V}_\epsilon = Vl_\epsilon/D = l_\epsilon/(D/V)$. This corresponds to allowing the diffusive length scale associated with the solute field, namely D/V , to be smaller than the length with which the velocity is scaled, denoted by l_ϵ , for large V . This is precluded in the original model [1] because the limit $l_\epsilon/(D/V) \rightarrow 0$, with the interface velocity, V fixed, implies D/V is large compared to l_ϵ . In the second WBM model [2], the non-dimensional interface velocity is scaled as $\tilde{V}_\delta = l_\delta/(D/V)$, where l_δ is identified as the characteristic length scale of the solute field. The limit $l_\epsilon/l_\delta \rightarrow 0$ in this case, is taken independent of the interface velocity. As a result, trapping of solute is observed when \tilde{V}_δ is not small. Therefore, we identify the trapping phenomena as a result of D/V being **comparable** or **smaller** than the characteristic length scales of either the phase-field, or the solute field. Now, in the case when $\delta = 0$, the only interfacial length scale is l_ϵ and so trapping occurs when $\tilde{V}_\epsilon = l_\epsilon/[D/V]$ is not small.

Both of these lengths are shown in the analysis (see section 7.4) to be proportional to the characteristic thickness of the interface, i.e., l_i , thus **solute trapping can be said to occur when the physical length scale of the solute field is comparable or smaller than the interface width**. This proved to be an advantage of the WBM2 model (a phase-field model) over Aziz's solute trapping models, which are sharp interface models. Because the phase-field model allows the solid-liquid interface to have a measurable thickness, we are able to form a direct relationship between, the relative sizes of the diffusive length scale D/V and the interface thickness, and the solute trapping process. Naturally, a concern arises when applying continuum models to a description of the length scale associated with the interface width, which is comparable to atomic dimensions. We have not addressed this issue here.

9.1.2 The partition coefficient

In our analyses, the partition coefficient, which is the parameter used as a measure for solute trapping, is defined by the following equation,

$$k = \frac{\text{far - field concentration}}{\text{the maximum concentration of solute}}.$$

The dependence of k on the interface velocity as observed in experiments, is well captured numerically and asymptotically. The numerical values of k are shown to increase from its equilibrium value k_e (whenever $k_e < 1$) to unity, as the interface velocity increases. The asymptotic representation of k also shows an increase to unity as $\tilde{V}_\epsilon \rightarrow \infty$ (whenever $k_e < 1$).

The quantitative dependence of k on the velocity is shown in the numerical analysis (see Fig. 7.9) to be closely approximated by the form of k given by CGM, i.e.,

$$k = \frac{k_e + V/V_D}{1 + V/V_D}.$$

The similarity has allowed us to extract values for the diffusive speed V_D from the numerical values of k using least squares fitting. We also managed to obtain an explicit form for V_D from the comparison of the asymptotic expansion for k and the CGM, in the high interface velocity limit.

9.1.3 Correlation between the diffusive speed and the material parameters

The values for the diffusive speed are obtained numerically using the procedure mentioned earlier, for a number of different material parameters of the alloy. These are the equilibrium partition coefficient k_e , the diffusivity ratio, D_S/D_L , and the interface width, l_i . The correlation between the numerical values of V_D and two of the parameters (k_e and l_i) agree with experimental observations, where we find V_D to be inversely correlated with both, k_e and l_i . We also observed that V_D is directly proportional to D_S/D_L .

These results are later confirmed by the explicit functional form obtained for V_D in the asymptotic analysis. This form is given by,

$$V_D = \frac{3}{16} \frac{D_L}{l_i} \frac{\ln(1/k_e)}{(1 - k_e)} \left\{ \left[\frac{D_S}{D_L} + 1 \right] - \frac{3}{16} \left[\frac{(D_S/D_L - 1)^2}{D_S/D_L + 1} \right] \right\}, \quad (9.1)$$

where it differs from the conventional approximation for V_D , i.e., D_L/l_i by a factor of Π , where Π is given by,

$$\Pi = \frac{3}{16} \frac{\ln(1/k_e)}{(1 - k_e)} \left\{ \left[\frac{D_S}{D_L} + 1 \right] - \frac{3}{16} \left[\frac{(D_S/D_L - 1)^2}{D_S/D_L + 1} \right] \right\}.$$

The quantity Π is identified as a factor to correct the assumptions made in the conventional approximation, that $D_i \approx D_L$ and $\lambda \approx l_i$, where D_i and λ are the interface diffusivity and the interatomic distance respectively.

In the expression for V_D above, the interface width l_i appears as a parameter, thus, in order to compare the explicit form for V_D with experimental results, a specific value for the interface width had to be chosen. This is resolved by plotting the asymptotic form corresponding to several different, physically plausible values of l_i , against the experimental data. For the

Silicon alloys in Table 8.1, we found the experimental V_D data are best approximated by the asymptotic approximation that corresponds to $l_i = 6.2 \times 10^{-8}$ cm. This value is within the proposed range of reasonable values for the interface width of Silicon [54, 70].

The explicit expression for V_D provides an estimate for its value which is useful in predicting microstructural development in solidification [71]. Our estimate is clearly an improvement to the conventional method, in that the **interface width is the same for all the Silicon alloys**, which is expected in this case as all the alloys are dilute. In the conventional method however, because the interface width is inferred from the equation $l_i = D_L/V_D$, its value was found to be different for all the Silicon alloys in Table 8.1. Its value varies by over an order of magnitude, which is quite unacceptable [4, 71].

Another advantage of the form we derived above is that it **relates V_D to the readily measurable quantities of the solvent** (in this case, Silicon). This provides a means of estimating the value of the parameter V_D for alloy systems in which the value cannot be measured. None of the solute trapping models to date is capable in providing a direct relationship between V_D and the material parameters. The only experimental result that has been able to predict an inverse correlation between V_D and the equilibrium partition coefficient, k_e , is due to Smith et. al. [4]. The expression we obtained in (9.1), extends their prediction by providing a more specific dependence of V_D on k_e , where the values calculated using the functional (9.1) are shown to agree **both qualitatively and quantitatively** with the results of Smith et. al. Furthermore, the functional form gives a direct relationship between V_D with the diffusivities in the bulk phases, i.e., D_S and D_L . Experimental analyses carried out by Smith et. al. [4] were unable to predict any correlation between V_D and either of these parameters.

9.1.4 The cases $k_e > 1$ and $\tilde{V}_\epsilon < 0$

The analyses we did in section 8.1.3 shows that solute trapping is also observed for the cases $k_e > 1$ and $\tilde{V}_\epsilon < 0$. The resulting form for V_D shows exactly the same trend with k_e and other material parameters as in the previous case. The similarity in the results suggest that there exists some symmetry between the trapping behaviour of solute in cases with $k_e < 1$ and $k_e > 1$, and in the cases $\tilde{V}_\epsilon > 0$ (solidification) and $\tilde{V}_\epsilon < 0$ (melting). Obviously, more analysis needs to be done to determine the limits in which the symmetric relationship is valid.

9.1.5 The relationship between phase-field models and the CGM

In section 8.4, we have shown that in the dilute limit of the alloy, the interdiffusion fluxes from the two models are in fact almost exactly equal. Because the interdiffusion flux determines the extent of trapping, this result implies that the partition coefficient is also equal in this limit. Consequently, this observation validates the earlier assumption that

$$\lim_{\tilde{V}_\epsilon \rightarrow \infty} k(\text{asymptotic}) = \lim_{V/V_D \rightarrow \infty} k(\text{CGM}). \quad (9.2)$$

It is perhaps not surprising that (9.2) is true because we have already observed an overwhelming similarity between the solute trapping calculations of WBM2 model in the numerical analysis, and the trapping behaviour described in CGM. Moreover, the explicit form for V_D derived at the end of the asymptotic analysis shows all the expected features predicted in experiments (where the V_D values are obtained from the least squares fitting of the CGM to the experimental data).

9.2 Kinetic undercooling effect

In rapid solidification, the interface temperature is commonly observed to decrease beyond the normal melting point of the material. This reduction in the temperature is ascribed to the kinetic undercooling effect. The effect is successfully captured by the WBM2 model as we have shown in sections 7.6 and 8.1. The numerical calculations of the temperature are compared with the corresponding sharp interface predictions where very good agreement is found. The kinetic undercooling is featured in the asymptotic analysis of the model, as a first order term in the high \tilde{V}_ϵ expansion.

In the sharp interface limit of the WBM2 model with a curved interface, carried out in chapter 5, the kinetic undercooling term is obtained as part of the equation for the interface temperature. This expression led to a direct relationship between the phase-field parameter \tilde{m} , which is the non-dimensional representation of the mobility of the phase-field, to the dimensional interface attachment kinetic of the solvent μ_A , and other materials parameters of A. This relationship is given by,

$$\tilde{m} = \frac{\mu_A \sigma_A T_M^A}{L_A D},$$

where σ_A , L_A and T_M^A are the surface tension, latent heat and melting temperature of the solvent A respectively, and D is the diffusion coefficient. In the studies of non-equilibrium solidification, the kinetic undercooling term is commonly expressed as a term inversely proportional to \tilde{m} .

Because the treatment of solute trapping is carried out using the Nickel-Copper alloy, where the value of \tilde{m} is relatively large compared to the non-dimensional velocity \tilde{V}_ϵ , the kinetic undercooling term (which is proportional to $\tilde{V}_\epsilon/\tilde{m}$) is neglected in the asymptotic analysis, and the interface temperature is assumed constant. The addition of the term will involve a small change in the leading order solution of the solute field, subsequently, a small change in the solute trapping results is also expected.

9.3 Future work

Because of the limited studies on rapid solidification using the phase-field model, there is a lot of scope for further development of this area of research. The topics we propose below are just a few of the possible areas that could be explored, and further expansions of the analyses can be made.

9.3.1 The stability of the planar interface during rapid solidification

The sharp interface limit of the curved interface model in chapter 5 provides a starting point for further analyses on the stability of the planar interface during rapid solidification. This involves an investigation in the ensuing so-called morphological stability. The work can be built on the work of Mullins and Sekerka [10] (for a sharp interface model of a binary alloy), and Braun, McFadden and Coriell [73] (for a phase-field model of a pure material).

Unlike the present isothermal phase-field model of a binary alloy, morphological instability takes place in a temperature gradient and may result from undercooled liquid adjacent to the interface. Therefore the WBM2 model may need to be extended to the non-isothermal situation. A thermodynamically consistent phase-field model is based upon an entropy functional [28], a methodology that can be extended to an alloy. Alternatively, a simpler heuristic method may be adopted, that is to append a modified heat equation of the form

$$\rho c_p \frac{\partial T}{\partial t} = \gamma \nabla^2 T - L \frac{\partial \phi}{\partial t},$$

where c_p is the heat capacity, γ is the thermal conductivity and ρ is the density of the alloy.

9.3.2 Solute trapping treatments using curved interface and regular solution formulations of the WBM2 model

The extension of our analyses on the rapid solidification process to the formulations suggested in chapters 5 and 6, which accounts for a curved interface and the regular solutions, is quite

straightforward. The only addition to the formulations are the two parameters \mathcal{K} and G which correspond to the interface curvature and the energy of pair-wise interaction of the solute atoms. These are the quantities that represent the physical effects included in the formulation. The study of the effects of these additional parameters on the analyses will throw more light on the mechanisms of rapid solidification in more general circumstances.

Specifically, we could examine the dependence of the partition coefficient and the diffusive speed on G , and the possibility of deriving a suitable form for the diffusive speed, V_D , in terms of the equilibrium partition coefficient, k_e , in the limit $k_e \rightarrow 1$. We have shown in chapter 8 that the ideal solution phase-field model is incapable of determining the values of V_D for this range of k_e values (see section 8.1.2).

9.3.3 The interface diffusivity

In Aziz's sharp interface theories, the interface diffusivity D_i is the main factor that determines the value of the diffusive speed. The basic hypothesis of CGM states that D_i is related to the diffusive speed through the equation

$$V_D = \frac{D_i}{\lambda},$$

where λ is the inter-atomic distance. It has not been possible to measure D_i directly through experiments, therefore it is common practice to estimate its value by D_L , the diffusivity of the bulk liquid [4]. The explicit form we obtained for V_D has allowed us to provide a correction to this estimate, which gives the following new estimate for D_i ,

$$D_i = \frac{\Pi D_L \lambda}{l_i}, \quad (9.3)$$

where all the parameters are described in section 8.2.2.

However, in our current analyses, we included the effect of varying the diffusivity across the interfacial region, by insisting that the diffusivity D to be a function of ϕ . The form for D in this case is given by,

$$D(\phi) = (D_S - D_L)\phi^2(3 - 2\phi) + D_L,$$

where D_S and D_L are the diffusion coefficients in the solid and liquid bulk phases respectively. This particular choice of $D(\phi)$ satisfies the conditions $D = D_S$, $dD/d\phi = 0$ when $\phi = 1$ and $dD/d\phi = 0$ when $\phi = 0$, and it is monotonic in ϕ . It is therefore possible to relate D_i given in (9.3), to some average of $D(\phi)$ over the interfacial region [70], for example,

$$D_i \approx \int_{\phi \text{ where } c=c_{+\infty}}^{\phi \text{ where } c=c_{max}} D(\phi) d\phi. \quad (9.4)$$

The feasibility of equation (9.4) has not yet been verified. However, it offers a starting point from which the idea may be expanded. Success in this direction could provide a rationalisation of the relationship between the phase-field model and the microscopic properties of the interface.

9.3.4 Solute trapping treatments using other phase-field models

It would be possible to generalise the results of our analysis to other phase-field models that adopt a different form of the free energy density function. This supposition can be confirmed by carrying out the analyses on, for example, the phase-field model of Caginalp [12] (extended to binary alloys). His choice of the free energy density function is the following Helmholtz free energy density (for pure materials),

$$f(\phi, T) = \frac{1}{8a}(\phi^2 - 1)^2 - 2T\phi, \quad (9.5)$$

where a is a dimensionless constant. Notice that this form is similar to the free energy density suggested by Kobayashi, in that it comprises two parts, the symmetric part (the first term in (9.5) which has the symmetric double-well form), and an asymmetric part (the term proportional to temperature).

9.4 Conclusion

The analyses carried out in this thesis have produced numerous insights into the rapid solidification process and, more specifically, the solute trapping phenomenon. Not only have we managed to use the WBM2 model to predict the trapping behaviour that agrees with experimental observations, we also succeeded in producing the numerical values for the partition coefficient which displays solute trapping phenomena. Moreover, the functional form we have obtained for the diffusive speed, provides an exact dependence of the diffusive speed on material parameters like the equilibrium partition coefficient, the diffusivity ratio and the interface width of the alloy. This is the first solute trapping theory that is able to produce such an explicit relationship. It extends an earlier theory of Aziz, which predicts an inverse correlation between the diffusive speed and the equilibrium partition coefficient. A lack of experimental data for the diffusive speed means this finding is very important as it will help to predict the values for the diffusive speed of alloys where experimental data is not available.

Our analyses have managed to resolve an important issue that arose in an earlier work by Wheeler, Boettinger and McFadden [1, 2], since our numerical results shows that solute

trapping captured by the WBM2 model is not a result of the inclusion of the solute gradient energy term in the free energy functional of the model. Instead, it is found to result from the diffusive length scale of the solute field becoming comparable to the thickness of the interface, when the interface velocity is sufficiently large. This issue brings us to the problem of applying a continuum model at length scales comparable to atomic dimensions. Further studies are required to ascertain the possible effects such description of the length scale might have on solute trapping.

Having found some evidence that the solute trapping behaviour modelled by the CGM is equivalent to the behaviour predicted by the WBM2 model, we are in the position to make the same generalisation to other types of phase-field models. A further generalisation to consider, is to extend the result to the ‘thermodynamically consistent’ phase-field models in which an entropy functional is adopted.

We have produced several different formulations of the WBM2 model to include a curved solid-liquid interface, and the consideration of regular solutions in the solid-liquid transformation. These formulations should provide suitable models to assist further work on solute trapping.

Another important physical effect successfully observed in the analyses is the kinetic undercooling effect. This effect is one of the main characteristics of rapid solidification processes. An extension of the current model to the non-isothermal process will be needed in order to analyse the effect in greater detail.

Appendix A

Transforming the cartesian coordinates into the curvilinear coordinates

In the new coordinates (r, s) , the tangent vector and the normal vector to the point $(X(s, t), Y(s, t))$ on the curve $\phi = 1/2$ are (X', Y') and $(Y', -X')$ respectively, and the normal velocity is $V_n = Y'X_t - X'Y_t$, where the prime denotes the derivative with respect to arclength and time derivative is denoted by the subscript t . Therefore, the Cartesian coordinates are transformed into the new coordinate as follows (see Figure 5.1),

$$x(r, s, t) = X(s, t) + rY'(s, t), \quad (\text{A.1})$$

$$y(r, s, t) = Y(s, t) - rX'(s, t), \quad (\text{A.2})$$

and hence,

$$x_r = Y'(s, t), \quad (\text{A.3})$$

$$y_r = -X'(s, t), \quad (\text{A.4})$$

$$x_s = X'(s, t) + rY''(s, t), \quad (\text{A.5})$$

$$y_s = Y'(s, t) - rX''(s, t). \quad (\text{A.6})$$

Following McFadden et. al. [34], the local curvature to the interface is given by

$$K = X'Y'' - Y'X'', \quad (\text{A.7})$$

so that the Jacobian is given by,

$$h(r, s) = \det \begin{pmatrix} x_r & y_r \\ x_s & y_s \end{pmatrix}$$

$$= x_r y_s - x_s y_r \quad (\text{A.8})$$

$$= 1 + r K(s). \quad (\text{A.9})$$

Having obtained an expression for the local curvature K , we can now derive an expression for the square of the element of the differential arclength for the orthogonal coordinates (r, s) . This is given by

$$dS^2 = dr^2 + h^2 ds^2, \quad (\text{A.10})$$

thus, if we denote $g_{\alpha\beta}$ to be the metric tensor of the (r, s) coordinate system, then we have

$$g_{\alpha\beta} = \begin{pmatrix} 1 & 0 \\ 0 & h^2 \end{pmatrix} \quad (\text{A.11})$$

as,

$$dS^2 = g_{\alpha\beta} dx^\alpha dx^\beta, \quad \alpha, \beta = 1 \text{ or } 2,$$

where $dx^1 = dr$ and $dx^2 = ds$.

The equivalent expressions for the gradient ∇ and the divergence ∇^2 in the (r, s) coordinate are obtained using tensor calculus [74, 75], where, in tensor forms they are given as follows,

$$\nabla\psi = \nabla^\alpha\psi, \quad (\text{A.12})$$

$$\nabla^2\psi = (\nabla^\alpha\psi)_{;\alpha}, \quad (\text{A.13})$$

where $\psi(r, s)$ is an arbitrary differentiable function. Expanding the right-hand side of equation (A.12), we have

$$\begin{aligned} \nabla\psi &= \begin{pmatrix} 1 & 0 \\ 0 & 1/h^2 \end{pmatrix} \begin{pmatrix} \psi_r \\ \psi_s \end{pmatrix} \\ &= \psi_r \hat{\mathbf{r}} + \frac{1}{h^2} \psi_s \hat{\mathbf{s}}, \end{aligned} \quad (\text{A.14})$$

where $\hat{\mathbf{r}}$ and $\hat{\mathbf{s}}$ are the unit vectors in the r and s directions respectively. Similarly, we expand the right-hand side of equation (A.13) to obtain an equivalent expression for the divergence,

$$\nabla^2\psi = (\nabla^\alpha\psi)_{;\alpha} + (\nabla^\mu\psi) \Gamma_{\mu\alpha}^\alpha, \quad (\text{A.15})$$

where $\Gamma_{\beta\gamma}^\alpha$ are the *Christoffel symbols*. Variational methods lead us to the following nonzero values of the Christoffel symbols,

$$\Gamma_{22}^1 = h h_r, \quad \Gamma_{12}^2 = \Gamma_{21}^2 = \frac{h_r}{h}, \quad \Gamma_{22}^2 = \frac{h_s}{h},$$

which are substituted into (A.15) to give,

$$\begin{aligned}\nabla^2\psi &= \psi_{rr} + \left(\frac{1}{h^2}\psi_s\right)_s + \psi_r\left(\frac{h_r}{h}\right) + \frac{1}{h^2}\psi_s\left(\frac{h_s}{h}\right) \\ &= \frac{1}{h}\left[(h\psi_r)_r + \left(\frac{1}{h}\psi_s\right)_s\right].\end{aligned}\quad (\text{A.16})$$

Equations (A.14) and (A.16) provide the appropriate expressions for ∇ and ∇^2 in the curvilinear coordinate (r, s) .

Appendix B

The Nickel-Copper alloy data

	Nickel	Copper
Classical parameters		
$T_M(K)$	1728	1358
$L(J/cm^3)$	2350	1725
$^1v_m(cm^3/mole)$	7.0	7.8
$^2\sigma(J/cm^2)$	3.7×10^{-5}	2.8×10^{-5}
$^3D(cm^2/s)$	10^{-5}	10^{-5}
Phase-field materials parameters		
$\epsilon(J/cm)^{1/2}$	3.3×10^{-6}	3.3×10^{-6}
$W(J/cm^3)$	8.9×10^3	5.1×10^3
$\beta(T)$	$1.6 \frac{(T-T_M^A)}{T_M^A}$	$2.0 \frac{(T-T_M^B)}{T_M^B}$
$M_1(cm^3/Js)$	4.9×10^8	4.9×10^8
$^4M_2(cm^5/Js)$	5.7×10^{-9}	5.7×10^{-9}

A table of the classical and phase-field parameters for the Nickel-Copper alloy, taken from WBM1 [1]. The material parameters used in this thesis are the same as those in both the WBM1 and the WBM2 model.

¹We have used an average value of 7.4 for the alloy because our model does not deal with volume changes.

²Estimated from $\sigma = 0.7L(v_m/N_o)^{\frac{1}{3}}$, see Coriell and Turnbull [76]; N_o is Avogadro's number.

³Typical liquid diffusion coefficient.

⁴At $T^* = (T_M^A + T_M^B)/2 = 1543K$.

Appendix C

Finite difference discretization

The governing equations (for $0 \leq D_S/D_L \leq 1$) (7.10) and (7.11) may be formulated as three second order nonlinear differential equations for variables ϕ , c and γ say, where γ is defined as,

$$\gamma = -\Delta^2 \frac{d^2 c}{d\tilde{z}^2} + \tilde{f}_c^{(-2)} + \tilde{f}_c^{(0)}. \quad (\text{C.1})$$

Therefore, the governing equations are reduced to,

$$\frac{d^2 \phi}{d\tilde{z}^2} + \frac{\tilde{V}_\epsilon}{\tilde{m}} \frac{d\phi}{d\tilde{z}} - [\tilde{f}_\phi^{(-2)} + \tilde{f}_\phi^{(0)}] = 0, \quad (\text{C.2})$$

$$c(1-c)D(\phi) \frac{\gamma}{d\tilde{z}} + (D(\phi) + 1) \frac{dc}{d\tilde{z}} + \tilde{V}_\epsilon(c - c_\infty) = 0, \quad (\text{C.3})$$

$$\gamma + \Delta \frac{d^2 c}{d\tilde{z}^2} - [\tilde{f}_c^{(-2)} + \tilde{f}_c^{(0)}] = 0, \quad (\text{C.4})$$

where the corresponding boundary conditions are,

$$\frac{d\phi}{d\tilde{z}} = \frac{dc}{d\tilde{z}} = \frac{d\gamma}{d\tilde{z}} = 0. \quad (\text{C.5})$$

The domain length L_N is divided into $N - 1$ equally spaced intervals, where N is the number of points at which the functions ϕ , c and γ are evaluated. Each of these points is defined as,

$$x_i = il, \quad i = 1, \dots, N,$$

where $l = L_N/(N - 1)$, the interval length. Correspondingly, the nodal values of ϕ , c and γ are defined as $\phi_i = \phi(x_i)$, $c_i = c(x_i)$ and $\gamma_i = \gamma(x_i)$. These values form a vector \mathbf{U} whose entries are ordered as follows (with subscript i denoting the i th entry),

$$\mathbf{U}_i = \phi_i, \quad (\text{C.6})$$

$$\mathbf{U}_{i+1} = c_i, \quad (\text{C.7})$$

$$\mathbf{U}_{i+2} = \gamma_i. \quad (\text{C.8})$$

The last entry of \mathbf{U} , namely \mathbf{U}_{3N+1} , is defined to be the temperature T .

The derivatives are discretised using the *Central Difference Approximation* [77] to give,

$$\frac{d\phi}{d\tilde{z}} = \phi_z^i = \frac{\phi_{i+1} - \phi_{i-1}}{2l} = \frac{\mathbf{U}_{i+3} - \mathbf{U}_{i-3}}{2l}, \quad (\text{C.9})$$

$$\frac{d^2\phi}{d\tilde{z}^2} = \phi_{zz}^i = \frac{\phi_{i+1} - 2\phi_i + \phi_{i-1}}{l^2} = \frac{\mathbf{U}_{i+3} - 2\mathbf{U}_i + \mathbf{U}_{i-3}}{l^2}, \quad (\text{C.10})$$

$$\frac{dc}{d\tilde{z}} = c_z^i = \frac{c_{i+1} - c_{i-1}}{2l} = \frac{\mathbf{U}_{j+3} - \mathbf{U}_{j-3}}{2l}, \quad (\text{C.11})$$

$$\frac{d^2c}{d\tilde{z}^2} = c_{zz}^i = \frac{c_{i+1} - 2c_i + c_{i-1}}{l^2} = \frac{\mathbf{U}_{j+3} - 2\mathbf{U}_j + \mathbf{U}_{j-1}}{l^2}, \quad (\text{C.12})$$

$$\frac{d\gamma}{d\tilde{z}} = \gamma_z^i = \frac{\gamma_{i+1} - \gamma_{i-1}}{2l} = \frac{\mathbf{U}_{k+3} - \mathbf{U}_{k-3}}{2l}, \quad (\text{C.13})$$

$$j = i + 2, \quad k = i + 3, \quad i = 1, \dots, N,$$

These derivatives are inserted into equations (C.2), (C.3) and (C.4) to form $3N$ nonlinear equations in ϕ , c , γ and their derivatives. These nonlinear equations another vector \mathbf{V} , where,

$$\mathbf{V}_i = \phi_{zz}^i + \frac{\tilde{V}_\epsilon}{\tilde{m}} \phi_z^i - [\tilde{f}_\phi^{(-2)}(\phi_i, c_i) + \tilde{f}_\phi^{(0)}(\phi_i, c_i)], \quad (\text{C.14})$$

$$\mathbf{V}_{i+1} = c_i(1 - c_i)D(\phi_i)\gamma_z^i + (D(\phi_i) + 1)c_z^i + \tilde{V}_\epsilon(c_i - c_\infty), \quad (\text{C.15})$$

$$\mathbf{V}_{i+2} = \gamma_i + \Delta c_{zz}^i - (\tilde{f}_c^{(-2)}(\phi_i, c_i) + \tilde{f}_c^{(0)}(\phi_i, c_i)), \quad (\text{C.16})$$

$$(\text{C.17})$$

where \mathbf{V}_i is the i -th component of the vector \mathbf{V} . The extra equation for the temperature, i.e., (7.12) is included in the formulation as the last entry of \mathbf{V} , and it is discretised using the Simpson's Rule to give,

$$\mathbf{V}_{3N+1} = \frac{l}{3} \sum_{i=1}^{i=N} (\phi_{i+1} + 4\phi_i + \phi_{i-1}).$$

Note that the boundary conditions will be imposed on the first three entries of \mathbf{V} , and on \mathbf{V}_{3N-2} , \mathbf{V}_{3N-1} and \mathbf{V}_{3N} . The entries of \mathbf{V} provide $3N + 1$ nonlinear equations for the $3N + 1$ variables, namely ϕ_i , c_i , γ_i , $i = 1, \dots, N$, and T .

Boundary conditions

The far-field conditions are applied at the two ends of the domain, namely we imposed conditions at $\tilde{z} = -\infty$ at $-L_N/2$ and conditions at $\tilde{z} = +\infty$ at $L_N/2$.

(1) At $-L_N/2$:

$$\phi_z^1 = c_z^1 = \gamma_z^1 = 0,$$

giving,

$$\phi_{\bar{z}\bar{z}}^1 = \frac{2(\phi_2 - \phi_1)}{l^2}, \quad (\text{C.18})$$

$$c_{\bar{z}\bar{z}}^1 = \frac{2(c_2 - c_1)}{l^2}, \quad (\text{C.19})$$

$$\gamma_{\bar{z}\bar{z}}^1 = \frac{2(\gamma_2 - \gamma_1)}{l^2}. \quad (\text{C.20})$$

The conditions above are substituted into the first three entries of \mathbf{V} respectively to give the first three nonlinear equations of the system.

(2) At $L_N/2$:

We have similar conditions as above, i.e.,

$$\phi_{\bar{z}}^N = c_{\bar{z}}^N = \gamma_{\bar{z}}^N = 0.$$

The second derivatives are therefore given by,

$$\phi_{\bar{z}\bar{z}}^N = \frac{2(\phi_{(N-1)} - \phi_N)}{l^2}, \quad (\text{C.21})$$

$$c_{\bar{z}\bar{z}}^N = \frac{2(c_{(N-1)} - c_N)}{l^2}, \quad (\text{C.22})$$

$$\gamma_{\bar{z}\bar{z}}^N = \frac{2(\gamma_{(N-1)} - \gamma_N)}{l^2}. \quad (\text{C.23})$$

Similarly, these conditions are substituted into the last three entries of \mathbf{V} .

Appendix D

Fortran program PDE1.F

```
#define NOPTS 201
#define NODE 3
      program main
c
c program to compute 1-d p.f. solutions for solute trapping
c modified from bif2.f for solving algebraic nonlinear equations
c
      parameter ( npts = NOPTS, neq = NODE*npts +1 ,
.                iwork = 3*neq, lwa = (3*neq**2 + 13*neq)/2 )
      common /b/ delx, fswitch, mswitch, mprint
      common /c/ eps,dsiga,dsigb,xla,xlb,v,xm,vmax
      common /d/ temp,xke,cinf, tma, tmb
      common /e/ del, dd
      dimension y(neq),f(neq),fp(neq,neq),
.              iv1(neq),fv1(neq),alfr(neq),alfi(neq),
.              z(neq,neq),v1(neq),v2(neq)
      complex eig(neq),cmax
      dimension work(iwork),wa(lwa)
      external fcn
c
c      read in data
      open(4,file='pde1.dat',status='unknown')
      read(4,*)
      read(4,*) ncont
      read(4,*)
      read(4,*) eps, dsiga, dsigb, xla, xlb,v
      read(4,*)
      read(4,*) xke, tt, xm, tma, tmb
      read(4,*)
      read(4,*) mswitch,fswitch, xlen, del, vmax
      read(4,*)
      read(4,*) dd
c
c      compute delx, the length of the interval
      delx = xlen/float(npts -1)
```

```

c
gas = 8.314
vm = 7.4
rtvm = gas*tt/vm
dfa = xla*(tt - tma)/(tma*rtvm)
dfb = xlb*(tt - tmb)/(tmb*rtvm)
cs = (exp(dfa) - 1.0)/(exp(dfa) - exp(dfb))
cinf = cs
cl = cs*exp(dfb)

c
if(v .eq. 0.0) cinf = cl

c
t0 = (cinf*xlb + (1.0-cinf)*xla)/(cinf*xlb/tmb
.      + (1.0-cinf)*xla/tma)
rt0vm = gas*t0/vm
sigas0 = dsiga/(eps*sqrt(rt0vm))
sigb0 = dsigb/(eps*sqrt(rt0vm))
sigsta0 = sqrt(cinf*sigb0**2 + (1.0-cinf)*sigas0**2)
write(*,*) 'cinf, sigas0, sigb0, sigsta0 = ',
.      cinf, sigas0, sigb0, sigsta0

c
c set the initial guesses \phi, c and \gamma as y(1), y(2) and y(3)
c respectively.
temp = t0
write(*,*) 'exact solution'
xold = -xlen/2.0

c
if (v .gt. vmax) then

c
c initial guess for velocity greater than vmax
do i = 1, npts

    x = xold + (i-1)*delx
    i1 = NODE*(i - 1) + 1
    i2 = i1 + 1
    i3 = i2 + 1
    y(i1) = 0.5*( 1.0 - tanh( 3.0*sigsta0*(x) ) )
    c1 = -cinf*(1.0-cinf)*((dd - 1)*y(i1)**2*(3 -2.0*y(i1)) + 1.0)
.      *(1.0-(tanh(3.0*sigsta0*(x))
.      **2))*fcfun(y(i1),cinf)
    y(i2) = cinf + c1/v
    y(i3) = fcfun(y(i1),y(i2))

end do
elseif (v .ge. 0.0 .and. v .le. vmax) then

c
c initial guess for velocity less than or equal to vmax
do i=1, npts

c
    x = xold + (i-1)*delx
    i1 = NODE*(i-1) + 1

```

```

i2 = i1 + 1
i3 = i2 + 1

x11 = 0.5*(NOPTS-1)*delx
y(i1) = 0.5*(1.0-tanh(3.0*sigsta0*(x)))

c
delfa_dl = xla*(temp/tma - 1.0)/rt0vm
delfb_dl = xlb*(temp/tmb - 1.0)/rt0vm
dd1 = delfa_dl - delfb_dl

delf = (siga0**2 - sigb0**2)*y(i1)**2*(1.0-y(i1))**2
delf = 18.0*delf + dd1*y(i1)**2*(3.0 - 2.0*y(i1))
delf = delf + fcfun(0.0,c1)

y(i2) = 1.0/(1.0 + exp(-delf))

y(i3) = fcfun(y(i1),y(i2))

c
end do
end if

c
c set initial temperature to tt
y(neq) = temp

c
c to use previous solutions as initial guess, set ncont > 0
if (ncont .ne. 0) call readin(y)

write(6,*)
write(6,*)
write(6,*)
write(6,1300) eps, siga, sigb, delfa, delfb,
.          ncont,mswitch,fswitch
1300 format(5x,' eps = ',1e12.4,5x,' siga = ',1e12.4/,
*          5x,' sigb = ',1e12.4,5x,' delfa = ',1e12.4/,
*          5x,' delfb = ',1e12.4/,
*          5x,' ncont = ', i12,5x,'mswitch = ', i12/,
*          5x,'fswitch = ',1e12.4/)

c
write(6,*) ' starting guess....'
call output(y)

c
c set parameters for snsqr
iopt = 2
tol = 1.0e-9
nprint = 1
mprint = 1

c
write(6,*) ' '
write(6,*) ' calling snsqr.....'
write(6,*) ' '

c

```

```

c      call snsqe using implicit jacobian
c
c      call snsqe(fcn,hjaco,iopt,neq,y,f,tol,nprint,info,
.          wa,lwa)
c
c      write(6,*) ' '
c      write(6,*) ' (is info = 1?) info = ',info
c      write(6,*) ' '
c
c      call fcn(neq,y,f,info)
c
c      call output(y)
c
c      ynorm = 0.0e0
c      do 300 k=1,neq
300  ynorm = ynorm + y(k)**2
c      ynorm = sqrt(ynorm)
c      write(6,*) ' '
c      write(6,*) '=====~=====',
c      write(6,*) ' a2 , y(1), ynorm: '
c      write(6,*) a2, y(1), ynorm
c
c      call resave(y)
c
c      call gnu(y)
c
c      end
c=====
c      subroutine output(y)
c=====
c      This subroutine writes out the solutions at any stage it is called.
c      y(1) = \phi, y(2) = c, y(3) = \gamma, y(neq) = temp
c
c      parameter ( npts = NOPTS, neq = NODE*npts + 1)
c
c      dimension y(*)
c
c      compute max and min of c
c
c      cmin = 1.0
c      cmax = 0.0
c
c      do k=1, npts
c
c      c = y(NODE*(k-1) + NODE-1)
c      if (c.gt.cmax) cmax = c
c      if (c.lt.cmin) cmin = c
c
c      end do
c
c      write(6,*)

```

```

do 10 k= 1, npts
write(6, '( 'k, phi, c:  ',i3,2x,1pe13.5,2x,1pe13.5,2x,1pe13.5)')
.      k ,y(NODE*(k - 1)+ 1), y(NODE*(k-1) + 2),
.      y(NODE*(k-1) + 3)
10 continue
c
write(6,*)
write(6,*) 'temperature =', y(neq)
write(6,*) 'cmin,cmax,k = '
write(6,*) cmin,cmax,cmin/cmax
c
return
end
c=====
      subroutine readin(y)
c=====
c
c This subroutine reads in the solution vector y(*) from the file fort.8.
c It is normally used to read in the solutions from the previous run and
c use them as the current initial guesses.
c
      parameter ( npts = NOPTS, neq = NODE*npts+1)
      common /b/ delx, fswitch, mswitch, mprint
      common /c/ eps,dsiga,dsigb,xla,xlb,v,xm,vmax

      dimension y(*)
c
      do j=1,neq
        read(8,*) jdum,y(j)
      end do
c
      return
      end
c=====
      subroutine resave(y)
c=====
c This subroutine store the vector y(*) in the file fort.9. It is
c normally use to store the current solutions for use as initial guesses
c in the following run.
c
      parameter ( npts = NOPTS, neq = NODE*npts+1)
      common /b/ delx, fswitch, mswitch, mprint
      common /c/ eps,dsiga,dsigb,xla,xlb,v,xm,vmax
      dimension y(*)

      do 10 j=1,neq
10 write(9,*) j,y(j)
c
      return
      end

```



```

c=====
      subroutine gnu(y)
c=====
c This subroutine writes out the solutions in the file pde1.out for plotting.
c
      parameter ( npts = NOPTS, neq = NODE*npts+1)
      common /b/ delx, fswitch, mswitch, mprint
      common /c/ eps, dsiga, dsigb, xla, xlb,v,xm,vmax
      dimension y(*)

c
      open(10, file = 'pde1.out', status = 'unknown')
c
      write(10,100) eps, siga, sigb, xla, xlb, vd, xm, tma,tmb
      .      , cinf, delta
100  format('#',1x,e13.5,1x,e13.5,1x,e13.5)
c
      write(10,(''# temp = ',e13.5)) y(neq)
c
      xlen = delx*float(npts - 1)
      do 10 k=1,npts
      c1 = v*(y((k-1)*NODE + 2) - cinf)
      write(10, '(1x,1pe13.5,2x,1pe13.5,2x,1pe13.5,2x,1pe13.5,
      .      2x,1pe13.5,2x,1pe13.5)')
      .      ((k-1)*delx - xlen/2.0), y((k-1)*NODE + 1), y((k-1)*NODE + 2),
      .      y((k-1)*NODE + 3), c1
10  continue
c
      close(10)
c
      return
c
      end

c=====
      subroutine fcn(neq,y,yp,info)

c Subroutine required by snsqe.
c It defines the equations to be solved.
c
      common /b/ delx, fswitch, mswitch, mprint
      common /c/ eps, dsiga, dsigb, xla, xlb, v, xm,vmax
      common /d/ temp, xke, cinf, tma, tmb
      common /e/ del,dd
      dimension y(neq),yp(neq), a(4), t(24), s(3)
      complex r(3)

c
c neqpts is the no of points where equation is solved
c neq is neqpts + 1 - the extra for int constraint
c
      neqpts = neq - 1
c

```

```

c      set temperature - which is the extra degree of freedom
c
c      temp = y(neq)
c
c      if(iflag.eq.0) then
c          write(*,*) 'current guess:'
c          call output(y)
c      end if
c
c set b.c.s at x = -xlen/2 (neumann)
c
c      ipt = 1
c      i1 = NODE*(ipt - 1) + 1
c      i1p1 = i1 + NODE
c      i1m1 = i1p1
c
c compute phi at neighbouring points
c
c      phip1 = y(i1p1)
c      phi = y(i1)
c      phim1 = y(i1m1)
c
c      deriv11 = (phip1 - phim1)/(2.0*delx)
c      deriv12 = 2.0*( phip1 - phi )/(delx**2)
c
c compute (dd-1)phi^2(3-2phi)
c
c      phidum   = (dd-1.0)*phi**2*(3.0 - 2.0*phi)
c
c      i2 = i1 + 1
c      i2p1 = i2 + NODE
c      i2m1 = i2p1
c
c compute c at neighbouring points
c
c      cp1 = y(i2p1)
c      c   = y(i2)
c      cm1 = y(i2m1)
c
c      deriv21 = (cp1 - cm1)/(2.0*delx)
c      deriv22 = 2.0*(cp1 - c)/(delx**2)
c
c      i3 = i2 + 1
c      i3p1 = i3 + NODE
c      i3m1 = i3p1
c
c compute mu at neighbouring points
c
c      xmup1 = y(i3p1)
c      xmu   = y(i3)
c      xmum1 = y(i3m1)

```

```

c
c compute mu'
c
      deriv31 = (xmup1 - xmum1)/(2.0*delx)
c
      yp(i1) = deriv12 + v*deriv11/xm + func(y(i1),y(i2),1)

      yp(i2) = c*(1.0-c)*(phidum + 1.0)*deriv31
               + func(y(i1),y(i2),2)

      yp(i3) = y(i3) + del**2*deriv22 - fcfun(y(i1),y(i2))
c
c set b.c.s at x = xlen/2    (neumann)
c
      ipt = neqpts/NODE
      i1 = NODE*(ipt - 1) + 1
      i1m1 = i1 - NODE
      i1p1 = i1m1
c
c compute phi at neighbouring points
c
      phip1 = y(i1p1)
      phi   = y(i1)
      phim1 = y(i1m1)
c
      deriv11 = (y(i1p1) - y(i1m1))/(2.0*delx)
      deriv12 = 2.0*( y(i1m1) - y(i1) )/(delx**2)

      i2 = i1 + 1
      i2m1 = i2 - NODE
      i2p1 = i2m1
c
c comput c at neighbouring points
c
      cp1 = y(i2p1)
      c   = y(i2)
      cm1 = y(i2m1)
      deriv21 = (cp1 - cm1)/(2.0*delx)
      deriv22 = 2.0*(cp1 - c)/(delx**2)
c
      i3 = i2 + 1
      i3m1 = i3 - NODE
      i3p1 = i3m1
c
c compute xmu at neighbouring points
c
      xmup1 = y(i3p1)
      xmu   = y(i3)
      xmum1 = y(i3m1)
c
      deriv31 = (xmup1 - xmum1)/(2.0*delx)

```

```

c
      yp(i1) = deriv12 + v*deriv11/xm + func(y(i1),y(i2),1)

      yp(i2) = c*(1.0-c)*(phidum + 1)*deriv31
      + func(y(i1),y(i2),2)

      yp(i3) = y(i3) + del**2*deriv22 - fcfun(y(i1),y(i2))
c
c Special case, v=0.0, c= c_L at +\infty
c
      if(v .eq. 0.0) then
        xmup1 = xmum1
        yp(i2) = c - cinf
      endif
c
c set interior points
c
      do ipt = 2, neqpts/NODE - 1
c
c set pointer to neighbouring points and compute second
c derivs
c
        i1 = NODE*(ipt - 1) + 1
        i1m1 = i1 - NODE
        i1p1 = i1 + NODE
        deriv12 = ( y(i1p1) - 2.0*y(i1) + y(i1m1) )/(delx**2)
        deriv11 = (y(i1p1) - y(i1m1))/(2.0*delx)
c
c compute phi at neighbouring points
c
        phip1 = y(i1p1)
        phi    = y(i1)
        phim1 = y(i1m1)
c
c compute (dd-1)phi^2(3-2phi)
c
        phidum  = (dd-1.0)*phi**2*(3.0 - 2.0*phi)

        i2 = i1 + 1
        i2m1 = i2 - NODE
        i2p1 = i2 + NODE
c
c compute c at neighbouring points
c
        cp1 = y(i2p1)
        c    = y(i2)
        cm1 = y(i2m1)
        deriv21 = (cp1 - cm1)/(2.0*delx)
        deriv22 = (cp1 -2.0*c + cm1)/(delx**2)
c
        i3 = i2 + 1

```

```

        i3p1 = i3 + NODE
        i3m1 = i3 - NODE
c
c compute mu at neighbouring points
c
        xmup1 = y(i3p1)
        xmu    = y(i3)
        xmum1 = y(i3m1)
c
c compute mu'
c
        deriv31 = (xmup1 - xmum1)/(2.0*delx)
c
c compute equations
c
        yp(i1) = deriv12 + func(y(i1),y(i2),1)
        yp(i1) = yp(i1) + v*deriv11/xm

        yp(i2) = c*(1.0-c)*(phidum + 1)*deriv31
                (phidum + 1)*deriv21 + func(y(i1),y(i2),2)

        yp(i3) = y(i3) + del**2*deriv22 - fcfun(y(i1),y(i2))
c
        end do
c
c last equation is that \int (phi - 1/2) = 0
c use Simpson's Rule to evaluate this
c
        xint = 0.0
        do ipt = 2, neqpts/NODE - 1,2

            i1 = NODE*(ipt -1) + 1
            i1m1 = i1 - NODE
            i1p1 = i1 + NODE
c
            xint = xint + y(i1m1) + 4.0*y(i1) + y(i1p1)
c
        end do
c
        xint = delx*xint/3.0
        xint = xint - 0.5*(NOPTS - 1)*delx
c
        yp(neq) = xint
c
c compute residual
c
        resid = 0.0e0
        do 100 j=1,neq
100      resid = resid + yp(j)**2

        resid = sqrt(resid)

```

```

        if (mprint.eq.1) write(6,*) ' resid = ',resid
c
        return
        end
c
c=====
        real function func(xphi,c,ieqn)
c=====
c
        common /c/ eps,dsiga,dsigb,xla,xlb,v,xm,vmax
        common /d/ temp, xke, cinf, tma, tmb
c
        fm2a(x) = -72.0*sigadl**2*x*(x-1.0)*(x-0.5)
        fm2b(x) = -72.0*sigbdl**2*x*(x-1.0)*(x-0.5)
c
        f0a(x) = -6.0*delfa*x*(1.0-x)
        f0b(x) = -6.0*delfb*x*(1.0-x)
c
        rtvm = 8.314*temp/7.4
        delfa = xla*(temp/tma - 1.0)/rtvm
        delfb = xlb*(temp/tmb - 1.0)/rtvm
        sigadl = dsiga/(eps*sqrt(rtvm))
        sigbdl = dsigb/(eps*sqrt(rtvm))
c
c gives nonlinearity of the equation
c
        if(ieqn.eq.1) then
c
c phi equation
c
                fm2 = (1.0 - c)*fm2a(xphi) + c*fm2b(xphi)
                f0 = (1.0 - c)*f0a(xphi) + c*f0b(xphi)
                func = fm2 + f0
c
        else if(ieqn.eq.2) then
c
c c equation
c
                func = v*(c-cinf)
c
        end if
c
        return
        end
c=====
        real function fcfun(xphi,c)
c=====
c
        common /c/ eps, dsiga, dsigb, xla, xlb, v, xm,vmax
        common /d/ temp, xke, cinf, tma, tmb
c

```

```

      fm2a(x) = 18.0*sig_a_dl**2*x**2*(1.0-x)**2
      f0a(x)  = delfa*x**2*(3.0-2.0*x)
c
      fm2b(x) = 18.0*sig_b_dl**2*x**2*(1.0-x)**2
      f0b(x)  = delfb*x**2*(3.0-2.0*x)
c
      rtvm = 8.314*temp/7.4
      delfa = xla*(temp/tma - 1.0)/rtvm
      delfb = xlb*(temp/tmb - 1.0)/rtvm
c
      sig_a_dl = dsig_a/(eps*sqrt(rtvm))
      sig_b_dl = dsig_b/(eps*sqrt(rtvm))
c
      fa = fm2a(xphi) + f0a(xphi)
      fb = fm2b(xphi) + f0b(xphi)
c
      fcfun = log(c/(1.0-c)) + fb - fa
c
      return
c
      end

```

Bibliography

- [1] A. A. Wheeler, W. J. Boettinger, and G. B. McFadden, *Phys. Rev. A* **45**, 7424 (1992).
- [2] A. A. Wheeler, W. J. Boettinger, and G. B. McFadden, *Phys. Rev. E* **47**, 1893 (1993).
- [3] C. W. White, B. R. Appleton and S. R. Wilson, *Supersaturated Alloys, Solute trapping and Zone Refining* in *Laser Annealing of Semiconductors*, Edited by J. M. Poate and J. W. Mayer, ch. 5, pp 111 (1982).
- [4] P.M. Smith, R. Reitano and M.J. Aziz, *Mat. Res. Soc. Symp. Proc.*, vol. 279 (1993).
- [5] M. C. Flemings, *Solidification Processing*, Materials Science and Engineering Series, McGraw-Hill (1974).
- [6] W. J. Boettinger and J. H. Perepezko, in *Rapid Solidified Crystalline Alloys* (edited by S. K. Das, B. H. Kear and C. M. Adam), p. 21 *Proc. of a TMS-AIME Northeast Regional Meeting*, Morristown, New Jersey (1985).
- [7] W. J. Boettinger and S. R. Coriell, in *Rapid Solidification Materials and Technologies* (edited by P. R. Sahm, H. Jones and C. M. Adam), p. 81 *Martinus Nijhoff*, Dordrecht (1986).
- [8] M.J Aziz, J.Y. Tsao, M.O. Thompson, P.S. Peercy and C.W. White, *Phys. Rev. Lett.* **56**, no. 23, 2489-2492 (1986).
- [9] M.J. Aziz, *J. Appl. Phys.* **53**, 1158 (1982).
- [10] W. W. Mullins and R. F. Sekerka, *J. Appl. Phys.* **35**, 444 (1964).
- [11] J. S. Langer, in *Directions in Condensed Matter Physics* (World Scientific, Singapore, 1986), pp. 164-186.
- [12] G. Caginalp, *Arch. Rat. Mech. Anal.* **92**, 205 (1986).

- [13] J. B. Collins and H. Levine, Phys. Rev. B **31**, 6119 (1985).
- [14] J. W. Cahn and J. E. Hilliard, J. Chem. Phys. **28**, 28 (1958).
- [15] S. M. Allen and J. W. Cahn, Acta Metall. **27**, 1085 (1979).
- [16] J.C. Baker and J.W. Cahn: *Solidification*, p. 23, American Soc. for Metals, Metals Park (1970).
- [17] J. C. Baker and J. W. Cahn, Acta Metall. **17**, 575 (1969).
- [18] R. J. Braun and S. H. Davis, Acta Metall., **40**, 2617 (1992).
- [19] M.J. Aziz and T. Kaplan, Acta Metall. **36**, no. 8, 2335-2347 (1988).
- [20] M.J. Aziz and C.W. White, Phys. Rev. Lett. **57**, no. 21, 2675-2678 (1986).
- [21] R. Kobayashi, Physica D **63**, 410 (1993).
- [22] A. A. Wheeler, B. T. Murray, and R. J. Schaefer, Physica D **66**, 243 (1993).
- [23] J. D. Van der Waals, *The Thermodynamic theory of capillarity under the hypothesis of a continuous variation of density (in Dutch)*. Verhandel. Konink. Akad. Weten. Amsterdam (Sect. 1) vol 1, no. 8 (Transl. J. S. Rowlinson, J. Stat. Phys., **20**, 197 (1979)).
- [24] V. L. Ginzburg and L. D. Landau, *On the Theory of Superconductivity*, Soviet Phys. JETP **20**, 1064 (1950).
- [25] B. I. Halperin, P. C. Hohenberg and S. -K. Ma, Phys. Rev. B **10**, 139 (1974).
- [26] A. R. Umantsev and A. L. Roitburd, Fiz. Tverd. Tela (Leningrad) **30**, 1124 (1988) [Sov. Phys. Solid State **30**, 651 (1988); A. Umantsev and G. B. Olson, Phys. Rev. A **46**, R6132 (1992).
- [27] O. Penrose and P. C. Fife, Physica D **43**, 44 (1990).
- [28] S-L Wang, R. F. Sekerka, A. A. Wheeler, B. T. Murray, S. R. Coriell, R. J. Braun, and G. B. McFadden, Physica D **69**, 189 (1993).
- [29] G. Caginalp, Phys. Rev. A **39**, 5887 (1989).
- [30] Youn-Woo Lee, R. N. Smith, M. E. Glicksman and M. B. Koss, Annual Review of Heat Transfer, vol. **7**, 59 (1996).

- [31] M. E. Glicksman and S. P. Marsh, *The Dendrite* in The Handbook of Crystal Growth, D. T. Hurle, Ed., vol. 1, Elsevier Science Publishers, Amsterdam, pp. 1077-1122 (1993).
- [32] G. Caginalp and P. C. Fife, Phys. Rev. B *34*, 4940 (1986).
- [33] J. W. Cahn and R. Kikuchi, Phys. Rev. B *31*, 4300 (1985).
- [34] G. B. McFadden, A. A. Wheeler, R. J. Braun, S. R. Coriell and R. F. Sekerka, Phys. Rev. E *48*, 2016 (1993).
- [35] C. Herring, in *Structure and Properties of Solid Surfaces*, edited by R. Gomer and C. S. Smith (University of Chicago, 1952).
- [36] A. A. Wheeler and G. B. McFadden, *On the Notion of a ξ -vector and a Stress Tensor for a General Class of Anisotropic Diffuse Interface Models*, preprint series (1996).
- [37] J. Smith, J. Comp. Phys. *39*, 112 (1981).
- [38] A. R. Umantsev, V. V. Vinograd and V. T. Borisov, Sov. Phys. Crystallogr. *30*, 262 (1986); *31*, 596 (1986).
- [39] G. P. Ivantsov, *Temperature Field Around Spherical, Cylindrical and Needle-shaped Crystals Which Grow in Supercooled Melt*, Dokl. Akad. Nauk, SSR **58**, pp. 567-569, 1947 (Translation by G. Horvay, General Electric Report 60-RL-2511M (1960)).
- [40] J. S. Langer and H. Muller-Krumbhaar, J. Crystal Growth, vol. **43**, 11 (1977).
- [41] J. S. Langer and H. Muller-Krumbhaar, Acta Metall., vol. **26**, 1681 (1978).
- [42] J. S. Langer and H. Muller-Krumbhaar, Acta Metall., vol. **26**, 1689 (1978).
- [43] J. S. Langer and H. Muller-Krumbhaar, Acta Metall., vol. **26**, 1697 (1978).
- [44] H. Lowen, J. Bocheffer, and L. S. Tuckerman, Phys. Rev. A **45**, 2399 (1992).
- [45] J. A. Warren and W. J. Boettinger, Acta Metall. Mater. vol *43*, no. 2, 689 (1995).
- [46] G. Caginalp and W. Xie, Phys. Rev. E *48*, 1897 (1993).
- [47] A. Karma, Phys. Rev. E *39*, 2245 (1994).
- [48] K. R. Elder, F. Drolet, J. M. Kosterlitz and M. Grant, Phys. Rev. Lett. *72*, 677 (1994).
- [49] A. A. Wheeler, G. B. McFadden and W. J. Boettinger, Proc. R. Soc. Lond. A *452*, 495 (1996).

- [50] R. N. Hall, J. Phys. Chem. **57**, 836 (1953).
- [51] M. Hillert and B. Sundman, Acta Metall. **25**, 11 (1977).
- [52] J.C Brice, *The Growth of Crystals from the Melt*, p. 65, North-Holland, Amsterdam (1965).
- [53] M. J. Aziz, Appl. Phys. Lett., **43**, 552 (1983).
- [54] J.A Kittl, M.J. Aziz, D.P. Brunco and M.O.Thompson, *Appl. Phys. Lett.* **64** (18) (1994).
- [55] S. J. Cook and P. Clancy, J. Chem. Phys., vol. **99**,2175 (1993).
- [56] Q. Yu, M. O. Thomson and P. Clancy, Phys. Rev. B, in press (1996).
- [57] D. Turnbull, *Thermodynamics in Metallurgy*, American Society for Metals, Metals Park, Ohio (1952).
- [58] J. A. Rice, *Mathematical Statistics and Data Analysis*, pp. 46-48, Wadsworth and Brooks/Cole Advanced Books and Software, (1988).
- [59] P. Baeri, G. Fotti, J. M. Poate, S. U. Campisano and A. G. Cullis, Appl. Phys. Lett. **38**, 800 (1981).
- [60] J. M. Poate, in *Laser and Electron-Beam Interactions with Solids*, edited by B. R. Appleton and G. K. Celler, Materials Research Society Simposia Proceedings Vol. 4 (North-Holland, Amsterdam, 1982), p. 121.
- [61] C. W. White, D. M. Zehner, S. U. Campisano and A. G. Cullis, in *Surface Modification and Alloying by Laser, Ion and Electron Beams*, edited by J. M. Poate, G. Foti and D. C. Jacobson (Plenum, New York, 1983), p. 94.
- [62] L.M. Goldman and M.J. Aziz, *J. Mater. Res.* **2** (4) (1987).
- [63] D. P. Woodruff, *The Solid-liquid Interface*, Cambridge University Press (1973).
- [64] J. W. Gibbs, *Collected Works*, Yale University Press, New Haven (1948).
- [65] M. Van Dyke, *Perturbation Methods in Fluid Mechanics*, Ch. 5, pg. 77, Academic Press, New York (1964).
- [66] C. H. P. Lupis, *Classical Thermodynamics of Materials*, p. 61-66, 80-86, North-Holland, Amsterdam (1983).

- [67] M. J. D. Powell, *A Hybrid Method for Nonlinear Algebraic Equation*, ed. by P. Rabinowitz, Gordon and Breach (1970).
- [68] M. J. Aziz and W. J. Boettinger, *Acta Metall. Mater.*, (1993).
- [69] D. Turnbull, *J. Phys. Chem.* **66**, 609 (1962).
- [70] W. J. Boettinger (private communications) (1996).
- [71] M.J. Aziz, *Metal. Mat. Trans. A* vol. 27A, (1996).
- [72] J. W. Cahn, W. B. Hillig and G. W. Sears, *Acta Metall.* vol. **12**, 1421 (1964).
- [73] R. J. Braun, G. B. McFadden and S. R. Coriell, *Phys. Rev. E*, vol. **49**, no. 5, 4336 (1994).
- [74] B. E. Schutz, *A First Course in General Relativity*, Cambridge Univ. Press, (1990).
- [75] P. G. Drazin, Lecture notes on General Relativity course at University of Bristol (1993).
- [76] S. R. Coriell and D. Turnbull, *Acta Metall.* **30**, 2135 (1982).
- [77] G. D. Smith, *Numerical Solution of Partial Differential Equations: Finite Difference Methods*, 3rd. edition, Clarendon Press, Oxford (1985).